# Nonlinear nonequilibrium dynamics in a nematic liquid crystal

vorgelet von
M. Sc.
Tillmann Stieger
geb. in Jena

von der Fakultät II – Mathematik und Naturwissenschaften
der Technischen Universität Berlin
zur Erlangung des akademischen Grades

Doktor der Naturwissenschaften
- Dr.-rer.-nat. -

vorgelegte Dissertation

Promotionsausschuss:

| | |
|---|---|
| Vorsitzender: | Prof. Dr. Martin Lerch |
| Gutachter: | Prof. Dr. Martin Schoen |
| Gutachter: | Dr. Marco G. Mazza |
| Gutachter: | Prof. Dr. Joachim Dzubiella |

Tag der wissenschaftlichen Aussprache:

Berlin 2016

# Zusammenfassung

Mit Hilfe von Molekulardynamiksimulationen im Nichtgleichgewicht untersuchen wir einen nematischen Flüssigkristall, welcher um ein kolloidales Teilchen fließt. Die Diskrepanz zwischen der globalen nematischen Vorzugsrichtung und der lokalen Orientierung der Flüssigkristallmoleküle an der Kolloidoberfläche führt zu Defekttopologien im thermodynamischen Gleichgewicht. Wir untersuchen die Modifikation der topologischen Defekte durch Fluss. Unsere Untersuchungen ergeben, in Übereinstimmung mit experimentellen Befunden [1], dass ein Saturnringdefekt in Flussrichtung verschoben wird. Zusätzlich wird der Saturnring durch den Poiseuillefluss verformt. Die Verformung lässt sich anhand von geometrischen Parametern aus Anpassungen geeigneter Projektionen des Saturnrings quantitativ analysieren. Unsere Simulationen zeigen, dass kleinere Saturnringe stromabwärts verschoben werden und ihre Kreisform nahezu behalten. Größere Saturnringdefekte hingegen weisen eine elastische Verformung auf, welche von der Kreisform abweicht. Weiterhin zeigen wir, dass der Fluss einen Boojumdefekt in einen asymmetrischen größeren Defekt flussabwärts verformt. Januskolloide weisen eine Kombination aus Boojum- und Saturnringdefekt auf. Unsere Untersuchung ergibt, dass der Boojumdefekt flussaufwärts zerstört wird und der Saturnring flussabwärts verschoben wird.

Außerdem untersuchen wir ein vergleichbares System, in welchem der nematische Flüssigkristall um eine zylindrische Säule fließt. Wir beobachten flussinduzierte Kavitation in einer anisotropen Flüssigkeit. Kavitationsdomänen bilden sich auf Grund des Druckverlusts hinter der zylindrischen Säule. Sowohl die Entstehung als auch das Wachstum der Kavität findet unter laminaren Flussbedingungen statt. Wir untersuchen im Detail die physikalischen Ursachen, welche zum Phänomen der Kavitation in einem nematischen Flüssigkristall führen. Weiterhin bestimmen wir den kritischen Wert der Reynoldszahl für den Beginn der Kavität. Dieser kritische Wert skaliert invers mit dem charakteristischen Ordnungsparameter für einen nematischen Flüssigkristall. Markanterweise kann die kritische Reynoldszahl bis zu 50% niedriger sein als der Kavitationsbeginn in einem isotropen Flüssigkristall. Diese Befunde weisen darauf hin, dass die langreichweitige Ordnung potentiell als Kontrollparameter verwendet werden kann um den Beginn von Kavitation in anisotropen Flüssigkeiten zu beeinflussen. Zusätzlich erreichen wir sehr gute Übereinstimmung mit mikrofluidischen Experimenten [2] für geringere Flussgeschwindigkeiten, bevor die Kavitation einsetzt. Unsere Simulationen sind in der Lage die strukturellen Veränderungen innerhalb des Mikrokanals für verschiedene Flussgeschwindigkeiten zu reproduzieren.

# Abstract

Liquid crystals are elongated molecules with a rich and surprising phase behavior. Nonequilibrium conditions open a myriad possibilities of manipulating matter, and reach collective states not accessible under equilibrium conditions. We perform nonequilibrium molecular dynamics simulations of a nematic liquid crystal flowing around a colloidal particle. Because of a mismatch between the nematic far field alignment and the local orientation of the liquid-crystal molecules at the surface of the colloid, defect topologies arise if the host is in thermodynamic equilibrium. We study the flow-induced modifications of these topological defects. We find that Saturn ring defects are convected downstream along the flow direction, which is in agreement with experimental observations [1]. As Poiseuille flow is initiated, the Saturn ring is deformed. The degree of deformation is analyzed quantitatively in terms of characteristic geometric parameters fitted to suitable projections of the Saturn ring. Our results suggest that smaller Saturn rings are shifted downstream while approximately maintaining their circular shape, whereas larger ones exhibit an elastic deformation in addition. Additionally, we show that flow distorts Boojum defects into an asymmetrically larger downstream lobe. For a Janus colloid, exhibiting a Boojum defect and a Saturn ring defect, we find that the Boojum defect facing the upstream direction is destroyed and the Saturn ring is convected downstream.

Furthermore, we study a similar system of a nematic liquid crystal flowing around a cylindrical pillar. We report flow-induced cavitation in an anisotropic fluid. Cavitation domains nucleate due to a sudden drop in pressure upon flow past the cylindrical obstacle. The inception and growth of cavitation domains ensue in the laminar flow regime. We study the physical principles governing the cavitation phenomena in nematic liquid crystals, and identify a critical value of the Reynolds number for cavitation inception that scales inversely with the characteristic order parameter of the nematic liquid crystal. Strikingly, the critical Reynolds number can be as low as about 50% of the cavitation threshold in the isotropic liquid crystal. These findings suggest that long range ordering, and its tunability, can be potentially applied as a novel control parameter to modulate cavitation inception in anisotropic fluids. Additionally, we find very good agreement with earlier microfluidic experiments [2] at smaller flow speeds before cavitation initiates. Our simulations are able to reproduce the structural changes within the microfluidic channel at different flow speeds.

# List of publications

**Contributing publications:**

[A] T. Stieger, M. Schoen, and M. G. Mazza. Effects of flow on topological defects in a nematic liquid crystal near a colloid. *J. Chem. Phys.*, 140:054905, 2014.

[B] T. Stieger, S. Püschel-Schlotthauer, M. Schoen, and M. G. Mazza. Hydrodynamic cavitation in Stokes flow of anisotropic fluids. *Mol. Phys.*, 114:259, 2016.

[C] T. Stieger, H. Agha, M. Schoen, M. G. Mazza, and A. Sengupta. Hydrodynamic cavitation in Stokes flow of anisotropic fluids. *submitted*, 2016.

**Non-contributing publications:**

[D] S. Schlotthauer, R. A. Skutnik, T. Stieger, and M. Schoen. Defect topologies in chiral liquid crystals confined to mesoscopic channels. *J. Chem. Phys.*, 142:194704, 2015.

[E] S. Püschel-Schlotthauer, T. Stieger, M. Melle, M. G. Mazza, and M. Schoen. Coarse-grained treatment of the self-assembly of colloids suspended in a nematic host phase. *Soft Matter*, 12:469, 2016.

[F] A. Córdoba, T. Stieger, M. G. Mazza, M. Schoen, and J. J. de Pablo. Anisotropy and probe-medium interactions in the microrheology of nematic fluids. *J. Rheo.*, 60:75, 2016.

# Contents

# 1 Introduction

## 1.1 History of liquid crystals

Liquid crystals were discovered in a series of experiments between 1850 and 1888. While performing experiments with polarized light on biological specimens, Virchow [3] and Mettenheimer [4] independently noticed unusual effects. Liquids usually do not polarize light, whereas solids do because of their regular crystalline structure. However, the biological specimens were not solid and yet they exhibited unusual polarization effects. Unfortunately, the structure of these biological specimens is complicated and therefore a more detailed study was not possible at that time. Another contributing experiment before the actual discovery of liquid crystals was performed by Lehmann [5]. He was investigating how certain substances crystallize with the aid of a heating stage for his microscope. He later added polarizers to his microscopes and was one of the first to use a polarized light microscope. Lehmann observed an amorphous before the clear liquid crystallized but did not realize at the time that he had found a new phase. He related the effects to anomalies during the liquid-solid phase transition. Around the same time Planer [6], Löbisch [7] and Raymann [8] noticed remarkable colors when cooling a compound synthesized from cholesterol. However, they were unable to offer any explanation. In 1850 Heintz observed that the organic substance stearin first melts into a cloudy liquid before turning clear at an even higher temperature. He stated that there was a second melting point. About forty years later Reinitzer [9] performed a very similar experiment with an organic substance related to cholesterol and observed a second melting point, too. He also reported color phenomena like earlier scientists working with similar substances. Today Reinitzer is given credit for the discovery of liquid crystals. He was the first to connect earlier studies and set the future path for the field. The term *liquid crystal* was first introduced by Lehmann [10] and unlike many other designations survived until today.

After Reinitzer's discovery Lehmann performed many other experiments that contributed to the further exploration of liquid crystals. Among those were experiments on the first synthesized nematic liquid crystal discovered by Gattermann and Ritschke [11]. Their compound was also the first liquid crystal not based on a natural substance. Lehmann noticed a difference in some liquid-crystal compounds, known today as nematic and smectic. Furthermore, he observed that liquid crystals tend to orient in a certain direction on solid substrates. The chemist Vorländer [12] was the first to observe a liquid crystal with more than one liquid-crystal phase. He also suggested that molecules with a linear shape are more likely to form liquid-crystal phases.

Influenced by Vorländer's suggestions the physicist Bose attempted to construct a complete molecular theory for liquid crystals [13–15]. Later Born [16] suggested that the basic interaction between molecules leading to liquid-crystal phases is caused by a separa-

tion of charge in the linear molecules. In 1922 Friedel [17] proposed a classification scheme of nematic, smectic and cholesteric using the concept of molecular ordering. He pointed out that the lines seen while studying liquid crystals with a microscope correspond to defect structures, that is drastic changes in molecular orientation on a microscopic length scale. It was also very clear to him that liquid crystals could be oriented by an electric field. Later Oseen [18] worked theoretically on the elastic properties of liquid crystals, work that was concluded much later by Frank [19] at the continuum level. During the period around World War II research on liquid crystals slowed down. However, it should be pointed out that a quantification in the form of an order parameter was developed by Tsvetkov in 1942 [20]. This order parameter has been utilized in countless subsequent studies including both experiments and theory.

Research on liquid crystals resumed shortly before 1960. Brown and Shaw [21] published an article reviewing the liquid-crystal state. Their review article can be viewed as a catalyst for the renewed interest in liquid crystals. Maier and Saupe [22–24] formulated a microscopic theory that was not based on the separation of charge in the linear molecules. This was the first theory predicting liquid-crystal behavior starting from a realistic description of the individual molecules. Another milestone in liquid-crystal research was the development of the liquid crystal display (LCD), first used in wristwatches and pocket calculators and, later for computer displays and television. Consequently, during the 1970's and 1980's research on liquid crystals literally exploded. This technological breakthrough and the rapid scientific progress has made the field of liquid crystal research as broad and fascinating as it is today. The field of colloidal dispersions in nematic liquid crystals [25] is an adequate representation of the widespread research nowadays. For example, investigations on colloidal self-assembly [26] show the joined endeavor of experimentalists and theoreticians in liquid crystal research. Today, the complexity of phenomena involving liquid crystals must be tackled by a combined effort involving both chemistry and physics [27, 28].

## 1.2 Physics and chemistry of liquid crystals

From the general discussion above it is clear that the term *liquid crystal* describes a state between the crystalline solid and the amorphous liquid. Generally speaking a compound in that state features strong anisotropic properties as well as a certain degree of fluidity. There exist quite a number of organic compounds capable of forming liquid-crystal phases. All of these compounds share one common property, namely that they are anisotropic in shape. Hence, their shape is such that one molecular axis is different from the remaining two. Therefore, interaction between these anisotropic molecules leads to orientational or even positional order within a fluid phase. Figure 1 shows one representative organic compound where one molecular axis is longer than the other two. Thus, the molecule is

anisotropic in shape resembling a rod. These compounds are classified as calamitic liquid crystals. It is important that the central part of the molecule is rather rigid in shape to produce the necessary interactions which favor alignment. The rigid part of the molecule is often called “mesogen”.

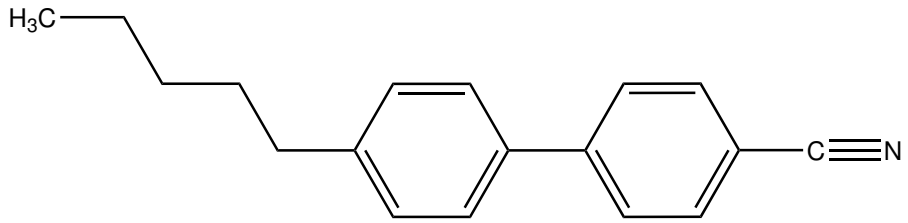


Figure 1: Chemical structure of 4-Cyano-4’-pentylbiphenyl, a widely used nematic liquid crystal which goes by the common name 5CB.

Molecules with one molecular axis shorter than the remaining two are of a disk-like shape. Therefore, these compounds are called discotic liquid crystals. As one can imagine their phase behavior is quite different from calamitic liquid crystals. Both types are called thermotropic liquid crystals because the different liquid-crystal phase transitions are driven by temperature changes. Two other types of liquid crystals are known. For lyotropic liquid crystals the formation of the phase depends strongly on the solvent concentration. Also polymers are capable of forming liquid-crystal phases if they consist of a rigid backbone. However, in this work we are going to focus only on calamitic liquid crystals.

Liquid crystals are most know for their remarkable optical features as already emphasized above. For example, their various ordered phases can give rise to Bragg reflections at specific optical wavelengths. Additionally, the wavelength of the reflected light exhibits a temperature dependence. Hence, the color of such a liquid-crystal phase changes over a small temperature range. Some liquid-crystal phases are birefringent and therefore exhibit the phenomenon of double refraction. Liquid crystals also respond heavily to external fields such as magnetic and electric fields. All of these properties are strongly linked to the anisotropy of the molecules, namely the orientational or even positional structural order of the corresponding liquid-crystal phase [28–30].

## 1.3 Phases of liquid crystals

Substances can exist in more than one state of aggregation. The most common states are solid, liquid and gas. In a crystalline solid molecules only occupy certain positions. Additionally, molecules are also constrained in the way they are oriented with respect to each other. Hence, a crystal exhibits both long-range positional order and orientational order. However, when a phase transition from solid to liquid occurs both types of order are lost. Thus, in a common liquid phase molecules are randomly oriented and positioned.

For liquid crystals this situation is entirely different. During the phase transition from a solid into a liquid-crystal phase molecules maintain a certain degree of orientational and sometimes even positional order. Thus, there exist a variety of different liquid-crystal phases. Here we are going to focus on the nematic phase.

The nematic phase is characterized by long-range orientational order but only short-range positional order. In fact a nematic phase still exhibits fluid motion. Figure 2 shows a schematic representation of the nematic phase as an intermediate state between liquid and solid. Molecules tend to be parallel to some common axis, described by a unit vector $\hat{\boldsymbol{n}}_0$, the so-called director. The nematic phase is rotationally invariant around $\hat{\boldsymbol{n}}_0$. In the absence of any surfaces or other external fields the direction of $\hat{\boldsymbol{n}}_0$ is infinitely degenerate. In other words, an infinite number of so-called "easy-axes" exist for $\hat{\boldsymbol{n}}_0$ in the terminology of Jerome [31]. Consequently, by using suitable external fields $\hat{\boldsymbol{n}}_0$ can be made monostable, that is a preferred single orientation of $\hat{\boldsymbol{n}}_0$ can be imposed. Furthermore, due to the head-tail symmetry of liquid crystals $\hat{\boldsymbol{n}}_0$ and $-\hat{\boldsymbol{n}}_0$ are indistinguishable. Only compounds consisting of molecules which do not distinguish between up and down, meaning mirror images of molecules are identical, are capable of forming a nematic phase. However, for compounds with a left- and right-handed species (chirality) a mixture of equal parts is capable of forming a nematic phase as well. It is immediately clear that orientational order is a key quantity to characterize nematic liquid crystals [27, 30].

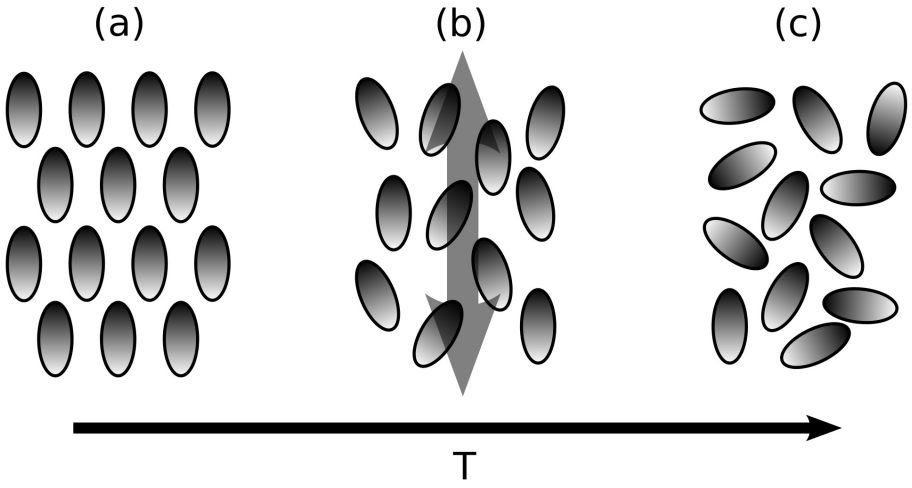


Figure 2: Schematic representation of the phase transitions for increasing temperature from (a) solid to (b) nematic and (c) liquid. The gray shaded double-headed arrow represents the director $\hat{\boldsymbol{n}}_0$.

## 1.4 Order parameters for nematic liquid crystals

To describe quantitatively the amount of orientational order in a nematic liquid crystal a variety of options seems plausible. However, it is immediately clear that since molecules are not fixed one needs to consider some sort of average to describe the order. The simplest approach is to calculate the angle between each molecule and one common axis (for instance the $z$-axis) from a snapshot of the system. Values between 90° and 0° are obtained, where the latter represents perfect alignment with the $z$-axis. The average over all molecules yields then a quantitative measure for the orientational order of the liquid-crystal phase. However, in a three dimensional system only in the single case of perfect alignment 0° is obtained. Whereas, innumerable orientations of a molecule yield values close to 90°. For a perfect aligned nematic phase, with $\hat{\boldsymbol{n}}_0$ pointing along the $z$-axis, the average angle is 0° as expected. However, it turns out that for a phase with absolutely no orientational order the average angle is 57° and not 45° as one would suspect [27]. Therefore, the procedure is misleading because the angle 57° suggests a net orientation for a phase with no orientational order.

To obtain correct values a different description is widely used nowadays. The magnitude of the orientational order is described by an average over the function $(3\cos^2\theta - 1)/2$ [20]. It is straightforward to see that this function is equal to 1 for perfect alignment and equal to 0 when no orientational order is present. The average of the function over all molecules is called the nematic order parameter [22–24, 27].

We define the nematic order parameter

$$S = \frac{1}{N}\left\langle \sum_{i=1}^{N} \frac{3}{2}\cos^2\theta_i - \frac{1}{2} \right\rangle, \tag{1.1}$$

where $N$ is the number of molecules, $\theta_i$ is the angle between the orientation of a molecule $\hat{\boldsymbol{u}}_i$ and the nematic director $\hat{\boldsymbol{n}}_0$ and $\langle \ldots \rangle$ indicates the ensemble or time average. However, $\hat{\boldsymbol{n}}_0$ is not known a priori. Thus, the nematic order parameter has to be calculated in a different fashion [32]. For a sufficiently large number of molecules one can actually compute

$$\begin{aligned} S &= \left\langle \sum_{i=1}^{N} \left[ \frac{3}{2}(\hat{\boldsymbol{n}}_0 \cdot \hat{\boldsymbol{u}}_i)^2 - \frac{1}{2} \right] \right\rangle \\ &= \sum_{i=1}^{N} \left\langle \left[ \hat{\boldsymbol{n}}_0 \cdot \left( \frac{3}{2}(\hat{\boldsymbol{u}}_i \otimes \hat{\boldsymbol{u}}_i - \frac{1}{2}\mathbf{1} \right) \cdot \hat{\boldsymbol{n}}_0 \right] \right\rangle \\ &= \sum_{i=1}^{N} \langle [\hat{\boldsymbol{n}}_0 \cdot \mathbf{Q} \cdot \hat{\boldsymbol{n}}_0] \rangle \,, \end{aligned} \tag{1.2}$$

where $\otimes$ is the dyadic product, $\mathbf{1}$ is the unit tensor. The so-called alignment tensor [30]

is defined as

$$\mathbf{Q} \equiv \frac{1}{2} \sum_{i=1}^{N} \langle [3\hat{\boldsymbol{u}}_i \otimes \hat{\boldsymbol{u}}_i - \mathbf{1}] \rangle \,. \tag{1.3}$$

Therefore, $\mathbf{Q}$ is a real, symmetric, and traceless second rank tensor which can be represented by a $3 \times 3$ matrix. To calculate the nematic order parameter one has to solve the eigenvalue equation

$$\mathbf{Q} \cdot \hat{\boldsymbol{n}}_n = \lambda_n \hat{\boldsymbol{n}}_n \tag{1.4}$$

where $\lambda_n$ is the $n$-th eigenvalue and $\hat{\boldsymbol{n}}_n$ the associated eigenvector. The nematic order parameter $S$ is defined as the largest eigenvalue and the associated eigenvector as the director $\hat{\boldsymbol{n}}_0$. For perfect alignment $S = 1$, whereas $S = 0$ for no orientational order.

## 1.5 Landau-de Gennes theory

The nematic order parameter $S$ can be used to quantitatively describe the phase transition between a phase with no orientational order, the so-called isotropic phase, and a phase with orientational order, the nematic phase in the context of this thesis. Landau developed a general phenomenological theory for phase transitions [33]. Landau's theory describes a temperature-driven phase transition from an ordered state at low temperature to a less ordered phase at higher temperature. Hence, the nematic order parameter is fit to quantitatively describe the isotropic-nematic phase transition for liquid crystals, which was used by De Gennes to develop a phenomenological description on the basis of the Landau theory of phases transitions [30]. The resulting Landau-de Gennes theory is rather simple but captures the most important aspects of the isotropic-nematic phase transition.

The Landau-de Gennes theory assumes that the nematic order parameter in the nematic phase but close to the nematic-isotropic phase transition is small. Therefore, the difference in free energy of the two phases can be expanded in terms of $S$. Up to the fourth order, the free energy can be expanded as

$$F(S) = F_0 + \frac{3}{4} A(T) S^2 - \frac{1}{4} B(T) S^3 + \frac{9}{16} C(T) S^4, \tag{1.5}$$

where $A(T)$, $B(T)$ and $C(T)$ are coefficients. There is no linear term in the expansion. This is to ensure that the state of minimum of $F$ is the state of $S = 0$, hence isotropic. Additionally, the nematic-isotropic phase transition is known to be of "weakly first order" [30]. Thus, the expression for the free energy includes a term of order $S^3$ predicting a discontinuous transition.

We have no knowledge about the coefficients $A(T)$, $B(T)$ and $C(T)$ a priori. Therefore, in a agreement with molecular theories [30], we postulate $A(T) \simeq a(T - T^*)$ and higher order coefficients $B(T)$ and $C(T)$ are assumed to be independent of temperature. Here $T^*$ is the temperature of the spinodal. Below $T^*$ the isotropic phase becomes com-

pletely unstable. One can rationalize the term $A(T) \simeq a(T - T^*)$ in the following manner: For $B = 0$ the transition is continuous and $A(T)$ must vanish at the transition point $T^*$. This is due to the fact that the isotropic phase $S = 0$ corresponds only to a stable minimum if $A > 0$, while in the nematic phase $S \neq 0$ corresponds only to a minimum if $A < 0$. Because $A(T)$ is positive on one side of the transition and negative on the other it has to vanish on the transition point itself.

Figure 3 shows the family of curves obtained from Eq. 1.5. For temperatures above the isotropic-nematic phase transition $T > T_{IN}$ the global minimum corresponds to the isotropic phase ($S = 0$). If $T = T_{IN}$ the isotropic and nematic phase coexist. Consequently, for temperatures below the isotropic-nematic phase transition $T < T_{IN}$ the global minimum of $F$ corresponds to the nematic phase and is shifted to higher values of $S$. Below the spinodal temperature $T^*$ only the nematic phase exists [28–30].

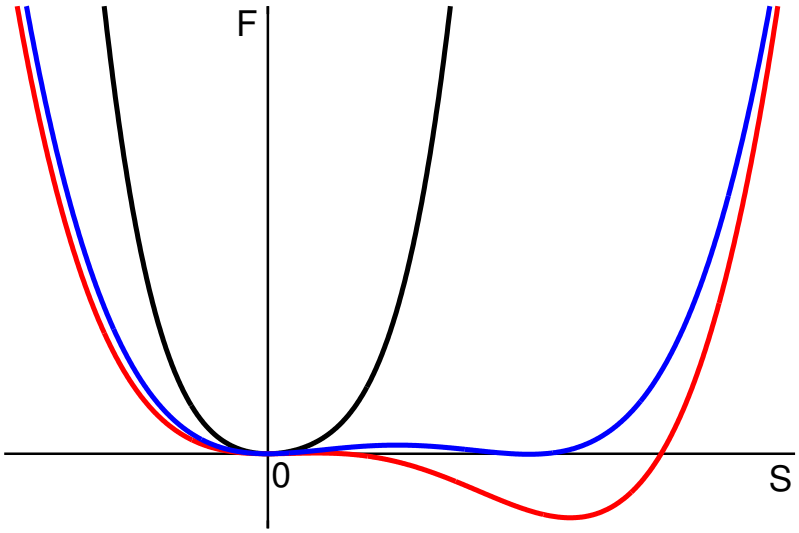


Figure 3: Free energy $F$ as a function of the nematic order parameter $S$ [see Eq. 1.5] for different temperatures $T$. $T > T_{IN}$ (—), $T = T_{IN}$ (—), and $T = T^*$ (—).

## 1.6 Defect topologies

In the previous two chapters we have considered global variables characterizing the nematic order and the free energy of the corresponding liquid-crystal phase. However, the nematic order can be perturbed locally on the molecular scale leading to so-called defect topologies. Topological defects are characterized by some core region, which can be in the shape of a point or line, where the nematic order is destroyed. From a strictly theoretical approach treating the liquid crystal as a continuum a defect is a singularity which cannot be remedied

with an infinite amount of infinitesimal changes of the director field. Furthermore, the nematic order parameter $S$ is not defined in this singularity and approaches zero in its vicinity. However, in computer simulations based on molecules or experiments such a singularity cannot be observed and the defect core has a finite size in the order of the molecular scale. We consider local changes in the nematic order in terms of the local nematic director $\hat{\boldsymbol{n}}(\boldsymbol{r})$ and the local nematic order parameter $S(\boldsymbol{r})$. In Sec. 1.4 we have already calculated the global nematic order parameter $S$ and the global nematic director $\hat{\boldsymbol{n}}_0$ with the aid of the alignment tensor $\mathbf{Q}$. The local quantities are obtained in the same manner and the local alignment tensor is defined as

$$\mathbf{Q}(\boldsymbol{r}) \equiv \frac{1}{2\rho(\boldsymbol{r})} \sum_{i=1}^{N} \langle [3\hat{\boldsymbol{u}}_i \otimes \hat{\boldsymbol{u}}_i - \mathbf{1}]\, \delta(\boldsymbol{r} - \boldsymbol{r}_i) \rangle \tag{1.6}$$

where $\boldsymbol{r}_i$ is the center-of-mass position of molecule $i$, $\delta(\boldsymbol{r})$ is the Dirac delta distribution and

$$\rho(\boldsymbol{r}) = \left\langle \sum_{i=1}^{N} \delta(\boldsymbol{r} - \boldsymbol{r}_i) \right\rangle \tag{1.7}$$

is the local number density. Again the local nematic order parameter $S(\boldsymbol{r})$ is defined as the largest eigenvalue and the associated eigenvector as the local director $\hat{\boldsymbol{n}}(\boldsymbol{r})$.

In a liquid-crystal sample defects can emerge, caused for example by external influences such as confining surfaces, external fields or colloidal particles. The defect topologies arising around a colloidal particle will be addressed in Sec. 2.8. However, also a bulk liquid crystal sample is subject to defects and not all molecules point in the same direction along the global director $\hat{\boldsymbol{n}}_0$. In fact, the orientation of $\hat{\boldsymbol{n}}_0$ varies in space over a very large distance compared to the molecular scale. This leads to the well known Schlieren textures [34]. Thus, within the nematic liquid crystal the local director $\hat{\boldsymbol{n}}(\boldsymbol{r})$ can change abruptly in the vicinity of a defect region. It is impossible to determine the exact orientation of $\hat{\boldsymbol{n}}(\boldsymbol{r})$ in this region. Hence, this area represents a defect in the order of the nematic liquid crystal. The most common types of liquid-crystal defects are point and line defects.

Point defects are less common than line defects. They can occur for instance in liquid-crystal droplets. The most simple example for a point defect would be a droplet where molecules are constrained to align perpendicular to the surface. Therefore, in the center of the droplet a point defect occurs. However, one can easily imagine multiple scenarios creating a line defect. For example, a nematic liquid crystal in a capillary tube where molecules are constraint to align perpendicular to the surface most likely exhibits a line defect. Because line defects represent a *discontinuity* in the *inclination* of the director they are referred to as *disclinations*. There exist a variety of different types of disclinations. Figure 4 shows a two-dimensional representation of common disclinations. To distinguish them the director configuration is examined in the plane perpendicular to

the direction of the line defect. Each configuration is assigned a value for the strength $s$ of the disclination to classify them. Sometimes $s$ is also referred to as the winding number since it also represents the number of rotations by 360° of $\hat{\boldsymbol{n}}(\boldsymbol{r})$ along one closed circuit around the core of the defect [see Fig. 4]. The sign of $s$ is positive for counter-clockwise rotations, consistent with the mathematical definition of the direction of rotation [27, 35].

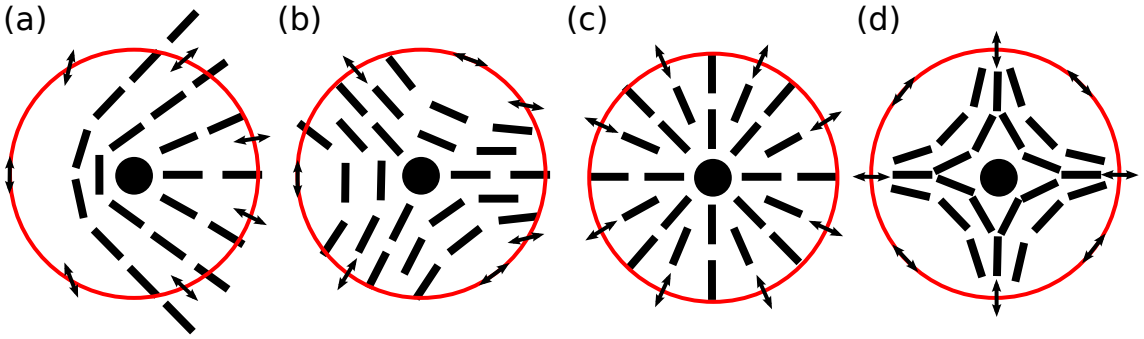


Figure 4: Graphical two-dimensional representation of different types of disclinations in a nematic liquid crystal, for strength (a) $s = 1/2$, (b) $s = -1/2$, (c) $s = 1$ and (d) $s = -1$. Lines represent the local director $\hat{\boldsymbol{n}}(\boldsymbol{r})$ and the defect topologies are represented by a black dot. The red circle and the double headed arrow serve as a visual aid in order to determine the strength of the defect.

## 1.7 Frank free energy

In the vicinity of a topological defect the local director $\hat{\boldsymbol{n}}(\boldsymbol{r})$ can change abruptly. However, in the far field region of the defect $\hat{\boldsymbol{n}}(\boldsymbol{r})$ changes slowly in space with respect to $\hat{\boldsymbol{n}}_0$. Additionally, external constraints such as electric or magnetic fields can cause local perturbations of $\hat{\boldsymbol{n}}_0$. Figure 5 shows the three most common deformations of the nematic phase: splay, twist and bend. These deformations occur on a much larger length scale than a typical molecular one. Hence, it is feasible to describe the deformation with the aid of a continuum theory neglecting the structure at the molecular scale. The distorted state may then be described entirely in terms of the local director $\hat{\boldsymbol{n}}(\boldsymbol{r})$ which is assumed to vary smoothly with $\boldsymbol{r}$. One can then define a free energy density $f_d(\boldsymbol{r})$ due to the distortion of $\hat{\boldsymbol{n}}(\boldsymbol{r})$ which vanishes for the unperturbed nematic liquid crystal where $\nabla\hat{\boldsymbol{n}}(\boldsymbol{r}) = 0$.

Such a theory was initiated by Oseen [18] and Zöcher [36] and later revised by Frank [19]. The free energy density is expanded up to quadratic order in the gradient of the local director $\nabla\hat{\boldsymbol{n}}(\boldsymbol{r})$. If one accounts for the head-tail symmetry, as well as the axial symmetry of nematic liquid crystals it turns out that all rotationally invariant linear terms in $\nabla\hat{\boldsymbol{n}}(\boldsymbol{r})$ vanish. The resulting fundamental formula the so-called Frank free energy density, may

be expressed as

$$f_d(\boldsymbol{r}) = \frac{1}{2}K_1(\nabla \cdot \hat{\boldsymbol{n}}(\boldsymbol{r}))^2 + \frac{1}{2}K_2[\hat{\boldsymbol{n}}(\boldsymbol{r}) \cdot (\nabla \times \hat{\boldsymbol{n}}(\boldsymbol{r}))]^2 + \frac{1}{2}K_3[\hat{\boldsymbol{n}}(\boldsymbol{r}) \times (\nabla \times \hat{\boldsymbol{n}}(\boldsymbol{r}))]^2, \quad (1.8)$$

where $K_1$, $K_2$ and $K_3$ are elastic constants corresponding to the splay, twist and bend deformations, respectively [see Fig. 5]. For most liquid-crystal compounds the bend deformation is larger than the other two. This is due to the fact that a liquid crystal, composed of elongated and stiff molecules, needs more energy to bend than to splay or even twist. However, in most cases all three elastic constants are of the same order of magnitude. Therefore it is useful to apply the one constant approximation $K = K_1 = K_2 = K_3$. Thus, because $(\nabla \times \hat{\boldsymbol{n}}(\boldsymbol{r}))^2 \equiv [\hat{\boldsymbol{n}}(\boldsymbol{r}) \cdot (\nabla \times \hat{\boldsymbol{n}}(\boldsymbol{r}))]^2 + [\hat{\boldsymbol{n}}(\boldsymbol{r}) \times (\nabla \times \hat{\boldsymbol{n}}(\boldsymbol{r}))]^2$, Eq. 1.8 takes the form

$$f_d(\boldsymbol{r}) = \frac{1}{2}K[(\nabla \cdot \hat{\boldsymbol{n}}(\boldsymbol{r}))^2 + (\nabla \times \hat{\boldsymbol{n}}(\boldsymbol{r}))^2]. \quad (1.9)$$

The one-constant approximation is certainly a trade-off between simplicity and accuracy. We will show in Sec. 5.2 that this approximation is quite valid for the model potential studied in this work [30].

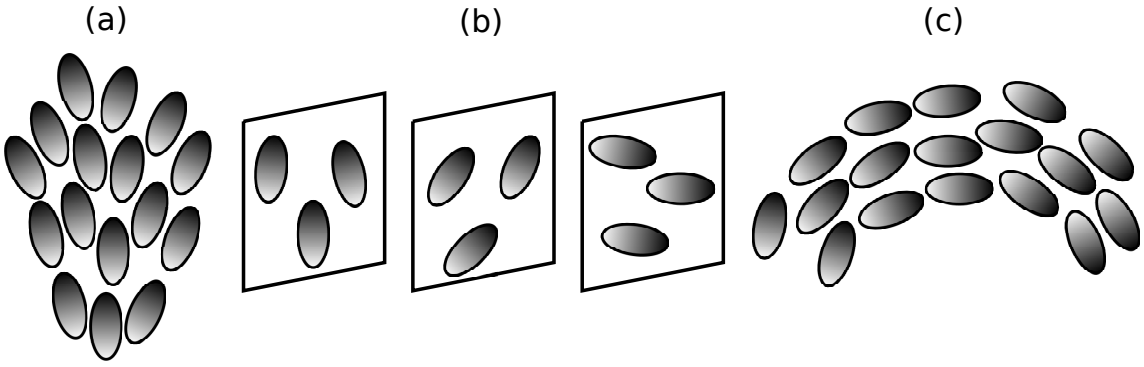


Figure 5: Graphical representation of the most common deformations of a nematic liquid crystal: (a) splay, (b) twist and (c) bend.

## 1.8 Elastic constants

It is possible to generate pure splay, twist or bend deformations. The elastic constants must be positive, otherwise an ideal unperturbed nematic phase would not correspond to a minimum of the Frank free energy. The values of the elastic constants depend strongly on temperature. In fact, for increasing temperature their values decrease, but their ratio remains approximately the same. Here we are going to focus on how to obtain the elastic constants from a molecular dynamics simulation.

The elastic constants can be obtained by considering the fluctuations $\delta\boldsymbol{n}(\boldsymbol{r})$ of the

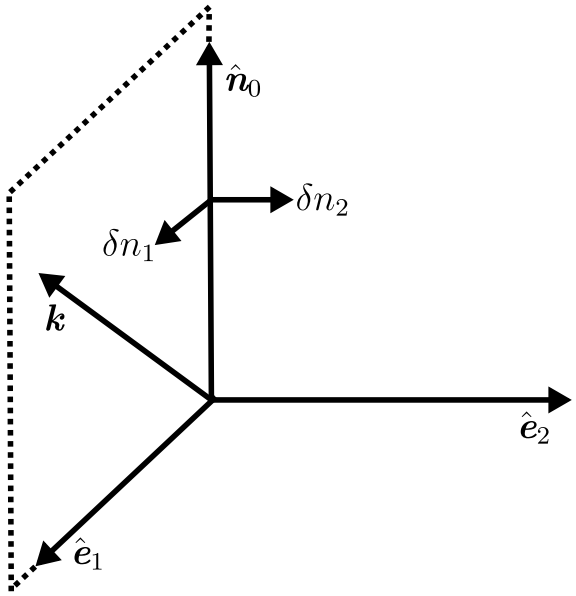


Figure 6: Graphical representation of the two uncoupled modes $\delta n_1$ and $\delta n_2$. The director $\hat{\boldsymbol{n}}_0$ is perpendicular to the unit vectors $\hat{\boldsymbol{e}}_1$ and $\hat{\boldsymbol{e}}_2$. The wave vector $\boldsymbol{k}$ is chosen in the 1-3 plane.

director. For small deviations from the equilibrium configuration $\hat{\boldsymbol{n}}_0$ we can write

$$\hat{\boldsymbol{n}}(\boldsymbol{r}) = \hat{\boldsymbol{n}}_0 + \delta\boldsymbol{n}(\boldsymbol{r}), \tag{1.10}$$

where $\hat{\boldsymbol{n}}_0 \cdot \delta\boldsymbol{n}(\boldsymbol{r}) = 0$ in order to guarantee that $|\hat{\boldsymbol{n}}(\boldsymbol{r})|^2 = 1$. Thus, $\delta\boldsymbol{n}(\boldsymbol{r})$ has two transverse components, $\delta n_1$ and $\delta n_2$, with respect to $\hat{\boldsymbol{n}}_0$ [see Fig. 6]. Both components represent combinations of the known deformations [see Sec. 1.7], where $\delta n_1$ represents a bend-splay deformation and $\delta n_2$ corresponds to a bend-twist deformation. We will derive in the following the connection between director fluctuations and the elastic constants starting from the Frank free energy. Rewriting Eq. 1.8 for $\hat{\boldsymbol{n}}(\boldsymbol{r})$ along the $z$-axis and integrating over the volume $V$ of the system one obtains the Frank free energy

$$F = \frac{1}{2}\int_V \left[ K_1 \left( \frac{\partial n_1}{\partial x_1} + \frac{\partial n_2}{\partial x_2} \right)^2 + K_2 \left( \frac{\partial n_1}{\partial x_2} - \frac{\partial n_2}{\partial x_1} \right)^2 + K_3 \left( \frac{\partial n_1}{\partial x_3} - \frac{\partial n_2}{\partial x_3} \right)^2 \right] \mathrm{d}^3\boldsymbol{r}, \tag{1.11}$$

where the indeces 1, 2, 3 refer to Cartesian components. It is convenient to work with the Fourier transforms, but to determine the expression of $F$ in Fourier space is rather lengthy, albeit straightforward. Thus, we will derive the expression only for contributions describing the splay deformation. The expressions in Fourier space for the twist and bend

contributions can be derived in the same fashion. The free energy then takes the form

$$F_{splay} = \frac{1}{2}\int_V \left[K_1\left(\frac{\partial n_1}{\partial x_1} + \frac{\partial n_2}{\partial x_2}\right)^2\right] \mathrm{d}^3\boldsymbol{r}. \tag{1.12}$$

We introduce the Fourier transform of the director $\hat{\boldsymbol{n}}(\boldsymbol{r})$

$$\tilde{n}_\alpha(\boldsymbol{k}) = \int_V n_\alpha(\boldsymbol{r}) \exp[-i\boldsymbol{k}\cdot\boldsymbol{r}]\mathrm{d}^3\boldsymbol{r}, \tag{1.13}$$

where $\alpha = 1, 2, 3$ and $\boldsymbol{k}$ is the wave vector. The inverse transformation is

$$n_\alpha(\boldsymbol{r}) = \frac{1}{(2\pi)^3}\int \tilde{n}_\alpha(\boldsymbol{k}) \exp[i\boldsymbol{k}\cdot\boldsymbol{r}]\mathrm{d}^3\boldsymbol{k}. \tag{1.14}$$

Substituting for $n_\alpha(\boldsymbol{r})$ in Eq. 1.12 leads to

$$F_{splay} = \frac{K_1}{2}\frac{1}{(2\pi)^6}\int_V\int\int \left[-\tilde{n}_1(\boldsymbol{k})k_1\tilde{n}_1(\boldsymbol{k}')k_1' + 2\tilde{n}_1(\boldsymbol{k})k_1\tilde{n}_2(\boldsymbol{k})k_2 - \tilde{n}_2(\boldsymbol{k})k_2\tilde{n}_2(\boldsymbol{k}')k_2'\right] \times \exp[i(\boldsymbol{k}+\boldsymbol{k}')\cdot\boldsymbol{r}]\mathrm{d}^3\boldsymbol{k}\mathrm{d}^3\boldsymbol{k}'\mathrm{d}^3\boldsymbol{r}. \tag{1.15}$$

Applying the known properties of the Dirac delta distribution $\delta(x)$

$$\int_V \exp[i(\boldsymbol{k}+\boldsymbol{k}')\cdot\boldsymbol{r}]\mathrm{d}^3\boldsymbol{r} = (2\pi)^3\delta(\boldsymbol{k}+\boldsymbol{k}') \tag{1.16}$$

and

$$\int f(\boldsymbol{k}')\delta(\boldsymbol{k}+\boldsymbol{k}')\mathrm{d}^3\boldsymbol{k}' = f(-\boldsymbol{k}) \tag{1.17}$$

results in

$$F_{splay} = \frac{K_1}{2}\frac{1}{(2\pi)^3}\int\int \left[-\tilde{n}_1(\boldsymbol{k})k_1\tilde{n}_1(\boldsymbol{k}')k_1' + 2\tilde{n}_1(\boldsymbol{k})k_1\tilde{n}_2(\boldsymbol{k})k_2 - \tilde{n}_2(\boldsymbol{k})k_2\tilde{n}_2(\boldsymbol{k}')k_2'\right] \times \delta(\boldsymbol{k}+\boldsymbol{k}')\mathrm{d}^3\boldsymbol{k}\mathrm{d}^3\boldsymbol{k}' \tag{1.18}$$

$$= \frac{K_1}{2}\frac{1}{(2\pi)^3}\int \left[\tilde{n}_1(\boldsymbol{k})\tilde{n}_1(-\boldsymbol{k})k_1^2 + 2\tilde{n}_1(\boldsymbol{k})k_1\tilde{n}_2(\boldsymbol{k})k_2 + \tilde{n}_2(\boldsymbol{k})\tilde{n}_2(-\boldsymbol{k})k_2^2\right]\mathrm{d}^3\boldsymbol{k}. \tag{1.19}$$

Because $\tilde{n}_\alpha(-\boldsymbol{k}) = \tilde{n}_\alpha^*(\boldsymbol{k})$ and $\tilde{n}_\alpha(\boldsymbol{k})\tilde{n}_\alpha^*(\boldsymbol{k}) = |\tilde{n}_\alpha(\boldsymbol{k})|^2$ the final result may then be cast as

$$F_{splay} = \frac{K_1}{2}\frac{1}{(2\pi)^3}\int (k_1\tilde{n}_1 + k_2\tilde{n}_2)^2\mathrm{d}^3\boldsymbol{k} \tag{1.20}$$

using shorthand notation $|\tilde{n}_\alpha(\boldsymbol{k})| = \tilde{n}_\alpha$. Transforming the twist and bend contributions of Eq. 1.11 into Fourier space as well leads to the complete Fourier transform of the Frank

free energy which can be written as a discrete sum

$$F = \frac{1}{2}\frac{1}{V}\sum_{k} K_1(k_1\tilde{n}_1 + k_2\tilde{n}_2)^2 + K_2(k_2\tilde{n}_1 - k_1\tilde{n}_2)^2 + K_3k_3^2(\tilde{n}_1^2 + \tilde{n}_2^2). \tag{1.21}$$

We can define a new coordinate system **1**,**2**,**3** where the global director is $\hat{\boldsymbol{n}}_0 = (0,0,1)^T$ and the wave vector $\boldsymbol{k} = (k_1, 0, k_3)^T$ is chosen in the 1-3 plane [see Fig. 6], where the transcript $T$ denotes the transpose of the vector. Additionally, we choose the unit vectors $\hat{\boldsymbol{e}}_1$ and $\hat{\boldsymbol{e}}_2$, with $\hat{\boldsymbol{e}}_1$ in the $(\boldsymbol{k}, \hat{\boldsymbol{n}}_0)$ plane and $\hat{\boldsymbol{e}}_2$ normal to it. Hence, one obtains

$$\boldsymbol{k} = k_1\hat{\boldsymbol{e}}_1 + k_3\hat{\boldsymbol{n}}_0 \tag{1.22}$$

and Eq. 1.21 can be rewritten as

$$F = \frac{1}{2}\frac{1}{V}\sum_{k}\sum_{\alpha=1}^{2}\left[|\tilde{n}_\alpha(\boldsymbol{k})|^2(K_3k_3^2 + K_\alpha k_1^2)\right]. \tag{1.23}$$

Both degrees of freedom $\alpha = 1, 2$ are completely decoupled. We have shown in Sec. 1.7 that the Frank free energy [see Eq. 1.8] describes the elastic deformation of $\hat{\boldsymbol{n}}(\boldsymbol{r})$. From a molecular point of view the deformation is achieved through the rotation of molecules [see Fig. 5]. Here, $\tilde{\boldsymbol{n}}(\boldsymbol{k})$ is a measure of the local fluctuations of $\hat{\boldsymbol{n}}(\boldsymbol{r})$ [see Eq. 1.10]. Again, these deviations from $\hat{\boldsymbol{n}}(\boldsymbol{r})$ are reflected by rotations of the molecules. Hence, $\tilde{n}_1(\boldsymbol{k})$ and $\tilde{n}_2(\boldsymbol{k})$ represent orientational degrees of freedom and the energy equipartition theorem can be applied. This leads to

$$\left\langle|\tilde{n}_1(\boldsymbol{k})|^2\right\rangle = \frac{Vk_\mathrm{B}T}{K_3k_3^2 + K_1k_1^2}, \tag{1.24}$$

$$\left\langle|\tilde{n}_2(\boldsymbol{k})|^2\right\rangle = \frac{Vk_\mathrm{B}T}{K_3k_3^2 + K_2k_1^2}, \tag{1.25}$$

where $\langle\ldots\rangle$ is again the ensemble or time average and $k_\mathrm{B}$ is the Boltzmann constant [37].

In order to obtain the elastic constants from molecular dynamics simulations it is more convenient to consider fluctuations of the Fourier transform of the alignment tensor $\mathbf{Q}(\boldsymbol{r})$ [see Eq. 1.3]. To rewrite Eqs. 1.24 and 1.25 in a tensorial form we use the relation

$$\mathrm{Q}_{\alpha\beta} = \frac{1}{2}S(3n_\alpha n_\beta - \delta_{\alpha\beta}), \tag{1.26}$$

where $S$ is the nematic order parameter. With $\hat{\boldsymbol{n}}_0$ pointing along the $z$-axis and $\delta\hat{\boldsymbol{n}}$ perpendicular to it [see Fig. 6] the local director corresponds to $\hat{\boldsymbol{n}}(\boldsymbol{r}) = (\delta n_1, \delta n_2, 1)^T$. Inserting $\hat{\boldsymbol{n}}(\boldsymbol{r})$ into Eq. 1.26 results in $\mathrm{Q}_{13} = \frac{3}{2}S\delta n_1$ and $\mathrm{Q}_{23} = \frac{3}{2}S\delta n_2$. Therefore, considering the Fourier transform of $\hat{\boldsymbol{n}}(\boldsymbol{r})$, $\tilde{\boldsymbol{n}}(\boldsymbol{k}) = (\tilde{n}_1, \tilde{n}_2, 1)^T$, one can rewrite Eqs. 1.24 and 1.25 as

[38, 39]

$$\left\langle \left| \tilde{\mathrm{Q}}_{13}(\boldsymbol{k}) \right|^2 \right\rangle = \frac{\frac{9}{4} S^2 V k_\mathrm{B} T}{K_1 k_1^2 + K_3 k_3^2}, \tag{1.27}$$

$$\left\langle \left| \tilde{\mathrm{Q}}_{23}(\boldsymbol{k}) \right|^2 \right\rangle = \frac{\frac{9}{4} S^2 V k_\mathrm{B} T}{K_2 k_1^2 + K_3 k_3^2}, \tag{1.28}$$

where $\tilde{\mathbf{Q}}(\boldsymbol{k})$ is the Fourier transform of the alignment tensor, defined as

$$\tilde{\mathbf{Q}}(\boldsymbol{k}) = \int_V \mathbf{Q}(\boldsymbol{r}) \exp(i\boldsymbol{k} \cdot \boldsymbol{r}) \mathrm{d}^3 \boldsymbol{r}. \tag{1.29}$$

Equations 1.27 and 1.28 are valid and linear functions of $k_1^2$ and $k_3^2$ in the limit of low $k$ because the elastic constants are defined only for long-wavelength director fluctuations. To extract the elastic constants from Eqs. 1.27 and 1.28 one may fit

$$E_{13}(k_1^2, k_3^2) \equiv \frac{\frac{9}{4} S^2 V k_\mathrm{B} T}{\left\langle \left| \tilde{Q}_{13}(\boldsymbol{k}) \right|^2 \right\rangle} = K_1 k_1^2 + K_3 k_3^2, \tag{1.30}$$

$$E_{23}(k_1^2, k_3^2) \equiv \frac{\frac{9}{4} S^2 V k_\mathrm{B} T}{\left\langle \left| \tilde{Q}_{23}(\boldsymbol{k}) \right|^2 \right\rangle} = K_2 k_1^2 + K_3 k_3^2, \tag{1.31}$$

to functions of $k_1^2$ and $k_3^2$. $E_{13}$ and $E_{23}$ vanish as $V \to \infty$, hence values at the origin, $E_{13}(0,0)$ and $E_{23}(0,0)$ should be set to zero and one should extrapolate to $k \to 0$. Figure 15 in Sec. 5.2 shows plots used for the calculation of the Frank elastic constants $K_1$, $K_2$ and $K_3$. The elastic constants may then be applied to Eq. 1.8 [40–42].

## 1.9 Effects of flow on topological defects

The above discussion gives a general introduction into the field of liquid crystals. Additionally, we have introduced a selection of key concepts which are helpful to understand the remainder of this work. Starting from these fundamentals we present the aims of this work in the remaining two sections of this chapter.

Nematic liquid crystals are fluids characterized by a high degree of orientational order along one common direction, the global director $\hat{\boldsymbol{n}}_0$, and no long-range positional order. One can imagine a colloidal particle dispersed in a nematic liquid-crystal host phase has great effects on the physical properties of the host phase. This is due to the fact that the colloid disturbs the orientational order of the nematic host phase. More specifically, the alignment of liquid-crystal molecules on the colloidal surface is not everywhere in agreement with the global orientational order along $\hat{\boldsymbol{n}}_0$. These local discrepancies can be measured by a local quantity such as the director field $\hat{\boldsymbol{n}}(\boldsymbol{r})$. Due to the local distortions

in the orientational order of the nematic liquid crystal defect topologies arise. To date, a variety of defect topologies have been observed. The most common ones are the Boojum defect, the Saturn ring defect and the hedgehog defect [43, 44]. However, the distortions of the director field $\hat{\boldsymbol{n}}(\boldsymbol{r})$ also cause long-range, anisotropic forces. These effective forces can lead to interesting phenomena such as self-assembly of the colloids [45, 46] which can be employed for photonic band-gap devices [47–49].

Modern microfluidic devices utilize flow to manipulate and control fluids and cargos [50]. So far, the majority of microfluidic applications is based on isotropic liquids. A relatively new and quickly emerging field is the investigation of anisotropic liquids, such as nematic liquid crystals under microfluidic conditions. The field is at an early stage but has promising future applications for instance in chemical synthesis, biological analysis, optics, and information technology [51]. Because of their high tunability, nematic liquid crystals have attracted considerable interest as a replacement for the isotropic liquid in microfluidics [52]. For instance, nematic liquid crystal flow can be driven by thermal expansion [53] or by pressure [54]. Microflows of nematic liquid crystals can induce transitions in the director field [55] or can even be utilized for guided transport of microscopic cargo such as colloids [2]. Furthermore, flow of nematic liquid crystals can be manipulated with electric fields [56] or mechanically with an optofluidic modulator [57].

We combine both fields and study in detail the effect of flow on defect topologies arising around a colloidal particle dispersed in a nematic liquid crystal. So far scientific attention on this matter has been rather scare and unsatisfactory from a theoretical perspective. The first step was undertaken by Billeter and Pelcovits [58]. They performed a falling-ball experiment with the aid of molecular dynamics simulations. However, because of the lack of powerful computers at the time, they were only able to show that high driving forces acting on a colloidal particle distort a Saturn ring defect topology. Stark and Ventzki [59] showed with a comprehensive computational study that a hedgehog defect moves upstream against the direction of flow. They also predicted that flow could turn a hedgehog defect into a Saturn ring defect. Later Fukuda *et al.* [60] and Yoneya *et al.* [61], with a related computational study, could not observe such a transition and found in contrast that the hedgehog defect moves downstream along with the flow. Additionally, Yoneya *et al.* [61] were able to show that a Saturn ring defect is pushed downstream, escaping from the particle and finally shrinking to a hyperbolic hedgehog defect. Utilizing again computational methods Araki and Tanaka [62] could reproduce the detachment of the Saturn ring defect from the colloid along the direction of flow. Furthermore, they reported a strong deformation of the Saturn ring defect when the flow direction is perpendicular to the global director. With numerical simulations Zhou *et al.* [63] could show as well that flow sweeps a hedgehog defect and a Saturn ring defect downstream. So far only Khullar *et al.* [1] have performed experimental studies on the subject. They found that defect structures around rising bubbles and droplets move downstream along the direction

of flow. In addition, they also observed the transition from a Saturn ring defect into a hedgehog defect due to flow. However, Gettelfinger *et al.* [64] recently reported molecular dynamics simulations showing that the Saturn ring defect around a solid nanoparticle moves upstream, while the Saturn ring defect around a nanodroplet moves downstream. Hence, there is still disagreement on the direction of motion of defect topologies around a colloid with respect to the direction of flow.

In Chap. 5 we study with the aid of nonequilibrium molecular dynamics simulations a nematic liquid crystal flowing around a colloidal particle. We pay particular attention to the application of a suitable thermostat in a nonequilibrium state. It is of crucial importance to remove viscous heat from the fluid without introducing artificial dynamical states [65] in order to obtain reliable results. We employ a local Galilean-invariant thermostat first proposed by Stoyanov and Groot [66] which uses a momentum-conserving pairwise force to control the temperature. The thermostat is a flexible and robust method for nonequilibrium molecular dynamics simulations of spatially inhomogeneous systems. We find from our simulations that a Saturn defect around a homogeneous colloid is deformed and deflected downstream along with the direction of flow. Our results are in agreement with experimental studies [1] and suggest that the earlier upstream shift of this defect topology [64] might be an artifact caused by improperly thermostating the nonequilibrium system. Additionally, we study colloids with a heterogeneous surface, so-called Janus colloids, consisting of two different patches under flow conditions. Both patches constrain the liquid-crystal molecules to different orientations with respect to the colloidal surface. Experimental [67] and theoretical [68] studies report a variety of new and interesting defect topologies for a Janus colloid dispersed in a nematic liquid crystal. We present the first numerical study of these defect structures under flow conditions and show that they can be modulated by flow as well.

Moreover, in Sec. 5.6 we present a more detailed take on ring shaped defects, such as the Saturn ring defect, under hydrodynamic flow. The previously described qualitative observations are concluded by a detailed quantitative analysis. More specifically, length, shape and flow-induced displacement of the defects are measured. To that end, we demonstrate that a computation of these quantities is rather straightforward if suitable projections of the defect loops with respect to the direction of flow are utilized. Previous experimental [1] and theoretical [61] work observed the transition of a Saturn ring defect into a hedgehog defect due to flow. From our nonequilibrium molecular dynamics simulations we can estimate this transition quantitatively correlating the length of disclination loops with dimensionless measures of flow. A particular important role in this regard plays the range of the interaction potential between liquid-crystal molecules and colloid which we study in detail in this work.

## 1.10 Hydrodynamic cavitation of anisotropic fluids

Apart from the displacement and deformation of defect topologies cavitation is another interesting flow-induced phenomenon. Cavitation is the nucleation of vapor gas bubbles within a liquid. The phenomenon can be triggered by local heating above the boiling temperature of the liquid or by physical processes that stretch the liquid abruptly below its saturated vapor pressure [69]. Hence, the liquid is subject to tensile stresses. Above a critical value, known as the breaking tension or cavitation threshold [70], cavitation sets in. During the inception of cavitation the liquid is subject to negative pressure. Consequently, this state is thermodynamically metastable [71] and a cavitation bubble forms. The liquid can be driven out of thermodynamic equilibrium by acoustic waves [72], hydrodynamic flows [54], laser induced heating [73] or simply pulling or stretching the liquid under confinement [74]. The lifetime of the vapor bubble from the inception of the cavitation to the implosion of the cavity depends on a range of parameters such as: volume of dissolved gases in the liquid, presence of inclusions, roughness of solid surfaces in contact with the liquid and the pre-existence of nucleation sites.

There exist numerous biomedical and biophysical processes where the inception of a cavity plays a major role. The inception of cavitation is crucial for the performance of mechanical heart valves [75] and necessary to understand how shrimp stun their prey [76], to name a few examples. Furthermore, it is immediately clear from these two examples that in some cases the physical and material parameters are tuned to avoid the inception of cavitation, in others, reaching the cavitation threshold may be the desired goal.

In Sec. 5.9 we focus on the evolution of a cavitation bubble due to a large pressure drop. This is referred to as "hydrodynamic cavitation" in the literature. Hydrodynamic cavitation of de-ionized water in microchannels with a microorifice was extensively investigated by Mishra and Peles [77–79] for large Reynolds numbers. The authors focus on the similarities and differences between cavitation at the macroscopic and microscopic scale. Medrano *et al.* [80] investigated various microfluidic geometries with de-ionized water as well as nanoparticles dispersed into the liquid. A cavitation bubble created through heat in form of a laser pulse was studied by Zwaan *et al.* [81]. However, their main focus was the dynamics of the bubble in a microfluidic system.

The phenomenon of cavitation has also been subject to a few computer simulation-based studies. For instance, molecular dynamics simulations were employed to study the nucleation of cavities in a homogeneous polymer under tensile strain [82] and within polymers containing nanocomposites [83]. In a Lennard-Jones fluid, Baidakov *et al.* [84, 85] used molecular dynamics simulations to study the spontaneous inception of cavitation under negative pressure. With the aid of Monte Carlo simulations Rasmussen *et al.* [86, 87] observed cavitation in homogeneous as well as heterogeneous pores with non-wetting defects for a Lennard-Jones fluid. A non-wetting defect was introduced as a round spot

on the pore wall which does not exert an attractive potential.

The research on cavitation in isotropic liquids is broad and comprehensive. However, in the light of recent biological applications and discoveries, such as electrohydraulic [88] and shock-wave lithotripsy [89], it is necessary to extend research efforts to anisotropic liquids. We will focus on nematic liquid crystals, which constitute a special class of complex non-Newtonian liquids. Studies on cavitation in liquid crystals are scare. Luckhurst [72] studied the disruption of the orientational alignment at the onset of cavitation in a nematic liquid crystal. However, in this study the cavitation was imposed by ultrasound. The only other existing study on the matter focuses on phase transitions in liquid crystals under negative pressure [90]. The cavity is induced by an isochoric cooling of small liquid crystal droplets embedded in a glass forming material. However, any attempt to study flow-induced cavitation in liquid crystals is still missing. This thesis is in part devoted to the first-in-depth study of cavitation in a nematic liquid crystal.

In Sec. 5.9 we study with the aid of nonequilibrium molecular dynamics simulations a nematic liquid crystal flowing around a cylindrical pillar. We are able to observe cavitation and establish its physical principles in anisotropic fluids such as a nematic liquid crystal. Thus, we employ measurements of the local density, pressure and velocity to quantitatively capture the onset of cavitation. Moreover, we measure the size and evolution of the cavitation bubble. Therefore, our nonequilibrium molecular dynamics simulations quantitatively capture the transient and stationary dynamics, and thereby determine the predictors of the phenomenon. On comparing the results with those in the corresponding isotropic phase, we find that the flow speeds for cavitation inception of anisotropic fluids can be less than half of that in isotropic fluids. Furthermore, the flow speed scales inversely with the nematic order parameter.

Additionally, we study a wide range of flow speeds before the onset of cavitation. Our nonequilibrium molecular dynamics simulations are able to reproduce the structural changes within the microfluidic channel of earlier experimental studies [2] performed in a similar geometry.

# 2 Theoretical background

## 2.1 Flow of nematic liquid crystals

In the present work we focus on the flow of nematic liquid crystals. The flow regimes of a nematic liquid crystal differ drastically from that of a conventional, isotropic fluid. There is a mutual coupling between the flow direction, the director orientation and the viscosity. In other words, the translation of the molecules is coupled with the orientational motion of the molecules. Therefore, flow in a nematic liquid crystal can disturb the alignment of the molecules along a common direction, the director $\hat{\boldsymbol{n}}_0$. Furthermore, flow can be induced in a nematic liquid crystal by reorienting the molecules with the aid of an external field. However, it is possible to study most of the properties of a nematic liquid crystal treating it as a continuous medium. We have already discussed continuum approaches for equilibrium systems in Sec. 1.5 and 1.7. There exist also continuum theories to study liquid crystals *out of equilibrium*. A complete continuum description for a nematic liquid crystal under flow was given by Ericksen [91–95], Leslie [96, 97] and Parodi [98], which will be explained further in the following section [30].

## 2.2 Ericksen-Leslie-Parodi theory

Hydrodynamic flow can be described by the Navier-Stokes equation. For a nematic liquid crystal one has to take into account the coupling between the director field and the hydrodynamic flow. This is achieved by the Ericksen-Leslie-Parodi theory, described by a set of equations consisting of a generalization of the Navier-Stokes equations for the fluid velocity $\boldsymbol{v}$ to uniaxial media and a dynamic equation for the director $\hat{\boldsymbol{n}}$. We will not derive the Ericksen-Leslie equations, instead we will focus on the explanation of their meaning. The Ericksen-Leslie equations, which have a basis in Frank elastic theory [see Sec. 1.7], describe the nematodynamic problem via the equations

$$\nabla \cdot \boldsymbol{v} = 0, \tag{2.32}$$

$$\rho \frac{\partial \boldsymbol{v}}{\partial t} + \rho(\boldsymbol{v} \cdot \nabla)\boldsymbol{v} = -\nabla P + \nabla \cdot (\boldsymbol{\sigma}^e + \boldsymbol{\sigma}^v), \tag{2.33}$$

$$\mathbf{0} = \hat{\boldsymbol{n}} \times (\boldsymbol{h}^e - \boldsymbol{h}^v), \tag{2.34}$$

where Eq. 2.32 is the equation of continuity for an incompressible fluid. Equation 2.33 represents the generalized Navier-Stokes equation, where $\rho$ is the density and $P$ is the hydrostatic pressure. The diffusive term can be formally written as a divergence of the stress tensor $\eta \nabla^2 \boldsymbol{v} = \nabla \cdot \boldsymbol{\sigma}$. The stress tensor in Eq. 2.33 consists of an elastic and viscous

term

$$\boldsymbol{\sigma}^e_{ij} = -\frac{\partial f_d}{\partial(\partial_i n_k)}\partial_j n_k, \tag{2.35}$$

$$\begin{aligned}\boldsymbol{\sigma}^v_{ij} &= \alpha_1 n_i n_j n_k n_l A_{kl} + \alpha_2 n_j N_i + \alpha_3 n_i N_j + \alpha_4 A_{ij} \\ &+ \alpha_5 n_j n_k A_{ik} + \alpha_6 n_i n_k A_{jk},\end{aligned} \tag{2.36}$$

where $f_d$ denotes the Frank free energy density [see Eq. 1.8] and $n_i$ is a component of the director. The elasticity of a nematic liquid crystal leads to an elastic contribution in the stress tensor, represented by Eq. 2.35. If the director is perturbed elastic forces arise and therefore hydrodynamic flow can be initiated by this perturbation. Equation 2.36 describes the viscous part of the stress tensor where $A_{ij} = \frac{1}{2}(\partial_i v_j + \partial_j v_i)$ is the symmetrized velocity gradient and $\alpha_i$ are the Leslie coefficients representing viscosities, which will be discussed in more detail in the subsequent section. The Leslie coefficients are linked by Parodi's relation $\gamma_2 = \alpha_2 + \alpha_3 = \alpha_6 - \alpha_5$. For a conventional isotropic fluid the stress tensor $\boldsymbol{\sigma}$ is simply proportional to the symmetrized velocity gradient $\boldsymbol{A}$. Hence, the conventional shear viscosity equals to $\alpha_4/2$ in Eq. 2.36. The uniaxial symmetry in a nematic liquid crystal leads to further terms proportional to $\boldsymbol{A}$ containing the director $\hat{\boldsymbol{n}}$. More specifically, terms including $\alpha_1$, $\alpha_5$ and $\alpha_6$ contribute to the anisotropy of the viscosity. The remaining terms in Eq. 2.36 including $\alpha_2$ and $\alpha_3$ include a second dynamic variable $\boldsymbol{N}$ depending on the time derivative of $\hat{\boldsymbol{n}}$. These contributions represent flow due to the relative rotation of the director field. Hence, both coefficients are coupled to the rotational viscosity $\gamma_1 = \alpha_3 - \alpha_2$ [see Sec. 2.3]. The vector

$$\boldsymbol{N} = \frac{\mathrm{d}\hat{\boldsymbol{n}}}{\mathrm{d}t} - \boldsymbol{\omega} \times \hat{\boldsymbol{n}}, \tag{2.37}$$

describes the rate of change of the director $\hat{\boldsymbol{n}}$ relative to the fluid motion, where $\boldsymbol{\omega} = \frac{1}{2}\nabla \times \boldsymbol{v}$ is the angular velocity.

Additional, approximation can be made to simplify Eq. 2.33. For Stokes flow, meaning low Reynolds numbers $\mathcal{R} \ll 1$ [see Sec. 2.5], advective inertial forces are small. Thus, the convective term $\rho(\boldsymbol{v} \cdot \nabla)\boldsymbol{v}$ can be neglected. Often another simplification, the so-called adiabatic approximation, is applied. More specifically, the velocity field is taken to be stationary, that is $\partial \boldsymbol{v}/\partial t = 0$. This can be justified because the velocity field relaxes almost instantaneously compared to the director field. Equation 2.33 may then be cast as

$$\boldsymbol{0} = -\nabla p + \nabla \cdot (\boldsymbol{\sigma}^e + \boldsymbol{\sigma}^v). \tag{2.38}$$

Finally, Eq. 2.34 specifies that the total torque on the director, due to elastic distortions and viscous processes, is zero. Because the director is a unit vector, that is $\hat{\boldsymbol{n}} \cdot \hat{\boldsymbol{n}} = 1$, only the normal component represents a thermodynamic force driving the director towards

equilibrium. Elastic and and viscous forces may be expressed as

$$h_i^e = \partial_j \frac{\partial f_d}{\partial(\partial_j n_i)} - \frac{\partial f_d}{\partial n_i}, \tag{2.39}$$

$$h_i^v = \gamma_1 N_i + \gamma_2 A_{ij} n_j. \tag{2.40}$$

Equation 2.39 describes the elastic force driving the director field towards equilibrium, whereas Eq. 2.40 is an opposing force specifying the viscous contributions. The first term of Eq. 2.40 defines a viscous force due to the rotation of neighboring molecules with different angular velocities. The second term describes the torque performed on the director by a shear flow. Since the reorientation of the director is a slow process on the molecular time scale, an inertial term for the rotational motion of molecules is not included. In general, the reorientation of the director can be viewed as a viscous process, where elastic energy stored in the director field is dissipated [25, 30, 99].

## 2.3 Mięsowicz viscosities

The anisotropy in the viscosity of a nematic liquid crystal can be described by three different viscosity coefficients. Each coefficient describes one possible orientation of the director $\hat{\boldsymbol{n}}$ with respect to the flow velocity $\boldsymbol{v}$ and the shear $\nabla v$. Figure 7 shows a sketch of the three fundamental geometries. The first experimental measurement of the three fundamental viscosities was performed by Mięsowicz [100]. Thus, they are named Mięsowicz viscosities. In the experiment the director $\hat{\boldsymbol{n}}$ was fixed with a strong magnetic field and a shear flow in the three different geometries was applied [see Fig. 7].

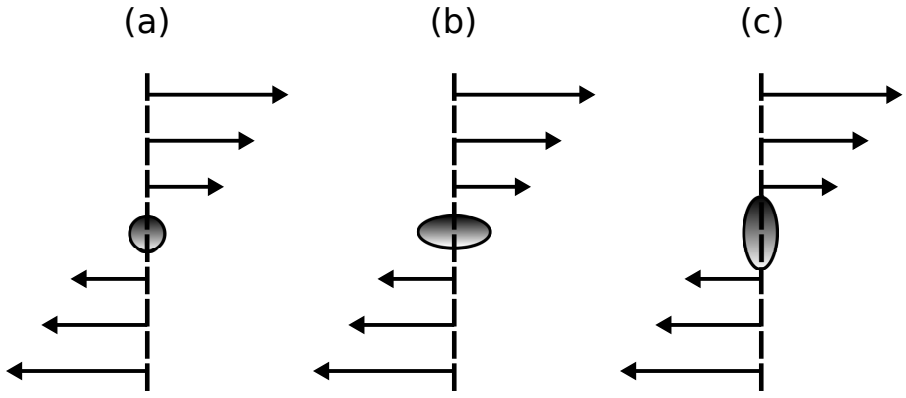


Figure 7: Graphical representation of the flow-director configurations corresponding to the Mięsowicz viscosities: (a) $\eta_a$ ($\hat{\boldsymbol{n}} \perp \boldsymbol{v}$ and $\hat{\boldsymbol{n}} \perp \nabla v$), (b) $\eta_b$ ($\hat{\boldsymbol{n}} \parallel \boldsymbol{v}$ and $\hat{\boldsymbol{n}} \perp \nabla v$), (c) $\eta_c$ ($\hat{\boldsymbol{n}} \perp \boldsymbol{v}$ and $\hat{\boldsymbol{n}} \parallel \nabla v$).

In addition to the three Mięsowicz viscosities nematic liquid crystals posses a fourth viscosity, the rotational viscosity $\gamma_1$. Whereas the three Mięsowicz viscosities are defined in the same fashion as a shear viscosity of an ordinary isotropic fluid, $\gamma_1$ has no counterpart

in isotropic fluids. The rotational viscosity $\gamma_1$ describes the ratio between the viscous torque on the director $\hat{\boldsymbol{n}}$ and the resulting angular velocity of the director rotation.

Within the framework of Ericksen-Leslie-Parodi theory we defined a viscous stress tensor in the previous section [see Eq. 2.36]. The Leslie coefficients of the tensor describe a general shear viscosity

$$\begin{aligned} \eta(\vartheta,\varphi) &= \alpha_1 \sin^2\vartheta\cos^2\vartheta\cos^2\varphi + \frac{1}{2}(-\alpha_2\sin^2\vartheta\cos^2\varphi + \alpha_3\cos^2\vartheta \\ &+ \alpha_4 + \alpha_5\sin^2\vartheta\cos^2\varphi + \alpha_6\cos^2\vartheta), \end{aligned} \tag{2.41}$$

where $\vartheta$ is the angle between $\hat{\boldsymbol{n}}$ and $\boldsymbol{v}$, and $\varphi$ is the angle between $\nabla v$ and the projection of $\hat{\boldsymbol{n}}$ onto the plane perpendicular to $\boldsymbol{v}$. By choosing the values of $\vartheta$ and $\varphi$ in Eq. 2.41 according to the three different geometries [see Fig.7] one obtains the three Mięsowicz viscosities

$$\eta_a = \frac{\alpha_4}{2}, \tag{2.42}$$

$$\eta_b = \frac{\alpha_3+\alpha_4+\alpha_6}{2}, \tag{2.43}$$

$$\eta_c = \frac{-\alpha_2+\alpha_4+\alpha_5}{2}. \tag{2.44}$$

As already stated above the rotational viscosity can be related to the Leslie coefficients via $\gamma_1 = \alpha_3 - \alpha_2$ [30, 52].

## 2.4 Effective viscosity

Apart from the viscosities according to Mięsowicz, discussed in the previous Section, it might be useful to find more general expressions in order to obtain an effective viscosity directly from particle based simulations, like the molecular dynamics simulations studied in this thesis. We consider a model system confined along the $z$-axis by two walls separated by a distance $s_z$. For a steady-state laminar flow the force along the direction of flow, here the $x$-axis, may be written as [30]

$$-\eta\frac{\partial P}{\partial x} = -\frac{\partial^2 v_x(z)}{\partial z^2} + \frac{1}{\delta^2}v_x(z) = 0, \tag{2.45}$$

where $\eta$ is the effective viscosity, $v_x$ is the component of the velocity along the direction of flow and $\delta$ has the dimensions of a length, characterizing the thickness of a boundary layer near the confining walls. Apart from this boundary layer the fluid is assumed to flow at a constant speed. The general solution of the differential equation 2.45 may be cast as

$$v_x(z) = -\frac{\delta^2}{\eta}\frac{\partial P}{\partial x} + C_1 e^{z/\delta} + C_2 e^{-z/\delta}. \tag{2.46}$$

Applying the boundary conditions $v_x(z = \pm s_z) = 0$ representing the two confining walls, leads to a single constant $C = C_1 + C_2$. Where

$$C = \frac{\delta^2}{\eta}\frac{\partial P}{\partial x}\frac{1}{\cosh(s_z/2\delta)}, \tag{2.47}$$

and the complete solution of Eq. 2.45 is

$$v_x(z) = -\frac{\delta^2}{\eta}\frac{\partial P}{\partial x}\left(1 - \frac{\cosh(z/\delta)}{\cosh(s_z/2\delta)}\right). \tag{2.48}$$

Equation 2.48 describes a plug flow. However, it can be shown that it also applies to Poiseuille flow as a limiting case. In contrast to plug flow, Poiseuille flow is characterized by a parabolic flow profile and does not posses a regime where the flow speed is constant. Hence, $\delta$ diverges and $\delta \gg s_z$. Therefore, the linear term in Eq. 2.45 vanishes and the complete solution of the differential equation, subject to the same boundary conditions, may be cast as

$$v_x(z) = \frac{1}{2\eta}\frac{\partial P}{\partial x}\left[z^2 - \frac{s_z^2}{4}\right], \tag{2.49}$$

exhibiting the typical parabolic profile. Eq. 2.49 clearly describes the variation of the velocity component $v_x$ as a function of position $z$ relative to the walls for Poiseuille flow. The velocity at midpoint $v_x(0)$ is maximum and the velocities at the walls $v_x(\pm s_z/2) = 0$. Note that by rewriting Eq. 2.48 as

$$v_x(z) = -\frac{\delta^2}{\eta}\frac{\partial P}{\partial x}\frac{1}{\cosh(s_z/2\delta)}[\cosh(s_z/2\delta) - \cosh(z/\delta)], \tag{2.50}$$

and expanding as Taylor series up to second order

$$v_x(z) \simeq -\frac{\delta^2}{\eta}\frac{\partial P}{\partial x}\underbrace{\frac{1}{\cosh(s_z/2\delta)}}_{\approx 1}\left[1 + \frac{1}{2!}\frac{s_z^2}{4\delta^2} - 1 - \frac{1}{2!}\frac{z^2}{\delta^2} + \mathcal{O}(\frac{z^4}{\delta^4})\right]. \tag{2.51}$$

Eq. 2.51 can be easily transformed into Eq. 2.49 for $\delta \gg s_z$. Throughout this work we only consider Poiseuille flow. Hence, we restrain ourselves to Eq. 2.49. Notice, Eq. 2.49 can also be obtained directly from the Navier-Stokes equation within the weak-flow limit.

Here we are interested in the flow of nematic liquid crystals. For this fluid a homogeneous density $\bar{\rho}$ throughout the system can be assumed. Hence, Eq. 2.49 can be rewritten in terms of the pressure gradient force $F_e = \frac{-1}{\bar{\rho}}\frac{\partial P}{\partial x}$ as [101]

$$v_x(z) = -\frac{\bar{\rho}F_e}{2\eta}\left[z^2 - \frac{s_z^2}{4}\right], \tag{2.52}$$

where $F_e$ is the external driving force acting on the system. With a second-order symmetric polynomial fit $v_x(z) = c_2 z^2 + c_0$ the effective viscosity can be computed from

$$\eta = -\frac{\bar{\rho} F_e}{2c_2}, \tag{2.53}$$

where $c_2$ can be obtained from fits to the velocity profiles [see Fig. 16 in Sec. 5.2]. The effective viscosity $\eta$, as well as the elastic constant $K$ [see Sec. 1.8] are fundamental to construct important dimensionless measures of flow.

## 2.5 Dimensionless measures of flow

In this Section we introduce common dimensionless quantities used throughout fluid dynamics. Dimensionless quantities are particularly useful in order to compare different systems with each other. If two systems share the same description through a dimensionless quantity they can be considered equivalent. We introduce the Reynolds number which is widely used in fluid dynamics. Additionally, we discuss another common quantity in fluid dynamics, the Euler number. Last, we consider the Ericksen number which is more prevalent in the field of liquid crystals under flow.

Introduced by Stokes [102] and established by Reynolds [103] the Reynolds number measures the ratio of inertial forces to viscous forces

$$\mathcal{R} = \frac{\bar{\rho} v_\infty l}{\eta}, \tag{2.54}$$

where $v_\infty$ is the streaming velocity at steady state and $l$ is the characteristic length of the system. Some ambiguity exists as far as $l$ is concerned. Throughout this work we take $l = s_z$, that is the distance between the substrates is the characteristic length scale of the system. Here we are interested in a colloidal particle dispersed in a nematic liquid crystal [see Sec. 3.4]. In general, one distinguishes between a particle-based and a flow-based Reynolds number. The former takes $l$ as the radius of the colloid whereas the latter uses $l$ as the distance between the substrates. The use throughout the literature is rather inconsistent. However, we adopt the flow-based definition which is consisted with the definition used in recent microfluidic experiments [54].

The Reynolds number characterizes different flow regimes. When inertial forces are dominating the flowing fluid is subject to instabilities such as vortices. This regime is referred to as turbulent flow and exhibits high Reynolds numbers $\mathcal{R}$. The laminar flow regime corresponding to low $\mathcal{R}$ is characterized by a smooth and constant flowing fluid. A laminar flow is dominated by viscous forces. However, if the fluid exhibits very low flow velocities and has a high viscosity the regime is referred to as creeping flow or Stokes flow. For Stokes flow the Reynolds number $\mathcal{R} \ll 1$. Liquid crystals, especially the nematic

phase, are characterized by a high viscosity. Hence, the flows considered in this work correspond to the laminar or even the Stokes flow regime.

In microfluidic experiments as well as in simulations another useful dimensionless number is the so-called Euler number [104]

$$\mathcal{C}_{\mathrm{E}} = \frac{\Delta P}{\bar{\rho} v_{\infty}^2}, \tag{2.55}$$

where $\Delta P$ is the pressure difference between the beginning and the end of the system. The Euler number measures the ratio of force due to a local pressure gradient and the kinetic energy per volume. The measured local pressure drop can be due to a restriction in the simulation cell like a colloid or cylindrical pillar in this work. Therefore, the Euler number measures the loss due to friction of the flow. For a perfect frictionless flow $\mathcal{C}_E = 1$. Notice, that the Euler number is independent of the viscosity. Therefore, it is useful to directly compare fluids with different viscosities. Additionally, the Euler number is closely related to the cavitation number, which utilizes instead the difference between the pressure within the simulation cell and the vapor pressure as $\Delta P$. Thus, the Euler number can characterize cavitating systems if the vapor pressure is not easily accessible.

Alignment effects due to flow [see Sec. 2.1] are in competition with alignment effects from other sources, such as external fields or chemically prepared substrates [see Sec. 3.3]. This leads to a distortion of the director field if different alignments scenarios are imposed. The Ericksen number is a useful measure of the deformation of the director field under flow. We define the Ericksen number [105] as

$$\mathcal{E} = \frac{\eta v_{\infty} l}{K}. \tag{2.56}$$

In the momentum balance of the Navier-Stokes equation $\mathcal{E}$ measures the ratio of viscous forces ($\eta v_{\infty}/l^2$) to elastic forces ($K/l^3$). Thus, the deformation of the director field can be either dominated by elastic forces ($\mathcal{E} \ll 1$) or viscous forces ($\mathcal{E} \gg 1$). In other words, for small $\mathcal{E}$ the director field is not affected by the flow, whereas for large $\mathcal{E}$ the flow determines the shape of the director field. Throughout this work we are mainly interested in systems exhibiting high Ericksen numbers $\mathcal{E}$. It is evident from Eqs. 2.54 and 2.56 that the Reynolds number and Ericksen number a related via

$$\mathcal{R} = \frac{\bar{\rho} K}{\eta^2} \mathcal{E}. \tag{2.57}$$

For liquid crystals one typically finds $\mathcal{R} \approx 10^{-4}\mathcal{E}$ [52].

## 2.6 Colloidal particles

The term "colloid" from the Greek "kollan" for glue, a protein rich colloidal dispersion, was first used by Graham in 1861 [106]. Colloids play an central role in many natural phenomena, such as shear thickening [107] and Brownian motion [108]. Thus, colloidal dispersions have been the subject of research early on without considering them explicitly in the framework of "colloidal science". Ostwald established the term and along with Buzagh and Hauser was one of the driving forces establishing colloidal science as an independent research field [109, 110].

Generally speaking a colloidal dispersion is a phase that is microscopically dispersed in a host phase. Particle sizes of colloidal dispersions can range from several nanometers up to microns. Hence, many colloidal dispersions can be visualized by a simple optical microscope. Therefore, colloidal science experienced its renaissance with the development and availability of optical microscopes. Even today, in many cases research on colloidal dispersions does not necessarily require advanced and expensive setups. However, at smaller length scales more sophisticated microscopy techniques are required and often they have to be used simultaneously in order to guarantee reliable results [111]. Therefore, molecular computer simulations operating at this length scale are an important and inexpensive tool for researchers.

Colloidal dispersions are indispensable in our everyday life. We encounter them on numerous occasions. They are present in many products, such as food, or in biological systems, like in our body in the shape of blood. Colloidal dispersions can be distinguished according to their host phase, which can be gaseous, liquid or solid. But also the colloidal particle itself can differ in terms of its state of aggregation. In general, one differentiates between foams, where gas bubbles are dispersed in a liquid host phase, emulsions, containing liquid droplets in a liquid host phase, and sols, with solid particles dispersed in the liquid host phase. Common examples are shaving cream (foam), milk (emulsion) and blood (sol). Thus, the research field of colloidal dispersions is very broad and diverse. Here, we are going to focus on a nematic liquid crystal as a host phase.

## 2.7 Physics and chemistry of colloidal particles

Colloids dispersed in a nematic liquid-crystal carrier fluid show a variety of periodic self-assembled structures. These structures can be highly symmetric, like linear chains of colloids [45]. This leads to novel photonic band-gap devices [112]. It is therefore important to study the properties of such a dispersion not only experimentally but also from a theoretical point of view. As explained in Sec. 1.3 a nematic liquid crystal is characterized by an orientational order along the director $\hat{\boldsymbol{n}}_0$. As one can imagine a dispersed colloidal particle affects the director field drastically. The colloid distorts the nematic order leading

to long-range anisotropic forces. This is caused by the alignment of the liquid-crystal molecules on the curved surface of the colloid. More specifically, this leads to a deviation between the far-field director $\hat{\boldsymbol{n}}_0$ and the director field $\hat{\boldsymbol{n}}(\boldsymbol{r})$ close to the colloidal surface. Hence, interesting topological defects around the colloid arise.

Furthermore, the presence of a colloidal particle increases the elastic free energy of the liquid-crystal host phase because of the perturbation of the director field $\hat{\boldsymbol{n}}(\boldsymbol{r})$. However, dispersing multiple colloids in a nematic liquid crystal can lead to interesting behavior. The elastic distortion of the nematic host induces long-ranged interactions between colloids. Therefore, colloids align for example as chains [45] in order to minimize the elastic free energy of the nematic liquid crystal. The possibility of a liquid-crystal host phase to arrange dispersed colloids into regular geometric patterns has also been applied to arrange defect structures into an array [113].

## 2.8 Defect structures near a homogeneous colloid

Figure 8 shows a two-dimensional representation of the most common defect topologies arising around a homogeneous colloidal particle dispersed in a nematic liquid crystal. One can imagine the director field depends crucially on how in particular the elongated linear liquid-crystal molecules align with the surface of the colloid. This leads to different defect topologies. The two extreme cases would be either that all molecules align planar or perpendicular with respect to the colloid's surface. Here we refer to these two cases as planar or perpendicular anchoring, respectively. Anchoring refers to an energetic discrimination of one or more orientations of the molecule at the surface of the colloid and will be explained in more detail in Sec. 3.4.

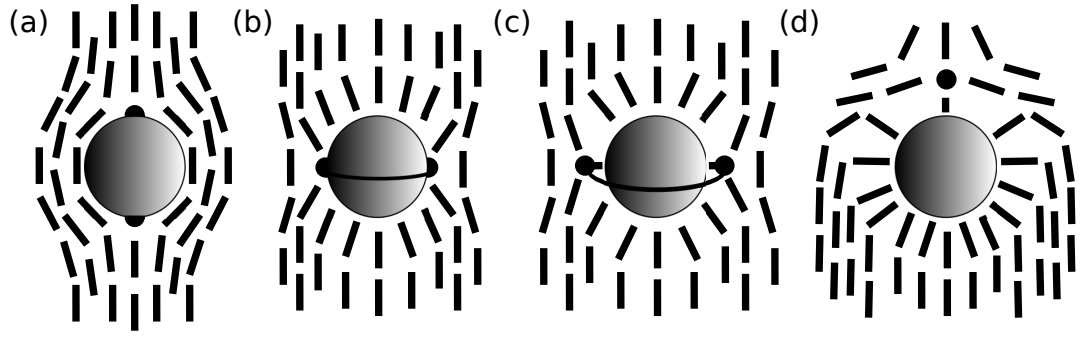


Figure 8: Graphical two-dimensional representation of different types of defect topologies that arise around a homogeneous colloid in a nematic liquid crystal: (a) Boojum defect, (b) Saturn ring for weak anchoring, (c) Saturn ring for strong anchoring and (d) hedgehog defect. Dashes represent the local director $\hat{\boldsymbol{n}}(\boldsymbol{r})$ and the defect topologies are represented by black dots (point defects) and black lines (disclinations).

For a homogeneous colloid exhibiting planar anchoring the director field is only distorted on the north and south pole of the colloid with respect to the director $\hat{\boldsymbol{n}}_0$. This is referred to as the Boojum defect topology [see Fig. 8 (a)]. A homogeneous colloid with perpendicular anchoring distorts the director field near the equator of the colloid. This leads to the Saturn ring defect located around the equator of the colloid [see Fig. 8 (b) and (c)]. However, the exact location of the ring defect depends on the anchoring strength. For stronger anchoring the director field is perturbed in a much larger area. Hence, the competition between anchoring and director field arises further away from the colloidal particle. Therefore, stronger anchoring leads to a Saturn ring defect slightly away from the colloidal surface [see Fig. 8 (c)]. For weaker anchoring the Saturn ring defect emerges very close the surface of the colloid [see Fig. 8 (b)].

Figure 8 (d) shows the so-called hedgehog defect. This type of defect is commonly observed in experimental studies for a homogeneous colloid with perpendicular anchoring. However, the hedgehog defect topology is only energetically favored for larger colloidal particles [25]. Therefore, in computer simulations, operating at the nanometer scale, it is rather difficult to obtain this defect topology. So far, a hedgehog defect has been observed in a computer simulation solely with *ad hoc* initial conditions [114]. Thus, this observed hedgehog defect very likely corresponds to a metastable state of the system.

## 2.9 Janus colloids

A colloidal particle can also be heterogeneous in size, shape or chemical functionality. One can imagine a large variety of these anisotropic particles. Here we are going to focus on surface-heterogeneous particles exhibiting multiple surface functionalities. However, often they possess an isotropic core. These particles are commonly referred to as patchy particles [115]. They can exhibit multiple patches of different size and shape. Patches can differ in electrical, chemical and/or physical properties. The most simple case would be a colloidal particle consisting of only two different patches. In 1988 Casagrande and Veyssié [116] synthesized particles with a hydrophilic and a hydrophobic patch. They were named Janus colloids after the Roman god of beginnings and transitions. This is due to the fact that their spherical symmetry is broken and the colloid is divided into two hemispheres. Both patches are of chemically different nature and therefore their physical properties are different as well. For example the patches can exhibit different magnetic properties leading to interesting self-assembled structures [117]. Here we consider patches with different anchoring of the liquid-crystal molecules. More specifically, one patch enforces perpendicular anchoring whereas the other one constrains molecules to anchor planar with respect to the surface of the colloid.

Nowadays, Janus colloids of different size and patchiness are accessible with sophisticated synthesis methods. It is even possible to manufacture Janus colloids on the

nanometer length-scale with an interface width of just a few nanometers between the different patches [118]. This is comparable to the length scale accessible to computer simulations. Experimental as well as theoretical studies of a Janus colloid dispersed in a nematic liquid crystal have led to a variety of new defect topologies [67, 68].

## 2.10 Defect structures near a Janus colloid

A Janus colloid with the equator perpendicular to the director field can create quite interesting defect topologies. Specifically, we consider the case where the upper hemisphere exhibits planar anchoring whereas the lower hemisphere is dominated by perpendicular anchoring. Figure 9 shows a two-dimensional representation of common defect structures for this configuration. The defect topologies arising around a Janus colloid dispersed in a nematic liquid crystal strongly depend on the ratio between the two different patches and thermodynamic variables such as temperature. One possible defect topology is a Boojum ring, where the perturbation of the director field is largest on the upper hemisphere [see Fig. 9 (a)]. Upon lowering the temperature the so-called crown topology arises [see Fig. 9 (b)]. Here the Boojum defect widens to a ring looking like a crown. For both defect topologies a second defect structure comparable to the surface ring is visible around the equator of the colloid. Figure 9 (c) shows the so-called cap configuration. This defect topology is observed for stronger planar anchoring on the upper hemisphere and a patch ratio in favor of the lower hemisphere with perpendicular anchoring. The point defect on the upper hemisphere coincides with the Saturn ring defect around the equator creating a cap shaped defect topology. When lowering the temperature the defect changes to an off-center Saturn ring [see Fig. 9 (d)]. The off-center position is due to the fact that the surface area of the upper hemisphere is much smaller than the one of the lower hemisphere [68].

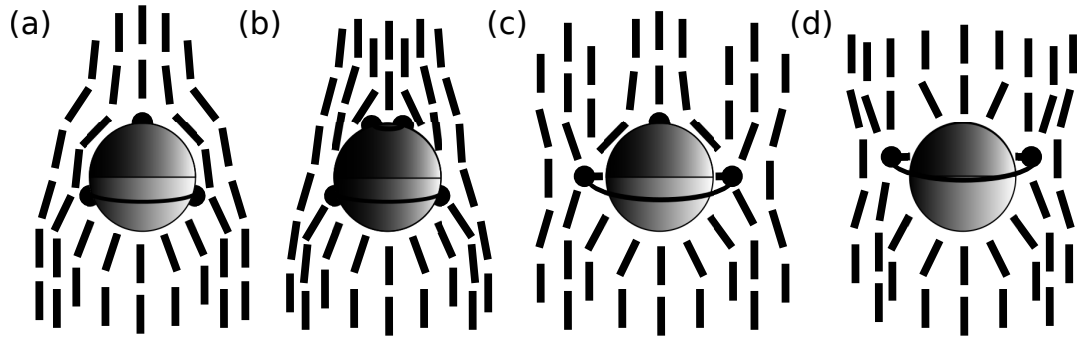


Figure 9: Graphical two dimensional representation of different types of defect topologies that arise around a Janus colloid in a nematic liquid crystal: (a) Boojum ring, (b) crown configuration, (c) cap configuration and (d) off-center Saturn ring. Dashes represent the local director $\hat{\boldsymbol{n}}(\boldsymbol{r})$ and the defect topologies are represented by black dots (point defects) and black lines (disclinations).

# 3 Model

## 3.1 Potential models

Our model system consists of a liquid crystal composed of $N$ molecules. The system is confined by two atomically resolved substrates at which the liquid-crystal molecules are anchored in a specific way. This ensures that the far-field nematic director $\hat{\boldsymbol{n}}_0$ remains fixed along a desired direction during the course of a simulation. The remaining two directions are subject to the usual periodic boundary conditions. Thus, the system is treated like it is surrounded by an infinite periodic lattice of identical systems. As molecules move in the original system during the simulation, their periodic images move exactly the same way. When molecules leave the original simulation box from one side one of their images will enter the box through the opposite site. Additionally, the so-called minimum image convention has to be applied to avoid that molecules interact with its own periodic image [119].

This setup can be seen as a microfluidic channel similar to those used in experimental studies, where the width of the channel is much larger than its depth [54]. Here we are interested in two different, yet closely related systems. Firstly, we study a system where a colloidal particle is dispersed in the nematic liquid crystal. Secondly, we are interested in a system where a cylindrical pillar connects the two substrates. For both systems the immersed object is fixed in space and treated via a soft potential including an excluded volume. Thus the total configurational potential energy of our system can be split into three contributions according to

$$\Phi = \Phi_{\mathrm{ff}} + \Phi_{\mathrm{fs}} + \Phi_{\mathrm{fc}}, \tag{3.58}$$

where the indices refer to the fluid-fluid (ff) interactions of the liquid-crystal molecules, the interaction between the fluid and the substrate (fs) and the fluid-colloid or fluid-cylinder interactions (fc). These different energetic contributions will be discussed in the following Sections.

## 3.2 Liquid crystal

To mimic the interaction between the liquid-crystal molecule we employ a potential model first introduced by Hess and Su [120]. Its simplicity makes it well suited for computer simulations and it has been successfully used to study and characterize liquid-crystal phases [121–126]. In contrast, the well established Gay-Berne potential [127] is computational rather expensive because of the elongated shape of the molecules. For the Hess-Su model the anisotropy of the molecules stems from the interaction rather then its elongated shape

[see Fig. 10]. Assuming pairwise additive interactions in the liquid-crystal fluid

$$\Phi_{\mathrm{ff}} = \sum_{i=1}^{N-1} \sum_{j>i}^{N} \varphi_{\mathrm{ff}} \left( \boldsymbol{r}_{ij}, \hat{\boldsymbol{u}}_i, \hat{\boldsymbol{u}}_j \right), \tag{3.59}$$

where the distance vector $\boldsymbol{r}_{ij} = \boldsymbol{r}_i - \boldsymbol{r}_j$ between the centers of mass of molecules $i$ and $j$ located at $\boldsymbol{r}_i$ and $\boldsymbol{r}_j$, respectively. The interaction potential $\varphi_{\mathrm{ff}}$ is split into an isotropic and an anisotropic contribution according to

$$\varphi_{\mathrm{ff}} \left( \boldsymbol{r}_{ij}, \hat{\boldsymbol{u}}_i, \hat{\boldsymbol{u}}_j \right) = \varphi_{\mathrm{iso}} \left( r_{ij} \right) + \varphi_{\mathrm{anis}} \left( \boldsymbol{r}_{ij}, \hat{\boldsymbol{u}}_i, \hat{\boldsymbol{u}}_j \right). \tag{3.60}$$

In Eqs. (3.59) and (3.60) $r_{ij} = |\boldsymbol{r}_{ij}|$, $\hat{\boldsymbol{u}}_i$ and $\hat{\boldsymbol{u}}_j$ are versors (unit vectors) specifying the orientations of molecules $i$ and $j$ in a space-fixed frame of reference. We take the isotropic part of the fluid-fluid interaction potential to be given by the Lennard-Jones potential function

$$\varphi_{\mathrm{iso}} \left( r_{ij} \right) = 4\varepsilon \left[ \left( \frac{\sigma}{r_{ij}} \right)^{12} - \left( \frac{\sigma}{r_{ij}} \right)^{6} \right], \tag{3.61}$$

where $\varepsilon$ is the depth of the attractive well and $\sigma$ is the van der Waals radius of a spherical reference molecule. To derive an expression for the anisotropic contribution we follow Giura and Schoen [128]. We write

$$\varphi_{\mathrm{anis}} \left( \boldsymbol{r}_{ij}, \hat{\boldsymbol{u}}_i, \hat{\boldsymbol{u}}_j \right) = -4\varepsilon \left( \frac{\sigma}{r_{ij}} \right)^{6} \Psi \left( \hat{\boldsymbol{r}}_{ij}, \hat{\boldsymbol{u}}_i, \hat{\boldsymbol{u}}_j \right), \tag{3.62}$$

where the anisotropy function is given by

$$\Psi \left( \hat{\boldsymbol{r}}_{ij}, \hat{\boldsymbol{u}}_i, \hat{\boldsymbol{u}}_j \right) = 5\varepsilon_1 P_2 \left( \hat{\boldsymbol{u}}_i \cdot \hat{\boldsymbol{u}}_j \right) + 5\varepsilon_2 \left[ P_2(\hat{\boldsymbol{u}}_i \cdot \hat{\boldsymbol{r}}_{ij}) + P_2(\hat{\boldsymbol{u}}_j \cdot \hat{\boldsymbol{r}}_{ij}) \right], \tag{3.63}$$

and $P_2 \left( x \right) \equiv \frac{1}{2} \left( 3x^2 - 1 \right)$ is the second Legendre polynomial, $\hat{\boldsymbol{r}}_{ij} = \boldsymbol{r}_{ij}/r_{ij}$, and $\varepsilon_1$ and $\varepsilon_2$ are (dimensionless) anisotropy parameters. We take $2\varepsilon_1 = -\varepsilon_2 = 0.08$ throughout this work. The molecules can be described as ellipsoids of revolution with an aspect ratio of 1.26 [see Fig. 10].

The first summand on the right side of Eq. 3.63 corresponds to the well-known Maier-Saupe term [23]; the other two are corrections describing the orientational dependence of $\varphi_{\mathrm{anis}}$ with increased sophistication. Thus, neglecting the corrections one ends up with the well known Maier-Saupe model [129]. As discussed by Giura and Schoen [128] the specific form of the anisotropy function $\Psi$ is obtained by expanding the anisotropic dispersion attractions in the basis of rotational invariants. The authors assumed solely dispersion interactions, invariance of $\varphi_{\mathrm{anis}}$ upon interchanging molecules $i$ and $j$, and head-tail symmetry of the molecules, that is $\hat{\boldsymbol{u}}_i = -\hat{\boldsymbol{u}}_i$. With the aid of these symmetry considerations it is relatively straightforward, but rather long, to derive Eq. 3.63 if one keeps only the

four leading terms in the expansion.

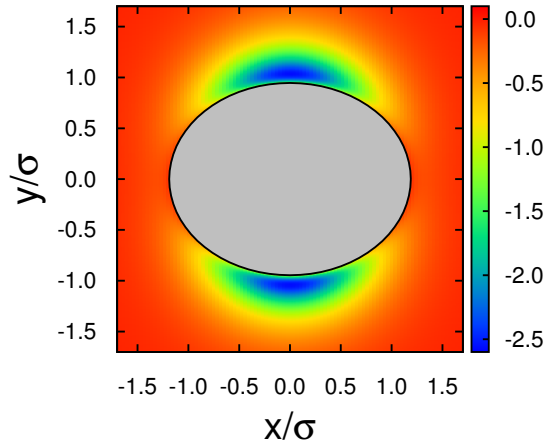


Figure 10: Equipotential energy contour plot for the Hess-Su potential. The plot is generated by moving a molecule, with a fixed orientation, in the $x$-$y$-plane around another molecule which is fixed in space and orientation.

## 3.3 Atomically resolved substrate

The potential model described in the previous section is capable of forming a nematic phase for a suitably chosen thermodynamic state. In the bulk, the far field nematic director $\hat{\boldsymbol{n}}_0$ can point in any direction. Additionally, during the course of a simulation the direction of $\hat{\boldsymbol{n}}_0$ is subject to change. Hence, it is impossible to predict the direction of $\hat{\boldsymbol{n}}_0$ beforehand. Obviously, this situation is not desirable both experimentally and theoretically where one would like to control $\hat{\boldsymbol{n}}_0$. Furthermore, the flow of nematic liquid crystals is coupled to the director orientation [see Sec. 2.1]. Therefore, fixing the alignment of the molecules simplifies the task for most problems. One possible route to achieve control over $\hat{\boldsymbol{n}}_0$ is the use of specially prepared solid substrates. More specifically, liquid-crystal molecules anchor in the desired way on the substrates imposing a preferred direction on $\hat{\boldsymbol{n}}_0$. Experimentally, this can be achieved either by mechanical means (e.g., rubbing or polishing), deposition of chemical substances on the pristine substrate, or external fields such as, for example, UV [130] or laser light [131] or by exposing the liquid crystal to flow [132].

A planar smooth substrate is perfectly capable of of controlling the global director $\hat{\boldsymbol{n}}_0$ and has been used throughout the literature. However, here we are interested in nonequilibrium molecular dynamics simulations of liquid crystals. We apply a Poiseuille flow [see Sec. 2.4] to drive the system out of equilibrium. In order to achieve this one needs structured surfaces, such as atomically resolved substrates, to create the necessary friction close to a substrate. However, atomically resolved substrates are not only needed to create a parabolic Poiseuille flow. To obtain a steady state during the course of a

simulation a certain amount of friction is needed to balance the force driving the system is needed as well. Reaching a steady state is crucial for obtaining reasonable time averages of the physical quantities of interest.

In our model we express the fluid-substrate interaction as

$$\Phi_{\mathrm{fs}} = \sum_{i=1}^{N} \sum_{j=1}^{2N'} \varphi_{\mathrm{fs}}(r'_{ij}, \hat{\boldsymbol{u}}_i), \tag{3.64}$$

assuming that each solid substrate consists of a monolayer of $N'$ atoms. The substrate atoms are located at positions $\boldsymbol{S} = \{\boldsymbol{s}_1, \boldsymbol{s}_2, \ldots, \boldsymbol{s}_{2N'}\}$, $r'_{ij} = \mid \boldsymbol{r}_i - \boldsymbol{s}_j \mid$, and

$$\varphi_{\mathrm{fs}}(r'_{ij}, \hat{\boldsymbol{u}}_i) = 4\varepsilon \left[ \left( \frac{\sigma}{r'_{ij}} \right)^{12} - \left( \frac{\sigma}{r'_{ij}} \right)^{6} g_s(\hat{\boldsymbol{u}}_i) \right]. \tag{3.65}$$

The atoms in each substrate form a monolayer in registry with each other using the (100) face of a face-centered cubic (fcc) lattice. The fcc (100) structure is characterized by a lattice constant $L/\sigma = \sqrt[3]{4}$ such that the areal density of the solid monolayers corresponds to $\rho_s = 2/L^2$. In Eq. 3.65, $0 \leq g_s(\hat{\boldsymbol{u}}_i) \leq 1$ is the so-called anchoring function, a mathematical device mimicking the specially prepared substrates from experimental systems. More specifically, $g_s(\hat{\boldsymbol{u}}_i)$ distinguishes energetically between desirable and undesirable orientations of a molecule relative to the substrate plane. In this work we consider planar anchoring along the $x$-axis and homeotropic anchoring along the $z$-axis. First, if

$$g_s(\hat{\boldsymbol{u}}_i) = g_x(\hat{\boldsymbol{u}}_i) = [\hat{\boldsymbol{u}}_i \cdot \hat{\boldsymbol{e}}_x]^2, \tag{3.66}$$

where $\hat{\boldsymbol{e}}_x$ is the unit vector (versor) of the $x$-axis, one realizes that the attractive interaction between a molecule and a substrate atom is switched off if $\hat{\boldsymbol{u}}_i \perp \hat{\boldsymbol{e}}_x$ whereas it is fully switched on if $\hat{\boldsymbol{u}}_i \parallel \hat{\boldsymbol{e}}_x$. Hence, alignment of the molecules along the $x$-axis is favored. Second, to realize alignment of the molecules along the $z$-axis we take

$$g_s(\hat{\boldsymbol{u}}_i) = g_z(\hat{\boldsymbol{u}}_i) = [\hat{\boldsymbol{u}}_i \cdot \hat{\boldsymbol{e}}_z]^2, \tag{3.67}$$

where $\hat{\boldsymbol{e}}_z$ is the unit vector (versor) of the $z$-axis, leading to homeotropic anchoring.

## 3.4 Colloidal particle

A great part of this work considers a system where a spherical colloid is immersed in the host phase and placed at the center of the simulation cell, halfway between both solid substrates. Its position coincides with the origin of a space-fixed Cartesian coordinate system. Experimentally, one could use optical tweezers to fix the colloid in space even

though the host phase will eventually flow past it [44, 133]. The distance between both substrates is chosen wide enough so that only the fluid-colloid interactions have to be accounted for. Hence,

$$\Phi_{\mathrm{fc}} = \sum_{i=1}^{N} \varphi_{\mathrm{fc}}(\boldsymbol{r}_i, \hat{\boldsymbol{u}}_i; r_0), \tag{3.68}$$

where $r_0$ is the hard-core radius of the colloidal particle. The fluid-colloid interaction is expressed via an attractive Yukawa-like potential function and an inverse power law repulsion

$$\varphi_{\mathrm{fc}}(\boldsymbol{r}_i, \hat{\boldsymbol{u}}_i; r_0) = \varepsilon \left[ a_1 \left( \frac{\sigma}{r_i - r_0} \right)^{10} - a_2 \frac{\exp[-\lambda(r_i - r_0)]}{r_i - r_0} g_c(\hat{\boldsymbol{r}}_i, \hat{\boldsymbol{u}}_i) \right], \tag{3.69}$$

where $r_i = |\boldsymbol{r}_i|$ and $\hat{\boldsymbol{r}}_i = \boldsymbol{r}_i / r_i$. Because the colloid is fixed at the origin the term $r_i - r_0$ represents the distance of a molecule $i$ from the colloidal surface. In Eq. 3.69 $\lambda$ represents the inverse Debye screening length of the attractive fluid-colloid interactions. The dimensionless parameters

$$a_1 = \frac{1 + \lambda\sigma}{9 - \lambda\sigma}, \tag{3.70}$$

$$a_2 = \frac{10 \exp(\lambda\sigma)}{9 - \lambda\sigma} \tag{3.71}$$

have been introduced such that the depth of the attractive well remains constant at $\varepsilon$ and stays at a distance $r_0 + \sigma$ from the center of the colloid irrespective of the value of $\lambda$ [see Fig. 11]. However, some caution is advisable in choosing the value of $\lambda$. For one, it is evident from Eqs. 3.70 and 3.71 that $\lambda\sigma < 9$. In practice, it turns out that for $\lambda\sigma \gtrsim 7$ the potential function $\varphi_{fc}$ develops a repulsive tail located at $r_i - r_0 > \sigma$. Additionally, for $\lambda = 0$ the attractive tail corresponds to a Coulomb potential between unlike charges. Hence, fluid-colloid interactions are very long ranged and one would have to apply Ewald summation techniques to account for the interaction properly [119].

Molecules in the immediate vicinity of the colloid are also subject to a variety of anchoring scenarios, again realized with an anchoring function $g_c(\hat{\boldsymbol{r}}_i, \hat{\boldsymbol{u}}_i)$ [see Eq. 3.69]. First, we will consider colloids with a chemically homogeneous surface [see Sec. 2.7]. Here we study three different kinds of anchoring: (*i*) nonspecific, $g_c(\hat{\boldsymbol{r}}_i, \hat{\boldsymbol{u}}_i) = 1$, (*ii*) planar, that is, molecules are preferably planar to the colloids surface

$$g_c(\hat{\boldsymbol{r}}_i, \hat{\boldsymbol{u}}_i) = g_{\parallel}(\hat{\boldsymbol{r}}_i, \hat{\boldsymbol{u}}_i) = [1 - |\hat{\boldsymbol{u}}_i \cdot \hat{\boldsymbol{r}}_i|]^2, \tag{3.72}$$

and (*iii*) perpendicular anchoring, where molecules anchor perpendicularly with respect to the colloidal surface

$$g_c(\hat{\boldsymbol{r}}_i, \hat{\boldsymbol{u}}_i) = g_{\perp}(\hat{\boldsymbol{r}}_i, \hat{\boldsymbol{u}}_i) = [\hat{\boldsymbol{u}}_i \cdot \hat{\boldsymbol{r}}_i]^2. \tag{3.73}$$

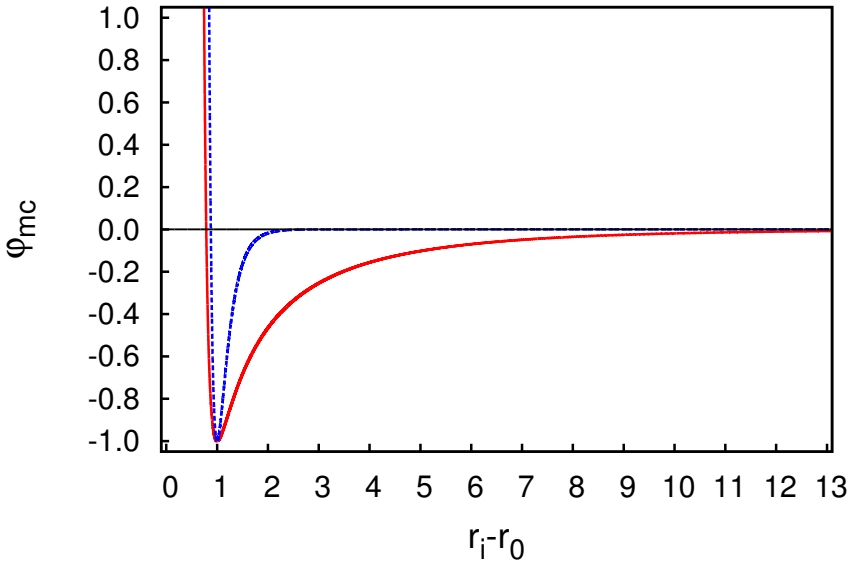


Figure 11: Plot of the fluid-colloid interaction potential $\varphi_{\mathrm{fc}}$ (in units of $\varepsilon$) as a function of a molecule's distance $r$ (in units of $\sigma$) from the center of the colloidal particle located at the origin of the coordinate system. For both plots $r_0 = 3\sigma$ and $\lambda\sigma = 0.20$ (——) and $\lambda\sigma = 4.00$ (- - -). Both plots have been generated for $g_c(\hat{\boldsymbol{r}}_i, \hat{\boldsymbol{u}}_i) = 1.00$ [see Eq. (3.69)]. For this special choice of $g_c$ depends only on $r_i - r_0$.

For nonspecific anchoring a molecule is not energetically penalized for any given orientation, whereas for homeotropic and planar anchoring molecules receive an energy penalty if they are oriented differently than the desired anchoring.

Second, a Janus colloid [see Sec. 2.9] can be modeled in a very similar fashion. We introduce two different patches that anchor molecules either planar or perpendicularly to the surface. In order to achieve this we modify the anchoring function in Eq. 3.69 such as

$$g_c(\hat{\boldsymbol{r}}_i, \hat{\boldsymbol{u}}_i) = \omega_{\parallel} g_{\parallel}(\hat{\boldsymbol{r}}_i, \hat{\boldsymbol{u}}_i) + \alpha\omega_{\perp} g_{\perp}(\hat{\boldsymbol{r}}_i, \hat{\boldsymbol{u}}_i), \tag{3.74}$$

where the same functions for planar and perpendicular anchoring are used as in Eqs. 3.72 and 3.73 and the dimensionless parameter $\alpha$ is introduced to weaken the perpendicular anchoring. This is due to the fact that perpendicular anchoring of linear molecules is energetically favored on surfaces even without a specified anchoring function. The anchoring function in Eq. 3.74 is weighted according to

$$\omega_{\parallel}(\hat{\boldsymbol{r}}_i) = 1 - \gamma_{\parallel}(1 - \hat{\boldsymbol{r}}_i \cdot \hat{\boldsymbol{e}}_x)^{\delta}, \tag{3.75}$$

$$\omega_{\perp}(\hat{\boldsymbol{r}}_i) = 1 - \gamma_{\perp}(1 + \hat{\boldsymbol{r}}_i \cdot \hat{\boldsymbol{e}}_x)^{2}, \tag{3.76}$$

where $\gamma_{\parallel} \leq 2^{-\delta}$ and $\gamma_{\perp} \leq 0.25$ in order to get a meaningful weighting function. Both parameters account for the smoothness of the transition between the patches and $\delta$ yields the ratio of the patch sizes. The unit vector $\hat{\boldsymbol{e}}_x$ is perpendicular to the plane of the equator of the colloid. Hence, $\hat{\boldsymbol{r}}_i \cdot \hat{\boldsymbol{e}}_x = +1(-1)$ defines the north (south) pole of the colloid. The weighting function $\omega_{\parallel}(\hat{\boldsymbol{r}}_i)$ is maximal at the north pole of the colloid, whereas $\omega_{\perp}(\hat{\boldsymbol{r}}_i)$ is opposite and has its largest value at the south pole of the colloid. Notice, that upon changing the sign of the unit vector $\hat{\boldsymbol{e}}_x$ one is able to switch the different patches. Figure 12 shows heat maps of the model potential used here to mimic a Janus colloid. It shows nicely that a different anchoring is energetically favored on each patch of the colloid. Hence, the potential is most attractive when the alignment of a molecule matches the preferred anchoring of the particular patch. For misalignment the potential energy between the colloid and the molecule is much weaker. Notice the rather smooth transition between patches ensuring numerical stability [68].

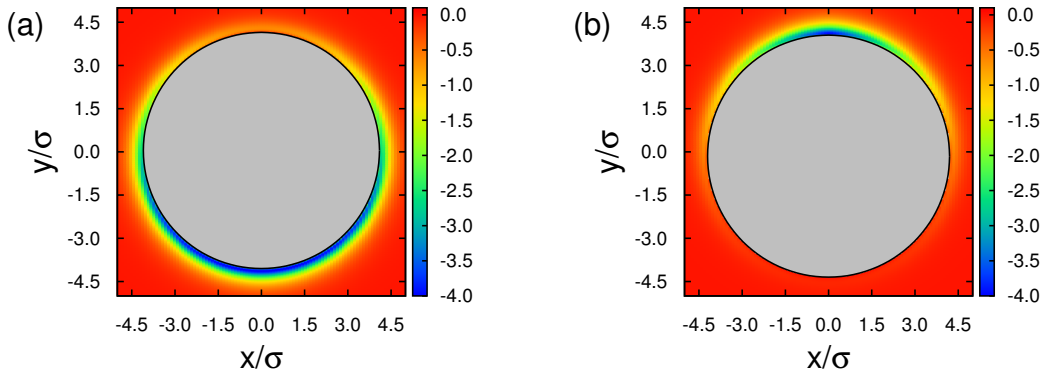


Figure 12: Equipotential energy contour plots for the fluid-colloid potential. Plots are generated by moving a molecule, with a fixed orientation, in the $x$-$y$-plane around the colloid which is fixed in space. The orientation was kept fixed (a) perpendicular and (b) planar with respect to the surface of the colloid.

## 3.5 Cylindrical pillar

We are also interested in a system containing a cylindrical pillar with a chemically homogeneous surface. The long axis of the cylinder is placed perpendicular to the solid substrates and the cylindrical pillar spans the entire distance between the two substrates along the $z$-axis. Experimentally, this can be compared to a setup where the cylindrical pillar is part of the cast prepared using soft lithography [2]. It is common practice in a computer simulation to place the cylindrical pillar, like the colloid in the previous section, at a fixed position at the center of the simulation box and apply periodic boundary conditions. We investigate a cavity with a growing volume upon increasing flow. The cavity is growing along the direction of flow, the $x$-axis [see Sec. 4.7]. Hence, the cylindrical pillar

is positioned slightly upstream of the midpoint of the simulation cell with respect to the $x$-axis. This assures that the cavity is not interfering with its nearest image. Additionally, smaller system sizes become accessible demanding less computational power.

Again, we neglect interactions between the cylinder and the substrate. Thus, Eq. 3.68 is still valid. However, the fluid-cylinder interactions are treated slightly differently. We adopt a modified Lennard-Jones potential function

$$\varphi_{\mathrm{fc}}(\boldsymbol{r}_i, \hat{\boldsymbol{u}}_i; r_0) = \varepsilon \left[ \left( \frac{\sigma}{r_i - r_0} \right)^{12} - \left( \frac{\sigma}{r_i - r_0} \right)^{6} g_c(\hat{\boldsymbol{r}}_i, \hat{\boldsymbol{u}}_i) \right]. \tag{3.77}$$

The term $r_i - r_0$ now represents the distance to the cylinder's surface. Notice that because of the cylindrical symmetry the fluid-cylinder distance can be simply calculated in the $x$-$y$-plane. Molecules close to the cylindrical surface exhibit a preferential anchoring due to the chemical nature of the cylindrical pillar. In Eq. 3.77 we use again the anchoring function $g_c(\hat{\boldsymbol{r}}_i, \hat{\boldsymbol{u}}_i)$ to control the alignment of the molecules with respect to the surface. In principle one can use the same expressions as for the homogeneous colloid [see Eqs. 3.72 and 3.73]. However, in this part of the work we restrict ourselves to the case of homeotropic anchoring represented by Eq. 3.73.

# 4 Computational details

## 4.1 Molecular dynamics simulation

In this chapter we will describe the techniques employed in our molecular dynamics simulations. The heart of every molecular dynamics simulation is solving the classical equations of motion for a system containing $N$ molecules interacting via a potential as in Eq. 3.59. The temporal evolution of molecules is described by Hamilton's equations [134]. For simple cases, such as classical molecular dynamics, Hamilton's equations simplify to Newton's second law of motion

$$\boldsymbol{F}_i = m_i \ddot{\boldsymbol{r}}_i, \tag{4.78}$$

where $\boldsymbol{F}_i$ is the force acting on molecule $i$ and $m_i$ its mass.

Along with the initial conditions, such as molecular positions and velocities, Eq. 4.78 can be solved numerically, with the aid of a computer, leading to a unique solution. Differential equations such as Eq. 4.78 can be solved by discretizing them in time $t$. To that end, we consider a Taylor expansion of the positions $\boldsymbol{r}_i$ of molecule $i$ at time $t + \delta t$ around $t$

$$\boldsymbol{r}_i(t + \delta t) = \boldsymbol{r}_i(t) + \delta t \boldsymbol{v}_i(t) + \frac{1}{2}\delta t^2 \boldsymbol{a}_i(t) + \mathcal{O}(\delta t^3), \tag{4.79}$$

where $\mathcal{O}(\delta t^3)$ stands for cubic or higher order terms in $\delta t$ [119].

A variety of numerical algorithms have been devised to solve this problem. One of the most efficient and widely used approaches is the velocity Verlet algorithm, which we will describe in full detail in the next section.

## 4.2 Velocity Verlet algorithm

The standard Verlet algorithm [135] is widely used to solve directly Newton's equation. The algorithm is based on the positions $\boldsymbol{r}_i(t)$, the accelerations $\boldsymbol{a}_i(t)$ and the positions $\boldsymbol{r}_i(t - \delta t)$ at the previous time step of molecule $i$ leading to

$$\boldsymbol{r}_i(t + \delta t) = 2\boldsymbol{r}_i(t) - \boldsymbol{r}_i(t - \delta t) + \delta t^2 \boldsymbol{a}_i(t). \tag{4.80}$$

This equation describes the advancing positions of each molecule. The velocities have been eliminated through the summation of the Taylor expansions for $\boldsymbol{r}_i(t + \delta t)$ and $\boldsymbol{r}_i(t - \delta t)$ about $\boldsymbol{r}_i(t)$

$$\begin{aligned} \boldsymbol{r}_i(t + \delta t) &= \boldsymbol{r}_i(t) + \delta t \boldsymbol{v}_i(t) + \frac{1}{2}\delta t^2 \boldsymbol{a}_i(t) + \mathcal{O}(\delta t^3), \\ \boldsymbol{r}_i(t - \delta t) &= \boldsymbol{r}_i(t) - \delta t \boldsymbol{v}_i(t) + \frac{1}{2}\delta t^2 \boldsymbol{a}_i(t) - \mathcal{O}(\delta t^3). \end{aligned} \tag{4.81}$$

Although velocities are not needed to calculate the trajectories, we might need them to calculate quantities such as the total energy, diffusion or viscosity of the system. The velocities can be obtained from the following equation

$$\boldsymbol{v}_i(t) = \frac{\boldsymbol{r}_i(t+\delta t) - \boldsymbol{r}_i(t-\delta t)}{2\delta t}. \tag{4.82}$$

The main problem with the standard Verlet algorithm is that the velocities can only be calculated once $\boldsymbol{r}_i(t+\delta t)$ is known. Therefore, positions, velocities and accelerations are not accessible at the same time $t$ which makes this algorithm difficult to implement in nonequilibrium molecular dynamics simulations. A modification of the Verlet algorithm that is capable of handling positions, velocities and accelerations at the same time $t$ is the so called *velocity Verlet* algorithm.

The velocity Verlet algorithm is symplectic, meaning that it corresponds to a canonical transformation of the equations of motion, and conserves phase space because of Liouville's theorem. The velocity Verlet algorithm takes the form

$$\boldsymbol{r}_i(t+\delta t) = \boldsymbol{r}_i(t) + \delta t \boldsymbol{v}_i(t) + \frac{1}{2}\delta t^2 \boldsymbol{a}_i(t), \tag{4.83}$$

$$\boldsymbol{v}_i(t+\delta t) = \boldsymbol{v}_i(t) + \frac{1}{2}\delta t[\boldsymbol{a}_i(t) + \boldsymbol{a}_i(t+\delta t)]. \tag{4.84}$$

The standard Verlet algorithm may be recovered by eliminating the velocities. The velocity Verlet algorithm evolves in two stages. First, the new positions at time $t+\delta t$ are calculated according to Eq. 4.83 and the velocities at mid-step are calculated via

$$\boldsymbol{v}_i(t+\frac{1}{2}\delta t) = \boldsymbol{v}_i(t) + \frac{1}{2}\delta t \boldsymbol{a}_i(t). \tag{4.85}$$

Second, the forces are computed at time $t+\delta t$ and the velocity move is completed

$$\boldsymbol{v}_i(t+\delta t) = \boldsymbol{v}_i(t+\frac{1}{2}\delta t) + \frac{1}{2}\delta \boldsymbol{a}_i(t+\delta t). \tag{4.86}$$

At this point kinetic and potential energy are available at $t+\delta t$ [119, 136].

## 4.3 Dynamics of linear molecules

Liquid crystals consist of non-spherical, anisometric molecules. Hence, it is important to consider the rotational dynamics in the molecular dynamics simulations. Here we discuss the formulation of the velocity Verlet algorithm proposed by Ilnystkyi and Wilson [137]. There exists variations [138] and other approaches, for example for polyatomic systems one could consider the widely used SHAKE algorithm [139].

It is a common approach to divide molecular motion into a translational and rota-

tional part. The translation of the molecules was covered by the previous section. The equation governing rotational dynamics is

$$\frac{\mathrm{d}\boldsymbol{L}_i}{\mathrm{d}t} = \boldsymbol{\tau}_i, \tag{4.87}$$

where $\boldsymbol{L}_i$ is the angular momentum of molecule $i$ and $\boldsymbol{\tau}_i$ is its torque given by

$$\boldsymbol{\tau}_i \equiv \boldsymbol{d} \times \boldsymbol{F}_i, \tag{4.88}$$

where $\boldsymbol{d}$ is the position vector relative to the center of rotation, namely the center of mass of a molecule. The torque can be thought of as a measure of the turning force acting on a molecule.

The equations of motion for the rotation of a molecule may be derived from Hamilton's equations

$$\dot{\hat{\boldsymbol{u}}}_i = \boldsymbol{\omega}_i \times \hat{\boldsymbol{u}}_i, \tag{4.89}$$

$$\dot{\boldsymbol{\omega}}_i = \frac{\boldsymbol{\tau}_i}{\mathcal{I}}, \tag{4.90}$$

where $\boldsymbol{\omega}_i$ is the angular velocity of molecule $i$ and $\mathcal{I}$ is the moment of inertia. For linear molecule $\boldsymbol{\tau}_i$ is always perpendicular to $\hat{\boldsymbol{u}}_i$, hence it is convenient to define a new vector $\boldsymbol{g}_i$ through the equation

$$\boldsymbol{\tau}_i = \hat{\boldsymbol{u}}_i \times \boldsymbol{g}_i = \hat{\boldsymbol{u}}_i \times \boldsymbol{g}_i^{\perp}, \tag{4.91}$$

where $\boldsymbol{g}_i \equiv -\nabla_{\hat{\boldsymbol{u}}_i} U$ is the so-called "gorque", and $\boldsymbol{g}_i^{\perp} = \boldsymbol{g}_i - (\boldsymbol{g}_i \cdot \hat{\boldsymbol{u}}_i)\hat{\boldsymbol{u}}_i$. Because the angular velocity must always be perpendicular to the molecular axis, $\boldsymbol{\omega}_i \cdot \hat{\boldsymbol{u}}_i = 0$, it is convenient to replace the angular velocity $\boldsymbol{\omega}_i$ with the orientational velocity $\boldsymbol{e}_i$. The equations of motion can be rewritten as two first-order differential equations

$$\dot{\hat{\boldsymbol{u}}}_i = \boldsymbol{e}_i, \tag{4.92}$$

$$\dot{\boldsymbol{e}}_i = \frac{\boldsymbol{g}_i^{\perp}}{\mathcal{I}} + \lambda_i \hat{\boldsymbol{u}}_i, \tag{4.93}$$

where $\lambda_i$ is a Lagrange multiplier. Equations 4.92 and 4.93 can be solved numerically with a velocity Verlet algorithm, introduced in the previous section. Again, the calculation evolves in two steps. First, the orientational velocities at mid-step are calculated via

$$\boldsymbol{e}_i(t + \frac{1}{2}\delta t) = \boldsymbol{e}_i(t) + \frac{1}{2}\delta t[\boldsymbol{g}_i^{\perp}(t) + \lambda_i' \hat{\boldsymbol{u}}_i(t)]. \tag{4.94}$$

Second, the orientations

$$\hat{\boldsymbol{u}}_i(t + \delta t) = \hat{\boldsymbol{u}}_i(t) + \delta t \boldsymbol{e}_i(t + \delta t) \tag{4.95}$$

are calculated at time $t + \delta t$, the gorque $\boldsymbol{g}_i^{\perp}(t + \delta t)$ is evaluated and the orientational

velocity move is completed

$$\boldsymbol{e}_i(t+\delta t) = \boldsymbol{e}_i(t+\frac{1}{2}\delta t) + \frac{1}{2}\delta t[\boldsymbol{g}_i^{\perp}(t+\delta t) - \lambda_i''\hat{\boldsymbol{u}}_i(t+\delta t)]. \tag{4.96}$$

The Lagrange multipliers $\lambda_i'$ and $\lambda_i''$ in Eqs. 4.94 and 4.96 are obtained solving the constraints $[\hat{\boldsymbol{u}}_i(t+\delta t)]^2 = 1$ and $[\boldsymbol{e}_i(t+\delta t)\cdot\boldsymbol{r}_i(t+\delta t)] = 0$, respectively [119, 137].

## 4.4 Global Nosé-Hoover thermostat

Solving Newton's equations leads to phase space trajectories corresponding to the microcanonical ensemble, where the number of molecules $N$, volume $V$ and energy $E$ are conserved. To perform simulations under constant temperature $T$ a thermostat must be implemented. There are several different methods to achieve constant $T$ in a molecular dynamics simulation. A very popular approach was first proposed by Nosé [140, 141]. Here the system is in contact with a thermal reservoir which is included through an additional degree of freedom $s$. Energy is allowed to flow back and forth from the system to the reservoir. The approach is based on an extended Lagrangian formalism, which contains additional, fictitious coordinates and velocities. The Lagrangian of the system is

$$\begin{aligned} \mathcal{L}_s &= \mathcal{K} + \mathcal{K}_s - \mathcal{V} - \mathcal{V}_s \\ &= \sum_{i=1}^{n} \frac{m_i}{2} s^2 \dot{\boldsymbol{r}}_i^2 + \frac{Q}{2}\dot{s}^2 - \mathcal{V} - (f+1)k_{\mathrm{B}}T\ln(s), \end{aligned} \tag{4.97}$$

where $\mathcal{K}$ and $\mathcal{V}$ denote kinetic and potential energy, $f$ is the number of degrees of freedom ($3N-3$ for fixed total momentum) and $Q$ is the thermal inertia parameter or an effective mass which controls the rate of temperature fluctuations. In other words, a friction force is added to the system to control the temperature.

The equations of motion follow as

$$\ddot{\boldsymbol{r}} = \frac{\boldsymbol{F}}{ms^2} - \frac{2\dot{s}\dot{\boldsymbol{r}}}{s}, \tag{4.98}$$

$$Q\ddot{s} = \sum_{i=1}^{N} m\dot{\boldsymbol{r}}_i^2 - \frac{(f+1)k_{\mathrm{B}}T}{s}. \tag{4.99}$$

The extended Hamiltonian $\mathcal{H}_s = \mathcal{K} + \mathcal{K}_s + \mathcal{V} + \mathcal{V}_k$ of the system is conserved. Hoover [142] has extended the formalism of Nosé. The equations of motion are slightly modified paying particular attention to controlling the temperature in a more subtle fashion.

$$\dot{\boldsymbol{r}} = \boldsymbol{p}/m, \tag{4.100}$$

$$\dot{\boldsymbol{p}} = \boldsymbol{F} - \xi\boldsymbol{p}, \tag{4.101}$$

where $\boldsymbol{p}$ is the linear momentum, and $\xi$ is the friction coefficient given by the first order differential equation

$$\dot{\xi} = \frac{f}{Q}(k_{\mathrm{B}}\mathcal{T} - k_{\mathrm{B}}T), \tag{4.102}$$

where $\mathcal{T}$ is the instantaneous value of the kinetic temperature. This method is widely referred to as the Nosé-Hoover thermostat. Calculations are performed in a microcanonical $NVE'$ ensemble with the modified Hamiltonian $\mathcal{H}_s$. However, the thermodynamic averages are equivalent to those in the canonical $NVT$ ensemble with the original Hamiltonian $\mathcal{H}$ for a rescaled particle momentum. This thermostat is of global nature, because the temperature is calculated by considering all particles in the system. Additionally, it is not Galilean invariant, because all calculations are performed in a reference frame where the system's center of mass is at rest. Therefore, this thermostat does not conserve local momentum [119, 136, 143].

## 4.5 Galilean-invariant thermostat

A global thermostat is not suitable when external forces are acting on the system which, for example, may set a macroscopic fluid flow into motion. One plausible approach would be a modification of the Nosé-Hoover thermostat to make it local and thus also conserve local momentum. There have been such modifications [144] and the simplest is to separate the system into slices and apply an isolated Nosé-Hoover thermostat to each slice.

Unfortunately, this simple modification is not satisfactory for our system. In a system containing liquid-crystal molecules streaming around a colloid the sliced thermostated system would lead to artifacts such as freezing or viscous heating. This is due to the fact that the colloidal particle greatly affects the thermostating of the slices containing parts of it. Figure 13 shows a representative sketch of a system thermostated with a sliced Nosé-Hoover thermostat. A given molecule $i$ close to the colloid has a very different energy than molecule $j$ that is streaming rather freely in the system. The molecule $i$ is strongly attracted by the colloid, whereas molecule $j$ further away is almost not influenced by the colloidal particle. However, both molecules can belong to the same slice. Thus, if the Hamiltonian is only calculated for each slice and does not take more local effects into account the system becomes somewhat artificial. Let's assume that molecule $i$ is slowed down by the colloid and molecule $j$ is not affected by the colloid. If the contribution of molecule $i$ to the Hamiltonian is too high, too little energy is taken away from molecule $j$ and the system undergoes viscous heating. Conversely, if molecule $j$ is dominating the Hamiltonian too much energy will be subtracted from molecule $i$ and the system begins to freeze. What becomes clear from those observations is that a system with a highly inhomogeneous spatial distribution of kinetic energy demands a more elaborate thermostating to reach a constant global temperature. One has to apply a truly local thermostat.

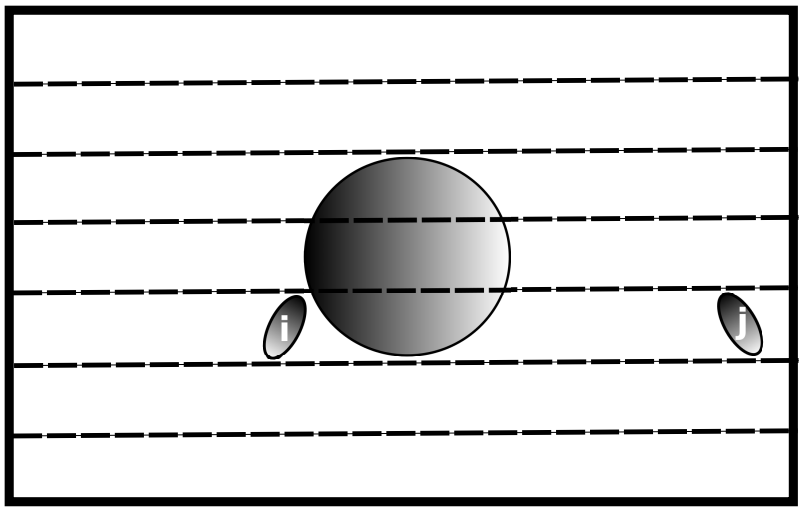


Figure 13: A schematic representation of the sliced Nosé-Hoover thermostat where the gray circle at the center represents the colloid and molecules $i$ and $j$ are representative liquid-crystal molecules.

In this work we use a novel thermostat that is based on pairwise interactions and was first introduced by Stoyanov and Groot [66, 143]. This thermostat is local and Galilean invariant and therefore conserves local momentum. In contrast to the Nosé-Hoover thermostat it acts on pairs of molecules rather than on single molecules.

The Stoyanov-Groot thermostat considers a thermostating force acting on the molecules $i$ and $j$

$$\boldsymbol{F}_{ij} = \lambda\psi(r_{ij}/r_c)\left[1 - \frac{1}{2}(T_i + T_j)/T_0\right][(\boldsymbol{v}_i - \boldsymbol{v}_j)\cdot\hat{\boldsymbol{r}}_{ij}]\hat{\boldsymbol{r}}_{ij}/\delta t, \tag{4.103}$$

where $\lambda$ is a thermostat coupling parameter, $\psi = 1 - r_{ij}/r_c$ is a smearing function, $r_c$ a cutoff radius, $T_0$ is the desired temperature, and $T_i$ is the local temperature of molecule $i$. If the temperature $T_i$ is lower than the desired temperature $T_0$ the thermostating force is putting energy back into the system, otherwise energy dissipates out of the system. Notice, if the desired temperature $T_0$ is reached the thermostating force vanishes. The Stoyanov-Groot thermostat is completely deterministic, like the Nosé-Hoover thermostat. Thus, it is very efficient in terms of computer time. The coupling parameter $\lambda$ stays constant during a simulation in contrast to the Nosé-Hoover thermostat. The local temperature $T_i$ in Eq. 4.103 for molecule $i$ can be obtained from

$$k_{\mathrm{B}}T_i = \frac{\sum_j \zeta(r_{ij}/r_c)M_{ij}(\boldsymbol{v}_i - \boldsymbol{v}_j)^2}{3\sum_j \zeta(r_{ij}/r_c)}, \tag{4.104}$$

where we choose the smearing function $\zeta = \psi$ and $M_{ij} = m_i m_j/(m_i + m_j))$ is the reduced mass. In principle the smearing function $\zeta$ and the cutoff radius $r_c$ employed for local temperature [see Eq. 4.104] can be different from the ones used for the thermostating

force [see Eq. 4.103].

## 4.6 Hoover barostat

The simulations in this work are equilibrated under constant pressure $P$. Hence, if one wants to work in an $NPT$ ensemble a barostat has to be applied as well. It is convenient to consider the volume $V$ of the system as a dynamical variable which changes over time during a simulation. The isobaric ensemble is once again realized by an extended ensemble approach proposed by Hoover [142]. The Lagrangian of a system in contact with a barostat may be written as

$$\begin{aligned} \mathcal{L}_V &= \mathcal{K} + \mathcal{K}_V - \mathcal{V} - \mathcal{V}_V \\ &= \sum_{i=1}^{N} \frac{m_i}{2} \boldsymbol{v}_i^2 + \frac{B}{2}\dot{V}^2 - \mathcal{V} - PV, \end{aligned} \tag{4.105}$$

where $B$ is a mass parameter, $\boldsymbol{r}$ and $\boldsymbol{v}$ are written in terms of a scaling variable $b$

$$\begin{aligned} \boldsymbol{r} &= V^{1/3}\boldsymbol{b}, \\ \boldsymbol{v} &= V^{1/3}\dot{\boldsymbol{b}}. \end{aligned} \tag{4.106}$$

The equations of motions obtained from the Lagrangian are

$$\ddot{\boldsymbol{b}} = \frac{\boldsymbol{F}}{mV^{1/3}} - \frac{2\dot{\boldsymbol{b}}\dot{V}}{3V}, \tag{4.107}$$

$$\ddot{V} = \frac{\mathcal{P} - P}{B}, \tag{4.108}$$

where $\mathcal{P}$ is the instantaneous pressure. The Hamiltonian $\mathcal{H}_V = \mathcal{K} + \mathcal{K}_V + \mathcal{V} + \mathcal{V}_V$ of the system is conserved. With the aid of the virial expression [145] one obtains the pressure tensor

$$\mathbf{P} = \frac{m}{V}\left\langle \sum_{i=1}^{N-1} \left[ (\boldsymbol{v}_i - \boldsymbol{v}) \otimes (\boldsymbol{v}_i - \boldsymbol{v}) + \sum_{j=i+1}^{N} \boldsymbol{r}_{ij} \otimes \boldsymbol{F}_{ij} \right] \right\rangle, \tag{4.109}$$

where $\boldsymbol{v} = v_\infty \hat{\boldsymbol{e}}_x$ is the flow velocity. This leads directly to the instantaneous pressure $\mathcal{P} = \frac{1}{3}\mathrm{Tr}\mathbf{P}$ [119].

## 4.7 Flow in molecular dynamics

The continuum theory by Ericksen, Leslie and Parodi [see Sec. 2.2] is very complex and rather difficult to handle. For most cases the Ericksen-Leslie equations cannot be solved analytically. One can refer to procedures such as finite difference, finite element, finite volume methods, or Lattice-Boltzmann simulations to solve the nematodynamic equations.

This is an entirely valid and feasible approach to study nematic liquid crystals under flow from a theoretical angle. However, one major drawback of the Ericksen-Leslie-Parodi theory is that it does not involve expressions for disinclination lines or point defects. Topological defects may play a crucial role and their evolution due to flow is of particular interest in this work. Thus, we approach the task from a different perspective. We avoid the nematodynamic equations completely and use nonequilibrium molecular dynamics simulations to tackle the problem [30].

Flow can be introduced quite simply in molecular dynamics. In a simulation box filled with liquid-crystal molecules one needs to apply a constant body force $F_e$ to each molecule. It is convenient to choose a common direction, here along the $x$-axis, for $F_e = \boldsymbol{F} \cdot \hat{\boldsymbol{e}}_x$. Hence, all molecules are dragged along the $x$-direction which can be compared to the effect gravity or an external field would have on the molecules. In other words, this creates a flow of liquid-crystal molecules along the $x$-axis from $-\infty$ to $+\infty$. Here we are interested in systems where either a colloid is dispersed in the host phase or a cylindrical pillar is introduced in the simulation cell. Thus, the symmetry of the system is broken in both cases. Applying a constant body force $F_e$ to the molecules located in the slipstream of the colloid would be somewhat artificial. Therefore, it is reasonable to introduce an additional constraint on $F_e$. We restrict the application of the constant force $F_e$ to molecules in a three-dimensional slice of width $2\sigma$ perpendicular to the $x$-direction. This slice is located at the beginning of the simulation box with respect to the direction of flow. The remaining molecules are pushed by the accelerated ones thus inducing a flow along the $x$-axis. However, this ensures that molecules are not artificially dragged out of the slipstream of the colloid.

In conclusion, the flow of a nematic liquid crystal can be tackled with molecular dynamics simulations in a more straightforward approach than solving the nematodynamic equations. However, one has to consider that the effort here lies in the numerical details and procedures of the molecular dynamics simulation. Firstly, it has to be ensured that a reasonably fast computer algorithm is developed to treat large enough systems. Secondly, additional methods, such as thermostats [see Sec. 4.5], tend to be more sophisticated under nonequilibrium conditions, like flow.

# 5 Results

## 5.1 Simulation protocol

In this thesis all quantities of interest are given in the usual dimensionless (i.e., "reduced") units. Taking $m$, $\sigma$, and $\varepsilon$ as basic units of mass, length, and energy, respectively, all other properties can be expressed in terms of suitable combinations of these basic quantities. For example, temperature is given in units of $\varepsilon/k_{\mathrm{B}}$, density in units of $\sigma^{-3}$, pressure in units of $\varepsilon/\sigma^3$, viscosity in units of $\sqrt{m\varepsilon}/\sigma^2$, and the Frank elastic constant in units of $\varepsilon/\sigma$ which is also the unit in which force is cast. Finally, in the nonequilibrium molecular dynamics simulations time is expressed in units of $\sqrt{m/\sigma^2\varepsilon}$ and velocity in units of $\sqrt{\varepsilon/m}$.

All simulations reported here have been carried out for a host phase containing $N = 24000$ molecules in a volume $V = s_x s_y s_z$. To make sure that the host phase is sufficiently deep in the nematic phase we choose $T = 0.90$ and, under isothermal-isobaric conditions, a pressure $P = 1.80$. For this thermodynamic state point we obtain a mean number density of $\overline{\rho} = N/\langle V \rangle \simeq 0.85$ in the bulk where $V$ denotes the (instantaneous) volume of the simulation box. We consider a system were molecules are confined between two planar atomistic substrates in the $z$-direction exhibiting planar anchoring. A colloidal particle is fixed in space at the center of the simulation cell. Figure 14 shows a sketch of the simulation cell.

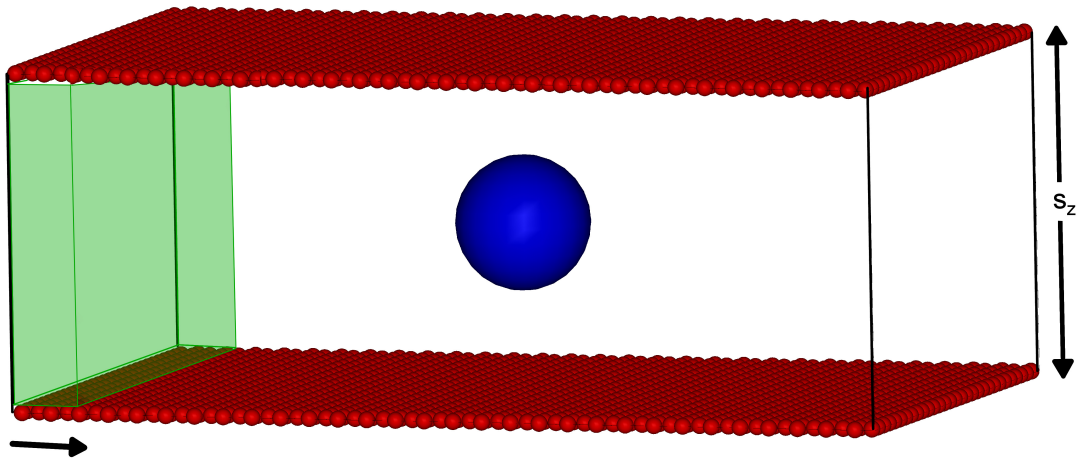


Figure 14: Sketch of the empty simulation cell with the discrete walls and a colloid. The green shaded area marks where the driving force $F_e$ is applied [see Sec. 4.7].

Fluid-fluid interactions [see Eq. 3.60] have been cut off if the center-of-mass distance between two molecules exceeds $r_c = 3.00$. For computational efficiency, we employ a Verlet neighborlist. Furthermore, we consider a much larger shell of neighbors then necessary to avoid frequent updates of the neighborlist under high-flow conditions. A molecule is considered a neighbor of a reference molecule if their centers of mass are separated by $r_N \leq 6.00$.

In the nonequilibrium simulations the equations of motion are integrated with a time step of $\delta t = 10^{-3}$ employing the velocity Verlet algorithm already described in Secs. 4.2 and 4.3. A steady-state Poiseuille flow is induced along the $x$-axis by applying a body force $\boldsymbol{F}_\mathrm{e} = F_\mathrm{e}\hat{e}_x$ [see Sec. 4.7].

Because of the external body force the system needs to be thermostatted permanently to achieve a stationary nonequilibrium state. As we explain in great detail in Sec. 4.5 the choice of a particular thermostat is of vital importance here because of the presence of the colloidal particle.

The molecular dynamics simulations are carried out according to the following protocol: (*i*) We generate a liquid-crystal fluid in equilibrium with the colloid and the solid substrates in the absence of flow ($F_\mathrm{e} = 0$), and in the isothermal-isobaric ($NPT$) ensemble. Typically, the evolution of the system is followed over $10^5$ time steps. (*ii*) Starting from the last configuration we perform a second equilibration in the canonical ($NVT$) ensemble under flow conditions ($F_e > 0$). The goal of this simulation stage is to generate a steady state nonequilibrium state. We monitor the kinetic and potential energies, and the velocity profile. This part of the simulation is performed for $5.0 \times 10^5$ time steps. (*iii*) Finally, the simulations are extended for another $1.5 \times 10^6$ time steps during which quantities of interest are sampled. For the computation of local quantities we divide our system by means of a grid with cubic cells of side length 0.2.

## 5.2 Measures of flow

Before discussing the main findings of this work it seems appropriate to characterize the regime of flows studied. Therefore, we need to recall the dimensionless numbers introduced in Sec. 2.5. In order to obtain the range of Ericksen $\mathcal{E}$ and Reynolds numbers $\mathcal{R}$ studied we calculate the elastic constants and the effective viscosity for our system.

In Sec. 1.8 we derived how to calculate the elastic constants in molecular dynamics simulations. To obtain $E_{13}$ and $E_{23}$ bulk simulations are performed in the $NVT$ ensemble with neither a colloid nor flow for different values of $N$ and $V$, while keeping the number density $\bar{\rho}$ fixed.

In Fig. 15(a) and (b), we show the dependence of $E_{13}$ and $E_{23}$ on $k_1^2$ and $k_3^2$ [see Eqs. 1.30 and 1.31]. As predicted from the theory, a linear fit can be applied for not too large values of the wave vectors. We note that the slopes of the two fits are almost

identical. In our calculations we find elastic constants $K_1 \approx K_2 \approx K_3 \approx K \approx 1.6$. The fact that the observed elastic constants of our system are equal, within statistical accuracy, is due to the rather small asphericity of liquid-crystal molecules in the Hess-Su model. Usually, the elastic constant $K_3$ is higher than the elastic constants $K_1$ and $K_2$. But for molecules of nearly spherical shape the bend configuration is energetically more or less equal to the splay and twist configuration. This is obviously not the case for much more elongated molecules that are truly anisotropic in shape, as is the case for the Gay-Berne model of liquid crystals [40–42].

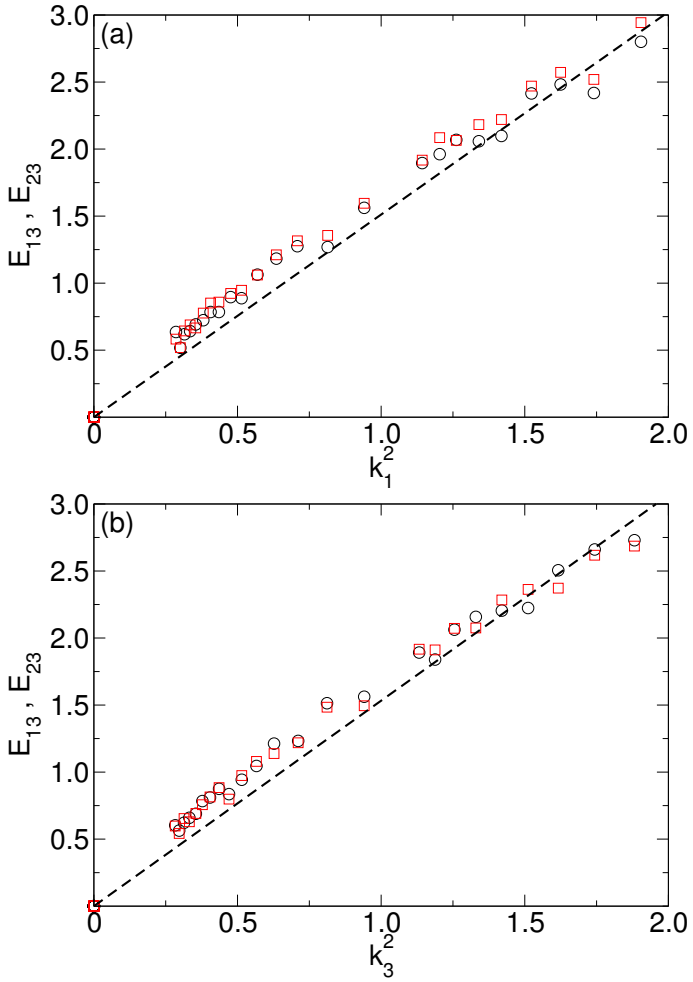


Figure 15: Dependence of $E_{13}(k_1^2, k_3^2)$ (black circles) and $E_{23}(k_2^2, k_3^2)$ (red squares) on (a) $k_1^2$ for $k_3^2 = 0$ as well as on (b) $k_3^2$ for $k_1^2 = 0$.

An important quantity to characterize the dynamic state is the effective viscosity. In Sec. 2.4 we have derived an equation that captures the parabolic shape of the velocity profile for Poiseuille flow [see Eq. 2.52]. To generate a streaming velocity profile $NVT$ simulations without a colloid for different external driving forces $F_e$ were performed. The simulation box is separated into slices of constant volume $s_x s_y \triangle z$, where $\triangle z = 0.2$.

Figure 16 shows the velocity profiles obtained with the recipe just described. A second-order polynomial provides a reasonably good fit of $v_x(z)$. From the fit we find $\eta \approx 40$.

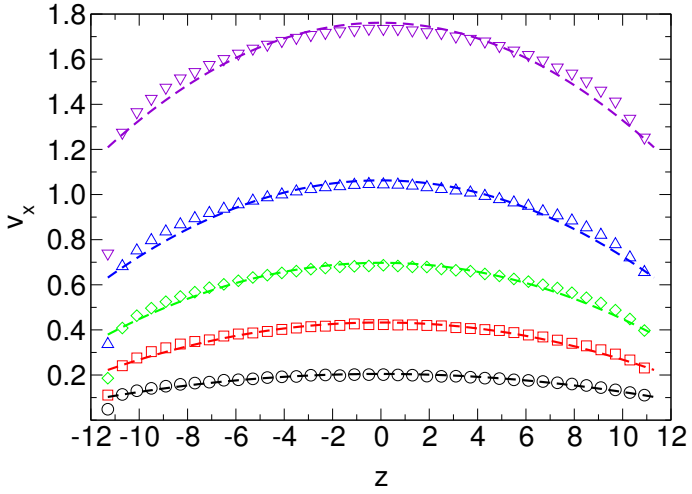


Figure 16: Streaming velocity profile for external driving forces $F_e = 0.1$ (circles), $F_e = 0.2$ (squares), $F_e = 0.3$ (diamonds), $F_e = 0.4$ (triangle up), $F_e = 0.5$ (triangle down) and corresponding second-order polynomial fits (dashed lines). For the sake of clarity we show every third data point.

With the aid of Eqs. 2.54 and 2.56 we can calculate the Reynolds number $\mathcal{R}$ and the Ericksen number $\mathcal{E}$, respectively. In Tab. 1 we list $\mathcal{R}$ and $\mathcal{E}$ for the flow regime studied in this work. Streaming velocities $v_\infty$ are obtained from $NVT$ simulations of the confined liquid-crystal fluid in the presence of the colloid for different external driving forces $F_e$. From Table 1 we see that over the range of streaming velocities considered, $\mathcal{R} \ll 1$. Therefore, all steady-state nonequilibrium states belong to the regime of laminar flow. Additionally, viscous effects dominate over elastic ones as indicated by the inequality $\mathcal{E} \gg \mathcal{R}$. However, we stress that the order of magnitude of both dimensionless numbers is in good agreement with recent microfluidic experimental studies [52].

| $F_e$ | $v_\infty$ | $\mathcal{R}$ | $\mathcal{E}$ |
|---|---|---|---|
| 0.10 | 0.12 | 0.08 | 93 |
| 0.20 | 0.25 | 0.17 | 193 |
| 0.30 | 0.39 | 0.26 | 302 |
| 0.40 | 0.55 | 0.36 | 426 |
| 0.50 | 0.71 | 0.47 | 550 |

Table 1: Reynolds numbers $\mathcal{R}$ and Ericksen numbers $\mathcal{E}$ for different external driving forces $F_e$ and corresponding streaming velocities $v_\infty$ used in our simulations.

The applied flow exhibits the known velocity profile for Poiseuille flow [see Fig. 16]. To gain further insight into the flow conditions. We study the velocity field around a colloidal particle dispersed in a nematic liquid crystal for different Ericksen numbers $\mathcal{E}$. In

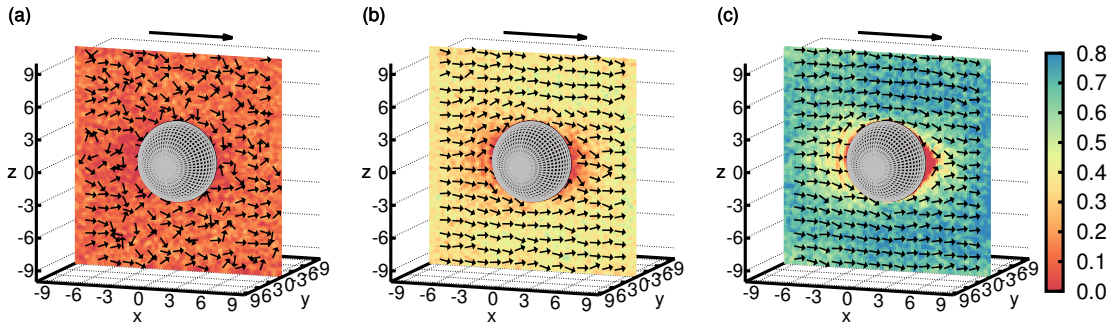


Figure 17: Maps of the magnitude of the local velocity $v_{\rm p}(\boldsymbol{r}_{\rm p})$ in the $x$-$z$ plane located at $y = 0$ [see attached color bar]. The long arrow above each plot gives the direction of flow. Small arrows in the maps give the local direction of flow represented by $\hat{\boldsymbol{v}}_{\rm p}(\boldsymbol{r}_{\rm p}) \equiv \boldsymbol{v}_{\rm p}(\boldsymbol{r}_{\rm p})/v_{\rm p}(\boldsymbol{r}_{\rm p})$. (a) $\mathcal{E} = 93$, (b) $\mathcal{E} = 302$, and (c) $\mathcal{E} = 550$.

Fig. 17 we present maps of the average velocity field in a $x$-$z$ cross section of the system

$$\boldsymbol{v}_{\rm p}(\boldsymbol{r}_{\rm p}) = v_x(\boldsymbol{r}_{\rm p})\hat{\boldsymbol{e}}_x + v_z(\boldsymbol{r}_{\rm p})\hat{\boldsymbol{e}}_z, \tag{5.110}$$

where $\boldsymbol{r}_{\rm p}$ is a point in the $x$-$z$ plane at $y = 0$ and $v_\alpha(\boldsymbol{r}_{\rm p}) = \boldsymbol{v}(\boldsymbol{r}_{\rm p}) \cdot \hat{\boldsymbol{e}}_\alpha$ ($\alpha = x, y$). One can see that with increasing flow (i.e., with increasing $\mathcal{E}$) the average local velocity increases steadily. Whereas for the smallest $\mathcal{E}$ the distribution of velocities across the $x$-$z$ plane is relatively homogeneous [see Fig. 17(a)], as $\mathcal{E}$ increases this distribution becomes more and more inhomogeneous in a region centered on the colloid's equator (i.e., around $z = 0$) [see Figs. 17(b) and (c)]. Two stagnation points emerge at the leading and trailing point on the colloid's surface with respect to the flow direction. In particular, from the plot in Fig. 17(c) it is evident that the average magnitude of $\boldsymbol{v}_{\rm p}(\boldsymbol{r}_{\rm p})$ is more strongly reduced on the upstream side of the colloid compared with the downstream side, matching one's physical intuition. As we will rationalize in the next section, it is this inhomogeneity of the velocity field that is ultimately responsible for the elastic deformation of disclination rings in sufficiently strong flow.

One also notices from the plot in Fig. 17(a) that at low $\mathcal{E}$ the velocity field exhibits rather strong fluctuations *locally* whereas *globally* the flow is in the direction of $\boldsymbol{F}_{\rm e}$. As $\mathcal{E}$ increases $\hat{\boldsymbol{v}}$ becomes more and more aligned with $\boldsymbol{F}_{\rm e}$. Because $\boldsymbol{F}_{\rm e}$ is parallel to $\hat{\boldsymbol{n}}_0$ we observe an increasingly larger alignment of the flow field with the far-field director.

## 5.3 Effects of flow on topological defects

We study the effects of flow on defect topologies around a colloid dispersed in a nematic host phase under flow well within the laminar flow regime. First, we will focus on homogeneous colloids and analyze the change of the defect topologies qualitatively. In particular, we focus on the direction of movement and the deformation of the defect topology due to the flow. Second, we quantitatively examine the Saturn ring defect of a heterogeneous colloid with perpendicular anchoring. Thus, we examine the length of the ring defect and the degree of deformation for different flow speeds. We pay particular attention to the influence of the anchoring strength on the size and position of the Saturn ring defect. Last, we present the first study on heterogeneous colloids subject to flow. More specifically, we investigate the defect topologies emerging around Janus colloids dispersed in a flowing nematic liquid crystal.

## 5.4 Displacement and deformation of defects

Figures 18(a)-(c) show three-dimensional representations of the defect structures around a homogeneous colloid with planar anchoring for different Ericksen numbers $\mathcal{E}$. We mark only locations with a local nematic order parameter $S(\boldsymbol{r}) \leq 0.2$, which we arbitrarily choose to represent the defect structures. Figures 18(d)-(e) show cross-sectional maps of the local nematic order parameter $S(\boldsymbol{r})$ and of the local director $\hat{\boldsymbol{n}}(\boldsymbol{r})$ for the same conditions as in Figs. 18(a)-(c). The cross-sections are taken along the $x$-$z$-plane that goes through the center of the colloid and the defect topologies ($y = 0$).

Colloidal suspensions of a homogeneous colloid with planar local anchoring in a nematic liquid crystal are known to form Boojum defects [43]. Fig. 18(a) shows that in the system at rest ($\mathcal{E} = 0$) a Boojum defect topology arises due to the strong planar anchoring of the molecules on the colloid surface. This is indicated as well by the low values of $S(\boldsymbol{r})$ on the left (negative $x$-axis) and right (positive $x$-axis) side of the colloid in Fig. 18(d). In these areas $\hat{\boldsymbol{n}}(\boldsymbol{r})$ is oriented planar to the colloidal surface, and therefore perturbs the global director field $\hat{\boldsymbol{n}}_0$. Notice that, sufficiently far away from the colloid, $\hat{\boldsymbol{n}}(\boldsymbol{r}) = \hat{\boldsymbol{n}}_0 \simeq \hat{\boldsymbol{e}}_x$, the director field matches approximately the far-field director $\hat{\boldsymbol{n}}_0$. The alignment of $\hat{\boldsymbol{n}}_0$ with $\hat{\boldsymbol{e}}_x$ is a consequence of the anchoring of molecules at both solid substrates [see Eq. 3.65].

For $\mathcal{E} > 0$, the upstream lobe of the Boojum defect shrinks [see Figs. 18(b) and (c)] because the molecules on the upstream side of the colloid are squeezed more tightly against the colloid with increasing $\mathcal{E}$ which results in their enhanced ordering; at the same time the lobe of the Boojum defect in slipstream of the colloid grows in size because molecules are locally decompressed in the slipstream, resulting in a disordering effect. Figures 18(e) and (f) show in detail the compression of the upstream Boojum lobe and the expansion

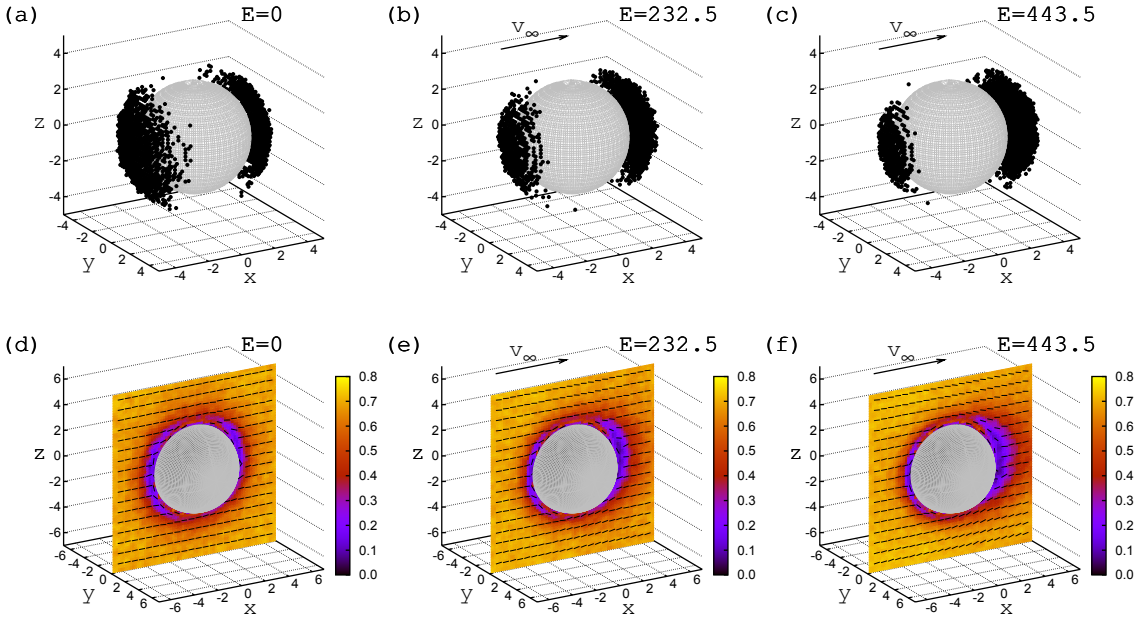


Figure 18: (a)-(c) A three dimensional representation of the defect structures ($S(\boldsymbol{r}) \leq 0.2$) around a homogeneous colloid (gray sphere). (d)-(f) Cross-section along the $x$-$z$ plane of the local nematic order parameter $S(\boldsymbol{r})$, where the color indicates the magnitude of $S(\boldsymbol{r})$, as well as the local director $\hat{\boldsymbol{n}}(\boldsymbol{r})$ represented by a black line. Plots are generated for different Ericksen numbers $\mathcal{E}$ for a colloid with planar anchoring and the black arrow indicates the direction of the streaming velocity $v_\infty$.

of the slipstream one.

Figure 19 is as Fig. 18 but for the case of perpendicular anchoring. When homogeneous colloids with perpendicular anchoring are dispersed in a nematic liquid crystal they are known to form Saturn ring defect structures [44]. Thus, when no external driving force is applied ($\mathcal{E} = 0$) a Saturn ring defect topology arises around the colloid, because of the strong perpendicular anchoring applied in our simulations [see Fig. 19(a)]. The Saturn ring defect topology is also indicated by the low values of $S(\boldsymbol{r})$ at the north (positive $z$-axis) and south pole (negative $z$-axis) of the colloid [see Fig. 19(d)]. In these areas the director field is strongly distorted because the anchoring opposes the far-field director.

Our molecular dynamics simulations show that for $\mathcal{E} > 0$ the defect structures [see Figs. 19(b) and 19(c)] are distorted and convected along with the flow in $x$-direction. This is also indicated by the position of the area of low nematic order in Figs. 19(e) and 19(f). This contradicts the results found by Gettelfinger *et al.* [64] but is in agreement with earlier theoretical studies [61–63] as well as experimental work by Khullar *et al.* [1].

As $\mathcal{E}$ increases, the local nematic director $\hat{\boldsymbol{n}}(\boldsymbol{r})$ at the north and south pole of the

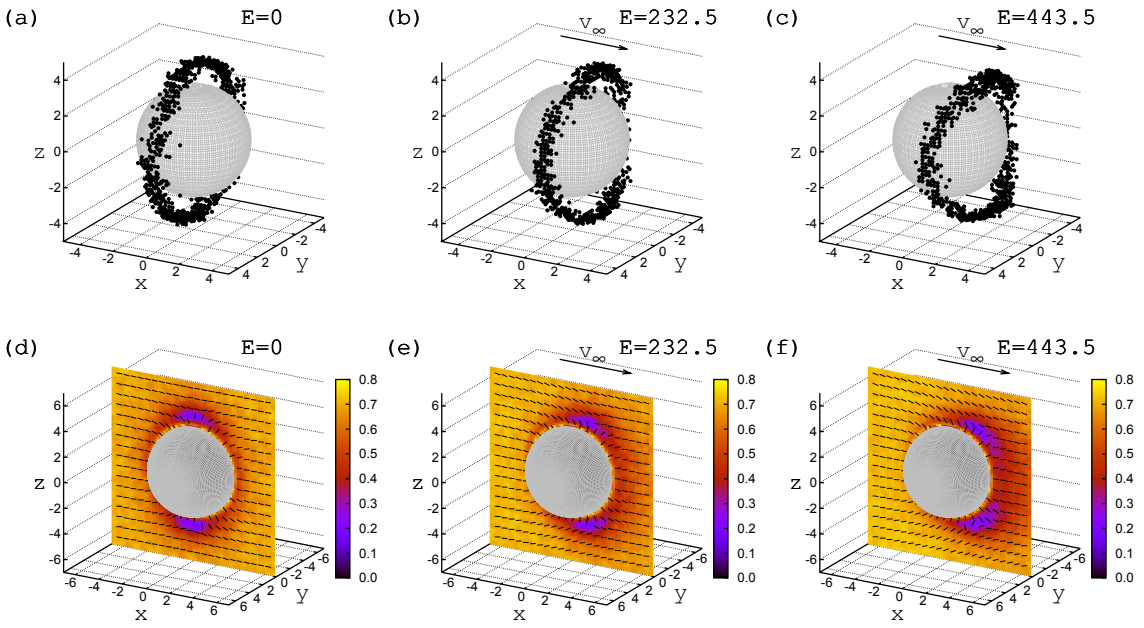


Figure 19: As Fig. 18 but for a homogeneous colloid with perpendicular anchoring.

colloid becomes more and more parallel to the global director $\hat{\boldsymbol{n}}_0$. For $\mathcal{E} > 0$ the Saturn ring defect deforms and moves downstream along the $x$-direction [see Fig. 19(c)]. The deformation takes the shape of a mouth. Therefore, we refer to this deformation as stomal defect. Fig. 20 shows the reason for this deformation. We calculate the $x$-component of the velocity $v_x$ averaged over a plane perpendicular to the $z$-axis, and study its dependence on $z$. We repeat the calculation for planes perpendicular to the $y$-axis to study the dependence of $v_x$ on $y$ as well. On the colloidal surface $v_x(z) > v_x(y)$, that is, the molecule moving between the north (south) pole and the top (bottom) wall move faster than the molecules on the equator of the colloid.

An interaction of the Saturn ring and confining walls was observed in experiments by Khullar *et al.* [1]. In their case the walls of the experimental cell have a pinning effect on the defect, which, we deduce, drastically reduces the velocity of the liquid crystal fluid between colloid and walls. Thus, the section of the Saturn ring closer to the walls moves slower than the sections at 90° from them. Despite the much larger colloids used in the experiments the structural changes illustrated in Fig. 19(c) are general and, at least from a qualitative perspective, independent of the size of the colloid.

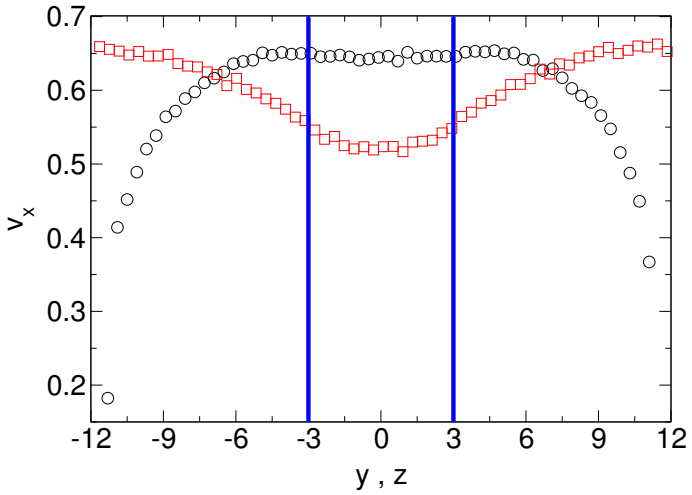


Figure 20: Streaming velocity profile for a homogeneous colloid with perpendicular anchoring for a Ericksen number $\mathcal{E} = 443.5$ along the $y$- (squares) and $z$-direction (circles) where blue lines represent the diameter of the colloid. For the sake of clarity we show every second data point.

## 5.5 Influence of the anchoring strength

We have established the displacement and deformation of defect topologies because of flow. Therefore, we focus on the Saturn ring defect in order to quantitatively explore the perturbation of the Saturn ring defect from its equilibrium shape. However, even in equilibrium the exact position of the Saturn ring defect with respect to the colloidal surface can be modulated by the anchoring strength of the colloid [see Eq. 3.69]. Thus, it seems instructive to give some information about the anchoring strength of liquid-crystal molecules at the surface of the colloid. We estimate the anchoring strength at the colloidal particle through the time average of the fluid-colloid potential energy per surface area of the colloid $W = -\langle \Phi_{\mathrm{fc}} \rangle / 4\pi r_0^2$. The value of $W$ depends somewhat on the inverse screening length $\lambda$ of $\varphi_{\mathrm{fc}}$ [see Eq. 3.69]. For example, $W \simeq 1.8 \times 10^{-2}\mathrm{Jm}^{-1}$ for $\lambda = 2.0$ (shortest-range interaction considered here) whereas $W \simeq 8.4 \times 10^{-2}\mathrm{Jm}^{-1}$ for $\lambda = 0.2$ (longest-range interaction) where we have assumed $\varepsilon k_{\mathrm{B}}^{-1} = 120\mathrm{K}$ and $\sigma = 3.4 \times 10^{-10}$ m for simplicity.

The values of $W$ for our model correspond to strong anchoring conditions and agree in magnitude with those used in a recent numerical study of colloidal particles dispersed in a nematic liquid crystal exhibiting Saturn ring defect topologies [146]. Similar orders of magnitude are common for liquid-crystal anchoring on different types of planar surfaces [31].

Figure 21 shows $S(\boldsymbol{r})$ and the associated director field $\hat{\boldsymbol{n}}(\boldsymbol{r})$ for nonspecific anchoring (i.e., for $g_c = 1$) under various flow conditions. As one moves closer to the colloid one observes locally homeotropic alignment of molecules near the colloid's surface even though $g_c = 1$. This results from the competition between energetic and entropic effects.

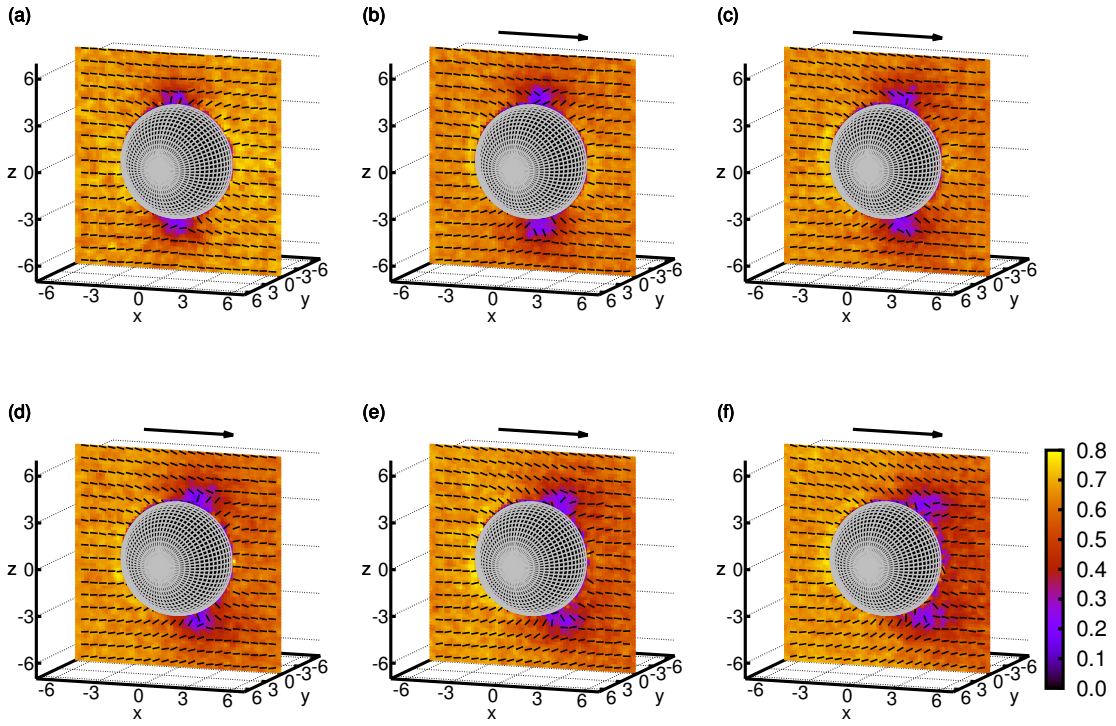


Figure 21: Maps of the local nematic order parameter $S(\boldsymbol{r}_{\mathrm{p}})$ in the $x$-$z$ plane at $y = 0$ [see attached color bar]. The circular area at the center represents the colloidal particle and the arrow above each plot indicates the direction of flow. Small dashes in the maps represent the director field. (a) $\mathcal{E} = 0$ (equilibrium), (b) $\mathcal{E} = 93$, (c) $\mathcal{E} = 193$, (d) $\mathcal{E} = 302$, (e) $\mathcal{E} = 426$, and (f) $\mathcal{E} = 550$. Plots have been generated for $g_c = 1.00$ and $\lambda = 0.50$ [see Eq. 3.69].

If molecules align their long axes parallel to the local surface normal of the colloid they lose some orientational entropy compared with a situation in which these axes are orthogonal to the local surface normal. This is because for homeotropic alignment only a single easy axis exists locally whereas for locally parallel alignment an infinite number of these axes obtains. Hence, the orientational entropy would be larger in this latter case.

However, from an energetic perspective locally planar or homeotropic alignments are nearly equivalent on account of the small aspect ratio of a molecule [see Sec. 3.2]. At the same time, packing at the curved surface of the colloid is more efficient in the case of locally homeotropic alignment. Consequently, the internal energy is lower for the locally homeotropic alignment such that the reduced configurational energy outweighs the loss in orientational entropy [68].

For $g_c = 1.00$ we observe that defects always stay very close to the surface of the colloid irrespective of $\lambda$. On the contrary, for $g_c$ as given by Equation 3.73, defects are displaced to regions further away from the surface as plots in Figure 22 reveal.

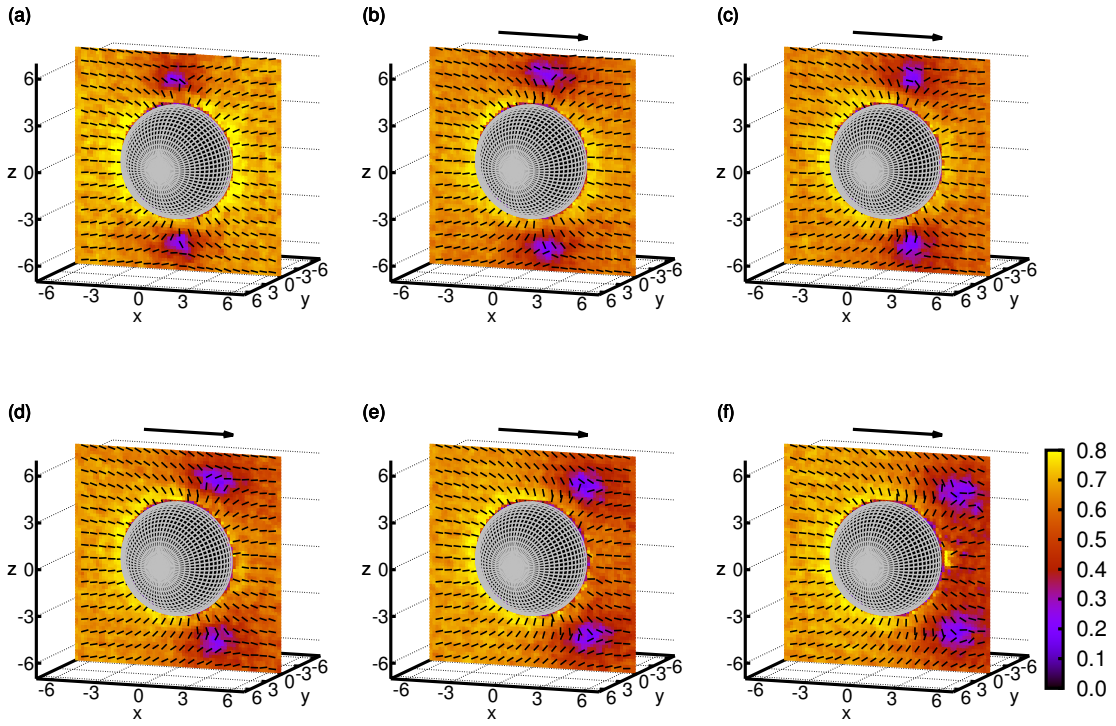


Figure 22: As Figure 21, but for $g_c$ as in Eq. 3.73.

## 5.6 Length and shape of disclination lines

Even though at thermodynamic equilibrium the quasi two-dimensional plots in Fig.s 21(a) and 22(a) correspond to ringlike disclination lines [68, 114, 147, 148] one anticipates their deformation under flow conditions, as is already evident from Figs. 19(a)-(c). Consequently, one has to resort to full three-dimensional plots of disclination lines in cases of non-zero $\mathcal{E}$ to capture these flow-induced deformations.

In molecule-based numerical approaches such as computer simulations defects manifest themselves as regions of low nematic order. As a definition of disclination lines we adopt

$$\ell = \left\{ \boldsymbol{r} = (x, y, z)^{\mathrm{T}} \middle| \, S(\boldsymbol{r}) \leq S_0 \right\}, \tag{5.111}$$

where the superscript T denotes the transpose of a vector and $S_0$ is a threshold value for $S(\boldsymbol{r})$. Obviously, the choice of $S_0$ is somewhat arbitrary. From an operational point of view $S_0 = 0.20$ provides an optimal visualization of $\ell$.

The plot in Fig. 23(a) illustrates the disclination line around a colloidal particle under flow conditions. To analyze the defect structure illustrated in Fig. 23(a) *quantitatively* we realize that for symmetry reasons its projection onto the $y$-$z$ plane [see Fig. 23(b)] is an

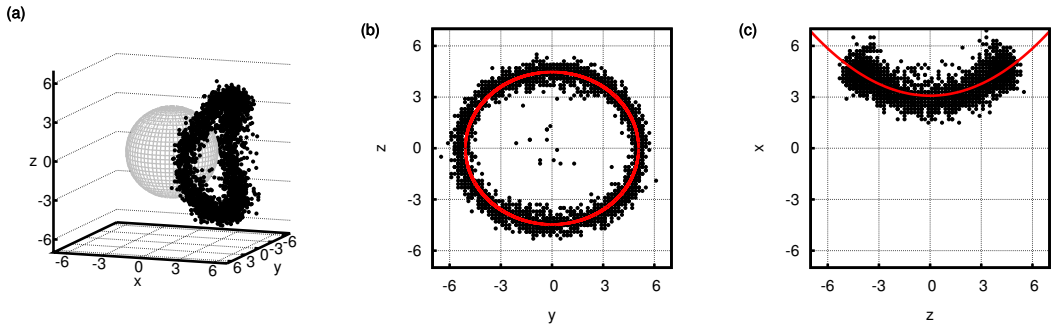


Figure 23: Disclination line near the surface of a spherical colloidal particle of hard-core radius $r_0 = 3.00$ and with an inverse screening length $\lambda = 0.50$. Data have been obtained under steady-state nonequilibrium conditions of the host phase characterized by Ericksen and Reynolds numbers $\mathcal{E} = 550$ and $\mathcal{R} = 0.47$, respectively. (b) As (a), but projected onto the $y$-$z$ plane. (c) As (a), but for a projection onto the $x$-$z$ plane. Red lines in parts (b) and (c) are fits of Eqs. 5.112 and 5.113 to the discrete data points, respectively.

ellipse whose equation in parametric form can be cast as

$$\begin{pmatrix} y \\ z \end{pmatrix} = \begin{pmatrix} a\cos t \\ b\sin t \end{pmatrix}, \qquad 0 \leq t \leq 2\pi, \tag{5.112}$$

where the ratio of principal axes $e = a/b$ defines the eccentricity of the ellipse. Similarly, a projection of the disclination line in Fig. 23(a) onto the $x$-$z$ plane can be described by a parabola [see Fig. 23(c)]

$$x = cz^2 + c_0 = cb^2 \sin^2 t + c_0. \tag{5.113}$$

Taking $a$, $b$, $c$, and $c_0$ as fit constants we compute the length $s$ of the disclination line via

$$s = \int_0^{2\pi} \mathrm{d}t \sqrt{\dot{x}^2 + \dot{y}^2 + \dot{z}^2} = \int_0^{2\pi} \mathrm{d}t \sqrt{a^2 \sin^2 t + b^2 \cos^2 t + 4c^2 b^4 \sin^2 t \cos^2 t}, \tag{5.114}$$

where the dot indicates a derivative with respect to the parameter $t$. However, on account of the complexity of the integrand on the far right side of Eq. 5.114 we have been unable to solve the expression for $s$ analytically in all cases. For the special case of an undeformed circular defect ring, for which $a = b$ and $c = 0$ the solution is straightforward and gives $s = 2\pi a^2$ as one would have guessed immediately. In the general case, instead, we solve Eq. 5.114 numerically using a simple trapezoidal rule and values for the constants $a$, $b$, and $c$ from the fitting procedure mentioned above.

Plots in Fig. 24 illustrate the impact of flow on the disclination lines. Figure 24(a) reveals that in the absence of flow the colloid is encircled by perfect circular rings where

the effective radius of the rings $r_{\text{eff}} > r_0$ is larger the smaller $\lambda$ is. The effective radius of disclination lines will always exceed $r_0$ because of repulsive fluid-colloid interactions [see Eq. 3.69], the finite kinetic energy of the molecules, and the fact that the minimum of $\varphi_{\text{fc}}$ is always located at a distance $r_0 + \sigma$ from the center of the colloid. The circular shape of defect lines remains basically unaltered at low $\mathcal{E}$.

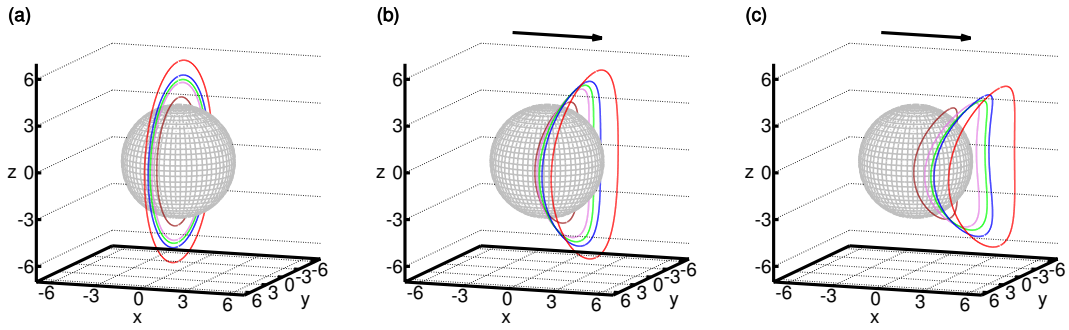


Figure 24: Three-dimensional representation of disclination lines $\ell$ [see Eq. 5.114] for $\lambda = 0.20$ (—), $\lambda = 0.50$ (—), $\lambda = 0.90$ (—), $\lambda = 2.00$ (—) (from outside inwards). In addition, data for $\lambda = 0.50$ and $g_\perp = 1.00$ (—) are shown (innermost ring). The arrow on top of the plots indicates the direction of flow. (a) $\mathcal{E} = 0$, (b) $\mathcal{E} = 302$, and (c) $\mathcal{E} = 550$.

At intermediate $\mathcal{E}$, Fig. 24(b) indicates a change in the disclination lines. Whereas they remain roughly circular in shape they are shifted downstream by an amount $c_0$ [see Eq. 5.113]. This shift is more pronounced for larger rings (i.e., for smaller $\lambda$). This can be understood if one realizes that molecules located along the disclination lines are more free to move the larger $r_{\text{eff}}$ becomes.

Finally, at large $\mathcal{E}$, Fig. 24(c) shows that besides moving the disclination line even further downstream, the rings are now significantly distorted by flow from a circular shape. The origin of this deformation is explained above and illustrated in Fig.20.

## 5.7 Perturbation of the Saturn ring defect

We now have derived the quantities necessary to further analyze the impact of the range of fluid-colloid interactions. Figure 25(a) shows that the length $s$ of the disclination line is a linear function of the screening length $1/\lambda$ both in the equilibrium system ($\mathcal{E} = 0$) and under flow ($\mathcal{E} \neq 0$). The curves are shifted with respect to one another such that under flow conditions disclination rings for the same screening length are generally shorter than in the equilibrium system.

To rationalize the apparent linear variation of $s$ with $1/\lambda$ shown in Fig. 25(a) we plot in Fig. 25(b) the perturbational free energy introduced in App. A [see Eq. A.127]. It

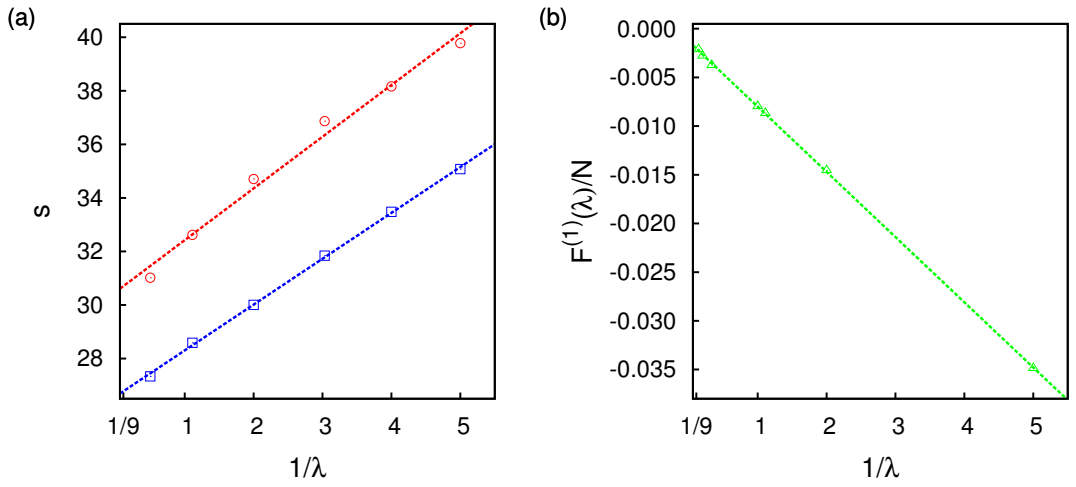


Figure 25: (a) Length of disclination lines $s$ as a function of the screening length $1/\lambda$ of the fluid-colloid interaction potential [see Eq. 3.69] for $\mathcal{E} = 0$ (○) and $\mathcal{E} = 550$ (□). (b) As (a), but for the per molecule perturbational free energy $\mathcal{F}^{(1)}(\lambda)$ [see Eq. A.127] and $\mathcal{E} = 0$ (△). In both panels dashed lines are linear least-squares fits to the calculated points obtained over the range where Eqs. 3.70 and 3.71 are valid [see also discussion in Section 3.4].

exhibits a similar linear dependence on $1/\lambda$ but with negative slope. These data have been obtained for the case of nonspecific anchoring $g_\perp = 1.00$ in corresponding Monte Carlo simulations [see App. B].

Nonspecific anchoring has been utilized here for reasons of computational convenience. It leads to a local homeotropic alignment of molecules at the surface of the colloid even in the reference system [see also Fig. 21]. We therefore conclude from Fig. 25 that a shift of the disclination rings to a larger distance from the surface of the colloid makes the system as a whole more stable as reflected by a similar decrease in free energy. This makes sense because at larger $1/\lambda$ the net attraction of molecules by the colloid increases [see Sec. 3.4 and Fig. 11] which results in a noticeable increase of local nematic order in the neighborhood of the colloid [see also Figs. 21 and 22].

Because the curves plotted in Fig. 25(a) are only shifted horizontally with respect to each other we expect a similar shift of the free energy in Fig. 25(b) due to the flow. However, the computation of a similar steady-state free energy in molecular dynamics is hampered by the hard-core background potential required by the perturbational approach on which Eq. A.127 is based.

To further analyze the variation in disclination-line length, we compute the displacement $c_0$ [see Eq.5.113] from our simulation results by applying the fit procedure described in Section 5.6. Results plotted in Fig. 26 for four values of $\lambda$ indicate that $c_0$ increases approximately linearly with the strength of flow (i.e., with $\mathcal{E}$). The linear increase of $c_0$

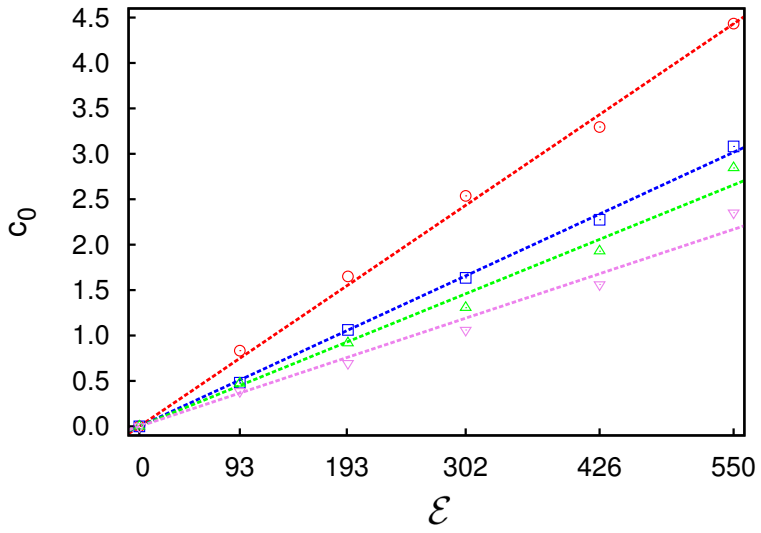


Figure 26: Displacement of disclination lines $c_0$ in downstream direction as a function of the Ericksen number $\mathcal{E}$ for $\lambda = 0.20$ (○), $\lambda = 0.50$ (□), $\lambda = 0.90$ (△), and $\lambda = 2.00$ (▽). Dashed lines are fits to the discrete data points.

with $\mathcal{E}$ makes sense if one recollects that $\mathcal{E}$ is directly proportional to the flow velocity [see Eq. 2.56]. The increase of $c_0$ with $\mathcal{E}$ is stronger for smaller $\lambda$ which is to be expected because larger disclination rings are prone to respond more strongly to flow than smaller ones for the same energetic reasons explained above.

One also notices from Fig. 24 that the circular shape of the disclination lines in the absence of flow is approximately preserved under flow conditions if $\mathcal{E}$ is not too large. Let us now assume these circular disclination lines maintain their distance from the surface of the colloid as they are displaced downstream. Moreover, let us assume them to preserve their circular shape upon displacement. Hence, the effective radius of the shifted disclination lines can be expected to satisfy the inequality $r'_{\text{eff}} < r_{\text{eff}}$ where $r'_{\text{eff}}$ is the radius of a circular disclination line displaced by flow.

Geometrically, the displaced disclination line forms the base of a spherical cap of radius $r'_{\text{eff}}$ shifted by an amount $c_0$ from the center of a sphere of radius $r_{\text{eff}}$ where the equator of the sphere marks the position of the disclination line in the absence of flow. This situation is sketched in Fig. 27.

Because of this idealized geometry it is easy to establish a relation between the length $s'$ of the displaced disclination line under flow, its radius at equilibrium $r_{\text{eff}}$, and the displacement from the equilibrium position $c_0$ in the downstream direction. Using elementary geometrical arguments allows one to conclude that [see Fig. 27]

$$s' = 2\pi\sqrt{2r_{\text{eff}}\,(r_{\text{eff}} - c_0) - (r_{\text{eff}} - c_0)^2}. \tag{5.115}$$

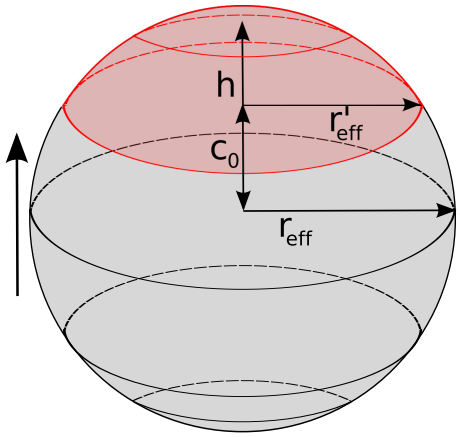


Figure 27: Spherical cap of radius $r'_{\text{eff}}$ and height $h$. The lower bound of the cap corresponds to a circular disclination line of radius $r'_{\text{eff}}$. This shorter disclination line is shifted by a distance $c_0$ in the direction of flow indicated by the vertical arrow. In the absence of flow the disclination line forms a circle of radius $r_{\text{eff}}$ around the equator of a colloidal particle of radius $r_0 < r_{\text{eff}}$ (not shown).

Notice that this expression does not contain any undetermined parameters. For example, $c_0$ is obtained from the fit procedure described in Section 5.6. Moreover, in the absence of flow disclination lines are perfectly circular. This implies that $a = b = r_{\text{eff}} > r_0$ in Eq. 5.112 and $c = 0$ in Eq. 5.113 such that $s = 2\pi r_{\text{eff}}$ follows trivially from Eq. 5.114 which allows us to compute $r_{\text{eff}}$ using $s$ from Eq. 5.114 directly from the simulation data in the limit $\mathcal{E} = 0$.

To test Eq. 5.115 we present plots of $s$ and $s'$ as functions of $c_0$ in Fig. 28(a). For sufficiently small $c_0$ all four plots reveal that the simulation data are represented quite nicely by Eq. 5.115 as expected. However, the applicability of Eq. 5.115 is limited as one might have guessed. For example, for the longest-range fluid-colloid interaction (i.e., the smallest $\lambda$), $s'$ underestimates $s$ systematically for ring displacements $c_0 \gtrsim 1.50$. As the rings move closer to the colloid's surface (i.e., as $\lambda$ increases) the range over which $s$ matches approximately $s'$ increases markedly.

We can take the analysis one step further and predict the values of $\mathcal{R}$ and $\mathcal{E}$ where the flow induces a transition from a defect line to a hedgehog defect [149]. Based upon the linear relation between $s$ and $\mathcal{E}$ observed in Fig. 26, it is straightforward to show from Eq. 5.115 that a similar relation holds, namely

$$s' = 2\pi\sqrt{2r_{\text{eff}}\,(r_{\text{eff}} - d\mathcal{E}) - (r_{\text{eff}} - d\mathcal{E})^2}, \tag{5.116}$$

where $d$ is the slope of the straight lines through the origin shown in Fig. 26 and obtained via a linear least-squares fit to the simulation data. Taking now as $\mathcal{E}_{\text{c}}$ the critical Ericksen number for which $s' = 0$ (i.e., for which $c_0 = r_{\text{eff}}$) and employing Eqs. 2.54 and 2.56 we

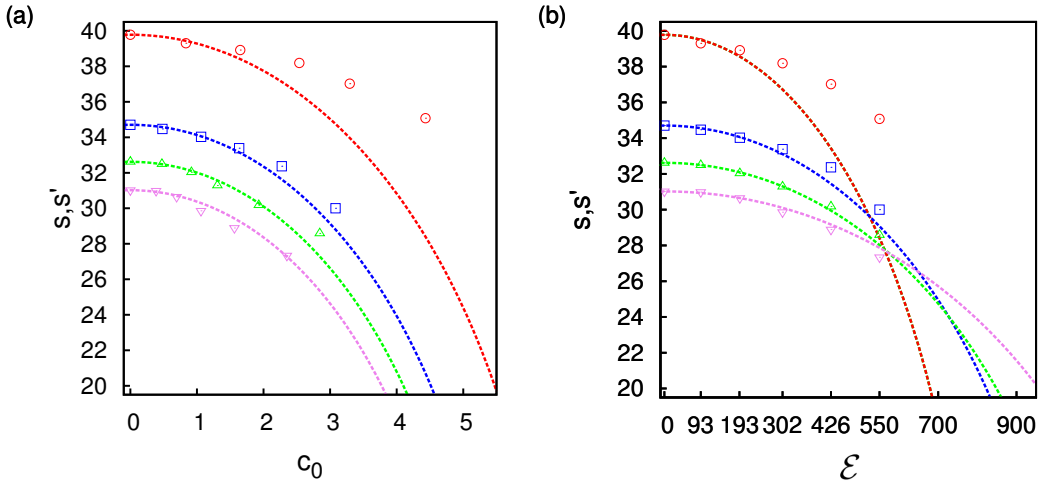


Figure 28: (a) Length $s$ of disclination rings obtained from Eq. 5.114 as a function of the downstream shift $c_0$ obtained through the fitting procedure described in Section 5.6 for $\lambda = 0.20$ (○), $\lambda = 0.50$ (□), $\lambda = 0.90$ (△), and $\lambda = 2.00$ (▽). Dashed lines are corresponding plots of $s'$ obtained via Eq. 5.115 where $r_{\text{eff}} = s/2\pi$ at $\mathcal{E} = 0.00$. (b) As (a), but as a function of the Ericksen number $\mathcal{E}$. Curves are given by Eq. 5.116.

arrive at

$$\mathcal{R}_{\text{c}} = \frac{\overline{\rho} K}{\eta^2} \mathcal{E}_{\text{c}} \tag{5.117}$$

for the critical Reynolds number at which disclination lines are transformed into a hedgehog defect due to flow. Based upon data for $\lambda = 2.00$ we estimate $\mathcal{E}_{\text{c}} = 1250$ which is less than a factor of 2 away from the largest $\mathcal{E}$ in Fig. 28(b). Using the mean density $\overline{\rho}$, shear viscosity $\eta$, and the elastic constant $K$ as given in Sec. 5.2 we estimate $\mathcal{R}_{\text{c}}$ as being of the order of one indicating that defect rings are expected to vanish under laminar flow conditions. Nevertheless, plots in Fig. 28(b) clearly show that the above analysis presumably underestimates $\mathcal{E}_{\text{c}}$ even for the largest $\lambda$ but may still be considered to give a reliable lower limit for $\mathcal{E}_{\text{c}}$.

The underestimation of $\mathcal{E}_{\text{c}}$ is a consequence of the fact that our analysis does not take into account any elastic deformation of disclination rings resulting in a deviation of their shape from that of a circle. That this deformation plays a crucial role in the response of defect rings to flow can be cast quantitatively in terms of the eccentricity $e$ and the curvature $c$ of the disclination rings in the various projections of $\ell$ [see Sec. 5.6]. In both parts of Fig. 29 we see that for the largest disclination rings investigated a noticeable deviation from a circular shape is obtained at rather small Ericksen numbers $\mathcal{E} \gtrsim 100$. This is fully in line with plots in Figs. 28(a) and 28(b) for the same $\lambda$ where we showed that the assumption of circularity of disclination rings under flow conditions becomes invalid at lower Ericksen numbers for larger disclination rings compared with smaller ones.

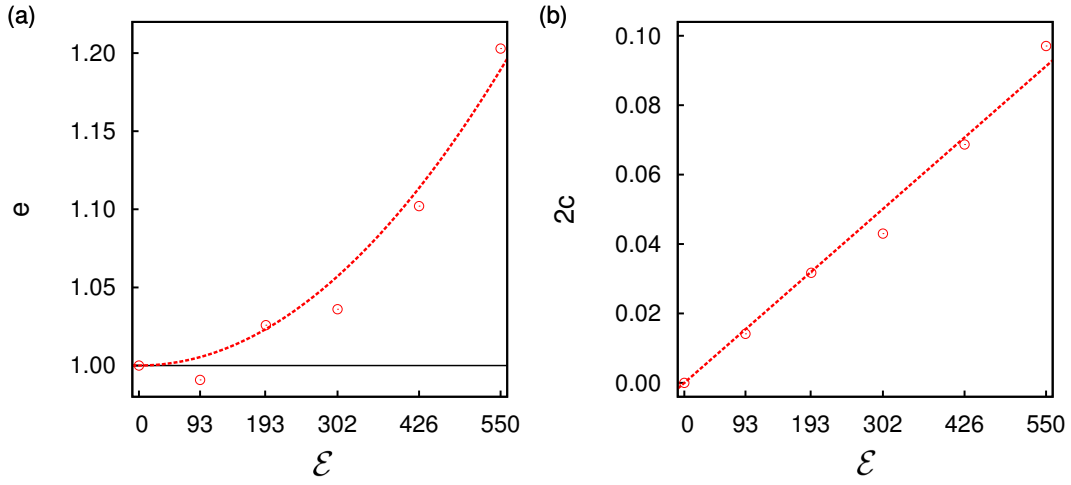


Figure 29: (a) Eccentricity $e$ of elliptic disclination rings as a function of the Ericksen number $\mathcal{E}$ (○). Ellipses are obtained from a projection of $\ell$ onto the $y$-$z$ plane. The horizontal line demarcates the circular limit of the projected $\ell$. (b) As (a) but for the curvature $c$ of parabolas obtained when $\ell$ is projected onto the $x$-$z$ plane [see Sec. 5.6]. Data are shown for $\lambda = 0.20$.

## 5.8 Janus colloid

In the previous sections we studied the effect of flow on well known defects of rather simple shape arising around homogeneous colloids. However, when these defects are subject to flow they are not only displaced in space but also deformed with respect to their equilibrium shape. We have extensively studied the deformation of the Saturn ring from a simple ring to a stomal shaped defect [see Fig. 23]. Thus, defect topologies are often more complex under flow conditions. Yet, there exists also more complex equilibrium defect topologies around heterogeneous colloids, such as Janus colloids [see Sec.2.10]. One can imagine that the study of defect topologies around heterogeneous colloids under flow leads to a vast variety of new defects. Here, we only show two different configurations as an example.

We performed molecular dynamics simulations of a Janus colloid with a planar-anchoring patch on the upstream side and a perpendicular-anchoring patch on the downstream side. The planar patch is smaller than the perpendicular one, although the transition between the different patches is rather smooth.

Figure 30(a) shows that for the system at rest ($\mathcal{E} = 0$) a ring defect topology arises around the equator. This is due to the fact that the patch with perpendicular anchoring covers most of the colloid's surface. However, at the smaller patch with planar anchoring a Boojum defect topology comparable to the defect for the homogeneous colloid with planar anchoring arises. Therefore, this defect topology corresponds to a *Boojum ring* [67]. This is also indicated by the low values of $S(\boldsymbol{r})$ at the north and south pole as well as on the

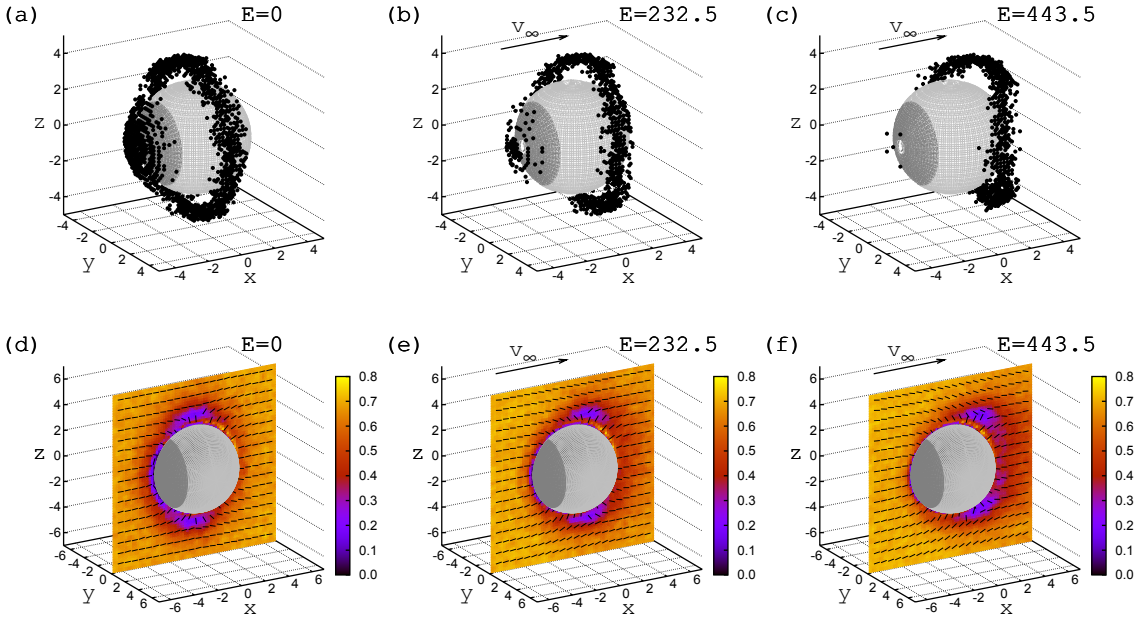


Figure 30: (a)-(c) A three dimensional representation of the defect structures ($S(\boldsymbol{r}) \leq 0.2$) around a Janus colloid. (d)-(f) Cross-section along the $x$-$z$ plane of the local nematic order parameter $S(\boldsymbol{r})$, where the color indicates the magnitude of $S(\boldsymbol{r})$, as well as the local director $\hat{\boldsymbol{n}}(\boldsymbol{r})$ represented by a black line. Plots are generated for different Ericksen numbers $\mathcal{E}$ for a colloid favoring planar anchoring (dark gray) on the upstream side and perpendicular anchoring (gray) on the downstream side and the black arrow indicates the direction of the streaming velocity $v_\infty$.

upstream side of the colloid [see Fig. 30(d)]. On the north and south pole the global director field is perturbed, which is indicated by the perpendicular orientation of $\hat{\boldsymbol{n}}(\boldsymbol{r})$ with respect to the colloid's surface. On the other hand, $\hat{\boldsymbol{n}}(\boldsymbol{r})$ is oriented planar with respect to the colloid surface on the upstream side of the colloid and therefore the global director field is perturbed here as well.

For increasing values of $\mathcal{E}$ one can see the ring defect structure moves downstream [see Figs. 30(b) and (c)]. This is equivalent to the configuration described above for the homogeneous colloid with perpendicular anchoring. Figures 30(e) and (f) confirm this observation. The region of low nematic order is moving downstream. However, the defect structure on the upstream side of the colloid is completely destroyed for high values of $\mathcal{E}$ [see Fig. 30(c)]. This effect can also be observed in the rapid increase of $S(\boldsymbol{r})$ [see Figs. 30(e) and (f)]. The destruction of the point defect structure is due to the fact that molecules are pushed out of the rather small patch favoring planar anchoring by the strong flow applied to the system.

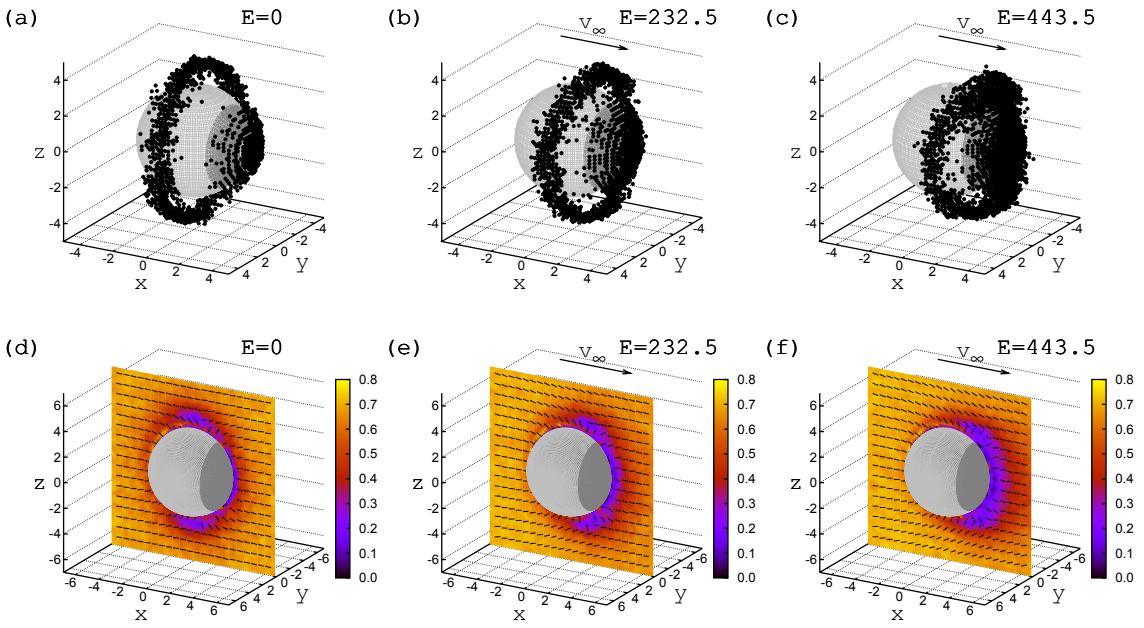


Figure 31: As Fig. 12 but for a Janus colloid favoring perpendicular anchoring (gray) on the upstream and planar anchoring (dark gray) on the downstream side.

We note that if the Janus colloid is reversed, and therefore exhibits the planar patch in the downstream direction, the Boojum defect grows in size as $\mathcal{E}$ increases. At the same time the Saturn ring deforms into a stomal defect and slowly merges with the growing Boojum lobe [see Fig. 31].

## 5.9 Hydrodynamic cavitation of anisotropic fluids

Hydrodynamic flow in a nematic liquid crystal has a strong impact on the defect topologies within the fluid. At even larger flow speeds (larger $\mathcal{E}$) than the ones presented in Tab. 1, another interesting flow-induced phenomenon can be observed: the inception and growth of cavitation. Interestingly, cavitation in a nematic liquid crystal occurs still within the laminar flow regime at rather low $\mathcal{R}$ compared to isotropic fluids such as water. In the following we will present the first in depth study of hydrodynamic cavitation in an anisotropic fluid with nonequilibrium molecular dynamics simulations. We follow the same simulation protocol already introduced in Sec. 5.1. However, in order to make our results comparable with recent microfluidic experiments [see App. C and Ref. [2]] we have replaced the colloidal particle with a cylindrical pillar and imposed homeotropic anchoring at the discrete walls [see Eq. 3.3]. Figure 32 shows a sketch of the simulation cell.

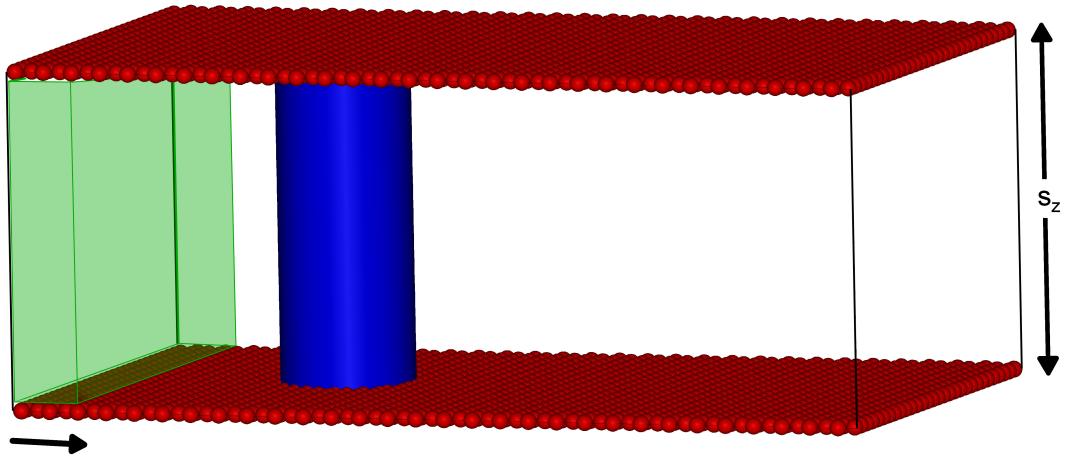


Figure 32: Sketch of the empty simulation cell with the discrete walls and a cylindrical pillar. The green shaded area marks where the driving force $F_e$ is applied [see Sec. 4.7].

The length scales accessible to molecular dynamics simulations of liquid crystals are still too small to study the cavitation bubble at the micron scale, as in experiments [see App. C], due to limitations in computer performance. The accessible molecular dynamics length scales do, however, give us access to the early stages of the cavitation process and to structural information not easily accessible with phenomenological theories of liquid crystals.

## 5.10 Local density

To characterize the onset and evolution of cavitation within the liquid crystal fluid we present in Fig. 33(a)-(c) maps of the local density [see Eq. 1.6] in a $x$-$y$ cross section of the system. For the system at rest, that is, without flow, the density is homogeneous throughout the system (not shown here). This is only disturbed by well-known layering effects close to the cylindrical pillar. For moderate flow conditions the density remains homogeneous across the system [see Fig. 33(a)]. However, when reaching very strong flow, starting at $\mathcal{E} \simeq 897$, the density across the system starts to change. More specifically, a drop in density in the wake of the pillar is observed [see Fig. 33(b)]. This area exhibits the density of a gas and therefore indicates the phenomenon of hydrodynamic cavitation. The size of the cavitation increases further with higher Ericksen numbers.

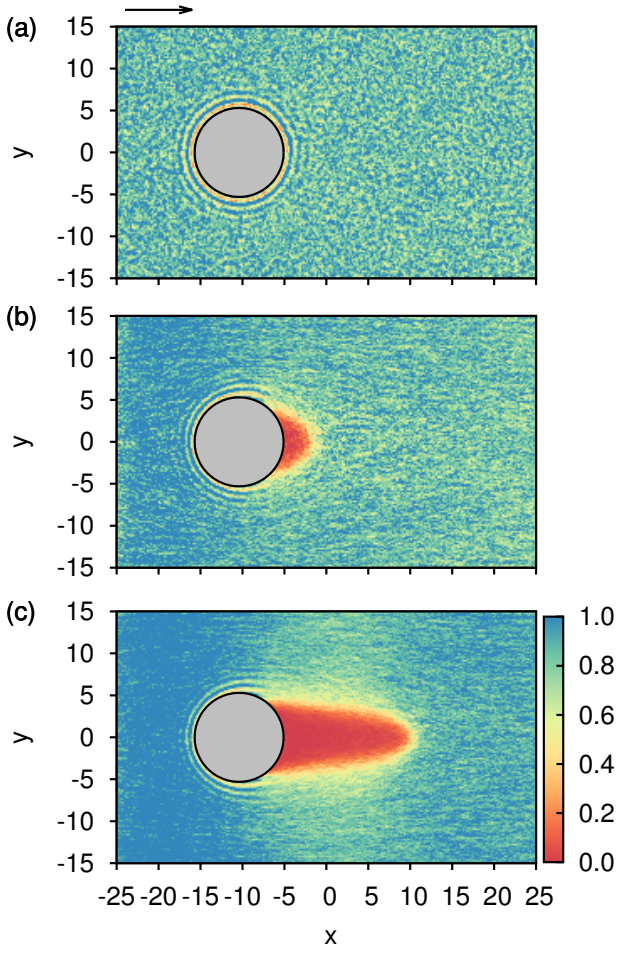


Figure 33: (a)-(c) Maps of the magnitude of local density in the $x$-$y$ plane located at $z = 0$ [see attached color bar]. The circle represents the cylindrical pillar and the arrow above each column indicates the direction of flow. (a) $\mathcal{E} \simeq 65$, (b) $\mathcal{E} \simeq 897$ and (c) $\mathcal{E} \simeq 1374$.

Figure 33(c) shows a well developed cavitation domain at $\mathcal{E} \simeq 1374$. The cavitation grows then at a slower pace than at low values of $\mathcal{E}$, and at $\mathcal{E} \simeq 1586$ reaches a maximum in size and does not grow further.

## 5.11 Local pressure

To gain insight into the development of cavitation we investigate the local pressure throughout the system. Figures 34(a)-(c) illustrate maps of the local pressure in a $x$-$y$ cross section of the system. The local pressure can be obtained rewriting Eq. 4.109 in a local form

$$\mathbf{P}(\boldsymbol{r}) = \frac{m}{V} \left\langle \left[ \sum_{i=1}^{N-1} \left( (\boldsymbol{v}_i - \boldsymbol{v}) \otimes (\boldsymbol{v}_i - \boldsymbol{v}) + \sum_{j=i+1}^{N} \boldsymbol{r}_{ij} \otimes \boldsymbol{F}_{ij} \right) \right] \delta(\boldsymbol{r}_i - \boldsymbol{r}) \right\rangle . \tag{5.118}$$

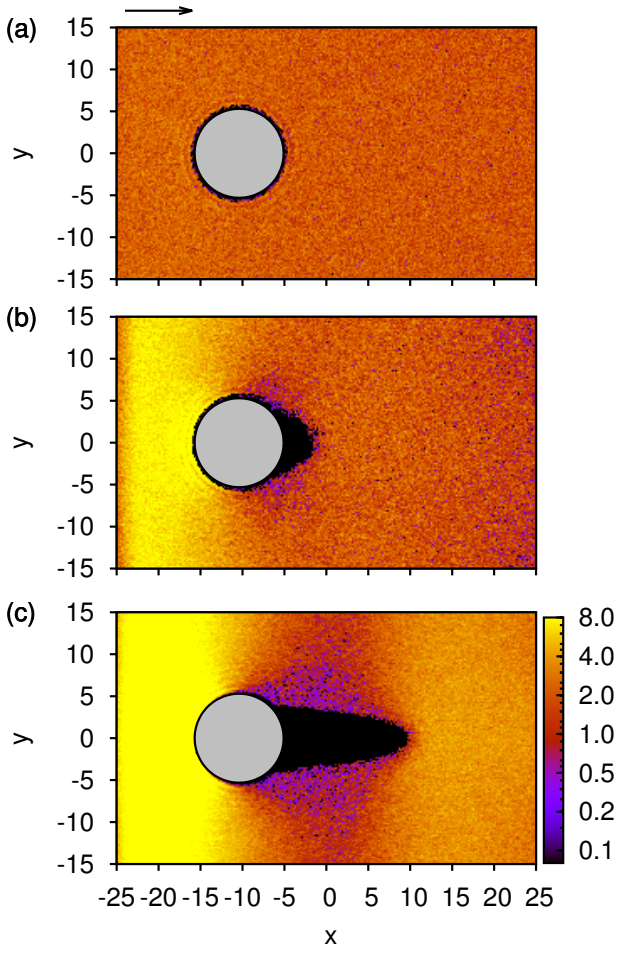


Figure 34: same as Fig. 33 but for the local pressure.

The system at rest exhibits a homogeneous local pressure, as one would expect (not shown here). From the map in Fig. 34(a) it is clear that this applies as well for small Ericksen numbers $\mathcal{E} \simeq 65$. However, for $\mathcal{E} \simeq 897$ at the onset of cavitation this situation changes drastically [see Fig. 34(b)]. On the upstream side of the pillar the local pressure exhibits very high values. This is due to the fact that the cylindrical pillar acts as an obstacle and takes up space. Therefore, the same amount of fluid is forced through a much smaller area compared to the rest of the system. Hence, locally the pressure builds up just before the cylindrical pillar. This is accompanied by a pressure drop on the downstream side behind the cylindrical pillar. After passing the constriction the fluid is now free to move and thus the local pressure decreases. This effect becomes even more drastic if flow is further increased as shown in Fig. 34(c). Notice that for a gas the contribution of the internal forces in Eq. (5.11) becomes negligible. Therefore, the pressure within the cavity is equivalent to the corresponding ideal gas pressure, $P = Nk_{\mathrm{B}}T/V$.

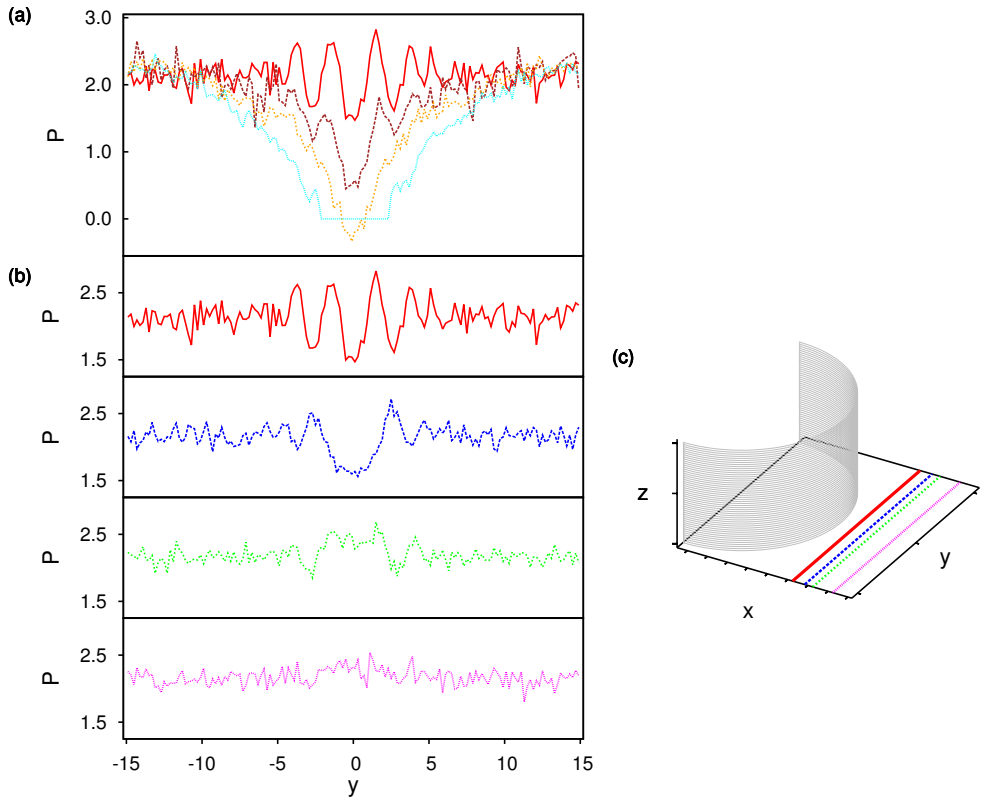


Figure 35: (a) Dependence of the local pressure at distance 0.7 behind the surface of the cylindrical pillar in the direction of flow along the $y$-axis for $\mathcal{E} \simeq 65$ (——), $\mathcal{E} \simeq 583$ (- - -), $\mathcal{E} \simeq 786$ (- · -), $\mathcal{E} \simeq 897$ (· · ·). (b) Same as (a) for $\mathcal{E} \simeq 65$ but for 0.7 (——), 1.3 (- - -), 1.7 (- · -), 2.7 (· · ·) behind the surface of the cylindrical pillar in the direction. (c) Sketch of the section behind the cylindrical pillar to illustrate the different positions of measuring the local pressure in (b).

To further explain the cavitation process we study the local pressure on a cross section in the $y$-$z$ plane at distance 0.7 behind the cylindrical pillar in the direction of flow. For reasons of symmetry and to improve statistics the values of the local pressure have been averaged along the $z$-axis and are presented along the $y$-axis in Figs. 35(a) and (b). To exclude confinement effects regions close to the planar substrates are excluded from the calculation.

Figure 35(a) focuses on the specific region where the cavitation is observed for strong flow, meaning high Ericksen numbers. For small flow velocities the local pressure behind the cylindrical pillar is on average constant along the $y$-axis. If flow is increased one can see from the plot in Fig. 35(a) that the local pressure starts decreasing behind the cylindrical pillar. At the threshold value for cavitation, $\mathcal{E} \simeq 786$, the local pressure attains negative values. Hence, molecules in this area are pushed out. This occurs just before a cavitation bubble develops. As soon as a cavitation bubble is visible ($\mathcal{E} \simeq 897$) the local pressure in that area is equal to the ideal gas pressure, for reasons explained above.

The oscillations visible in Fig. 35(a) for $\mathcal{E} \simeq 65$ are due to the layering effects [150, 151] of the molecules close to the pillar. This leads to changes in pressure in this region located at the center of the $y$-axis. If the local pressure is measured further away from the surface of the cylindrical pillar layering effects become less prominent and the minimum in local pressure at $y = 0$ vanishes [see Fig. 35(b)]. From a molecular point of view the local pressure oscillations close to the surface of the cylindrical pillar support the nucleation of a cavitation bubble. This is consistent with the fact that hydrodynamic cavitation requires a nucleation site such as a surface.

## 5.12 Local velocity

Figures 36(a)-(c) show maps of the local velocity in $x$-direction in a $x$-$y$ cross section of the system. For the system at rest there is no preferred direction of motion of the molecules (not shown here). Hence, the local velocity is on average zero across the entire system. At small flows, $\mathcal{E} \simeq 65$, the local velocity is still rather low [see Fig. 36(a)]. This can also be seen from the random orientations of the arrows representing the direction of flow in Fig. 36(a). At the onset of cavitation, $\mathcal{E} \simeq 897$, there is a clear net flow present [see Fig. 36(b)]. Additionally, Fig. 36(b) reveals that the local velocity in front of and behind the cylindrical pillar in the direction of flow is much lower than in the areas next to the pillar. This becomes even more evident from Fig. 36(c) where $\mathcal{E} \simeq 1374$ and the cavitation is much more developed. The local convective velocity is set to zero in the cavitation area due to the lack of reasonable statistics in the gaseous phase.

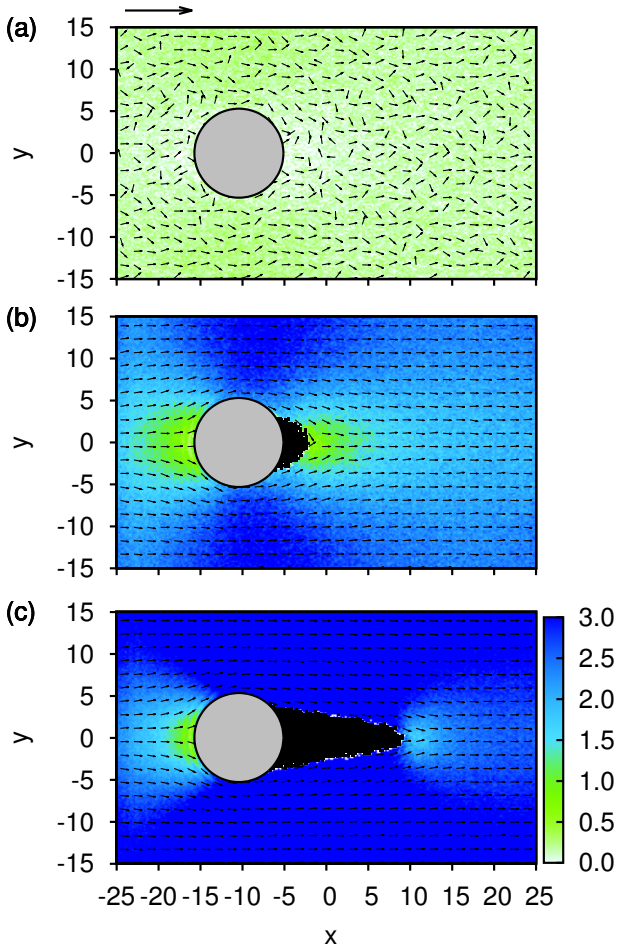


Figure 36: (a)-(c) Maps of the magnitude of local velocity in the $x$-$y$ plane located at $z = 0$ [see attached color bar]. The circle represents the cylindrical pillar and the arrow above each column indicates the direction of flow. (a) $\mathcal{E} \simeq 65$, (b) $\mathcal{E} \simeq 897$ and (c) $\mathcal{E} \simeq 1374$. The small arrows in the maps give the local direction of flow.

## 5.13 Cavitation volume

To gain further insight into the evolution of the cavitation and to characterize the cavitation bubble we calculate its volume. From the density calculations in Fig. 33(a)-(c) we can estimate the volume $V_c$ by adding up the volume of all cubes for which the local density $\rho_l \leq 0.15$. In addition to the liquid crystal system described so far we have performed additional molecular dynamics simulations for the same liquid crystal model in the isotropic phase ($T = 1.10$). The geometry of the microfluidic setup remains unchanged. The comparison of these two fluids will shed light on the influence of orientational ordering in the cavitation process.

Figure 37 shows how the volume $V_c$ of the cavitation bubble depends on the Reynolds

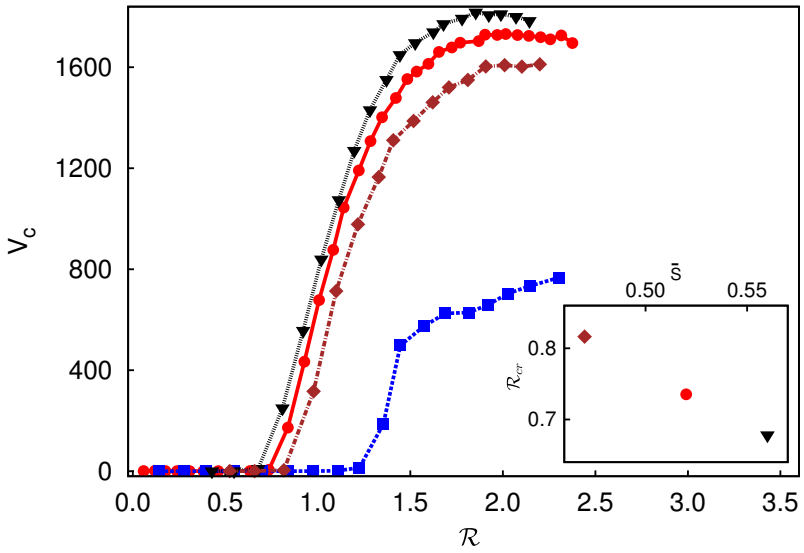


Figure 37: Cavitation volume $V_c$ against Reynolds number $\mathcal{R}$ for the nematic liquid crystal at $T = 0.88$ (▼), at $T = 0.90$ (●), and at $T = 0.92$ (♦), and for an isotropic liquid crystal (■). The inset shows the critical Reynolds number $\mathcal{R}_{cr}$ against the average nematic order parameter $\bar{S}$.

number $\mathcal{R}$, where $\mathcal{R}_{cr}$ denotes the cavitation inception. The major difference between the two systems is their viscosity $\eta$. The nematic liquid crystal ($\eta \simeq 37$) is more viscous than the isotropic liquid crystal ($\eta \simeq 21$). From the definition of $\mathcal{R}$ then follows that the nematic liquid crystal cavitates at lower critical Reynolds number $\mathcal{R}_{cr}$ than the isotropic liquid crystal. That fluids with lower viscosity require a larger $\mathcal{R}_{cr}$ to cavitate is consistent with microfluidic experimental observations [see App. C] that de-ionized water flowing at the same $\mathcal{R}$ as the liquid crystal did not exhibit cavitation. Furthermore, microfluidic experiments with de-ionized water by Mishra *et al.* [77–79] require a much larger $\mathcal{R}_{cr}$ to cavitate.

For both nematic and isotropic liquid crystals we observe a steep growth of the cavitation bubble after its formation followed by a saturation to a plateau. We have verified that the height of the saturation plateau is due to the finite size of the simulation box and therefore is system-size dependent. Notice also that the plateau value of the cavitation bubble depends on the nature of the fluid. We ascribe this behavior to the structural differences, e.g., ordering in the nematic liquid crystal, among the two fluids.

Figure 37 shows additionally the cavitation process for the nematic liquid crystal at $T = 0.88$ and $T = 0.92$, which exhibit a higher ($\eta \simeq 40$) and lower ($\eta \simeq 34$) viscosity, respectively, than what we considered above. One can see that the qualitative behavior is retained but there are small quantitative differences in growth and saturation of the cavitation bubble: the lower the temperature, and hence the higher the viscosity, the larger is the volume of the bubble. However, also the nematic order is different from the

nematic liquid crystal at $T = 0.90$. The inset of Fig. 37 shows the dependence of $\mathcal{R}_{cr}$ on the average global nematic order parameter $\bar{S}$. For values of $\bar{S}$ in the nematic phase the critical Reynolds number $\mathcal{R}_{cr}$ decreases linearly with $\bar{S}$, that is, cavitation is enhanced by stronger nematic alignment. This qualitative measurement could be a first step towards understanding the influence of long range ordering in high speed microfluidic systems.

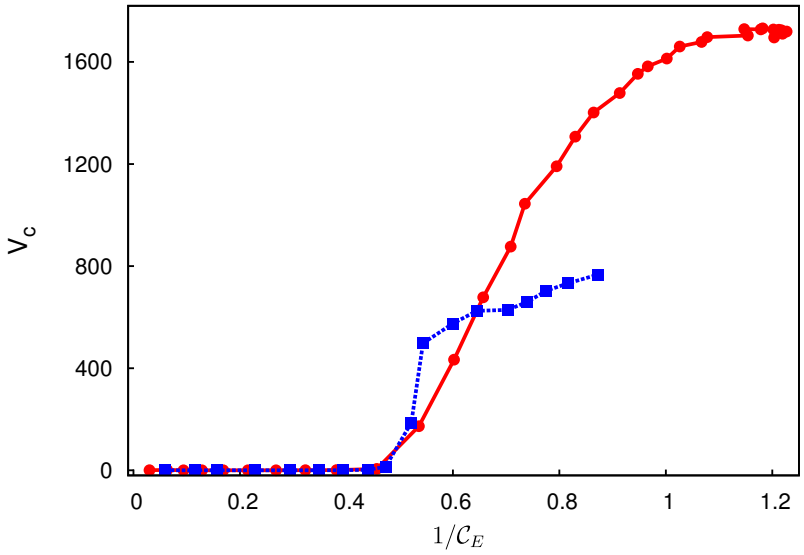


Figure 38: Dependence of the cavitation volume $V_c$ on the inverse Euler number $\mathcal{C}_{\mathrm{E}}^{-1}$ for the nematic liquid crystal (●), and isotropic liquid crystal (■)).

It might be more suitable to use a dimensionless number which is independent of the viscosity of the model system. Figure 38 shows the cavitation volume $V_c$ in terms of the inverse Euler number $\mathcal{C}_{\mathrm{E}}$ [see Sec. 2.5]. One can see very nicely that the ratio between the pressure gradient and the kinetic energy per volume is decisive for the development of a cavitation bubble. Independent of the model system cavitation occurs at the same Euler number $\mathcal{C}_{\mathrm{E}}$. Cavitation first occurs in the experiments [see App. C] for $\mathcal{C}_{\mathrm{E}} \approx 0.5$.

## 5.14 Local nematic order

Figure 39 shows maps of the magnitude of the local nematic order parameter for the liquid crystal in the nematic phase. The homeotropic anchoring at the substrates and the cylindrical pillar causes the director field to bend in regions close to the surface of the cylindrical pillar. At the intersections of substrate and pillar defect topologies arise, symmetrically placed at the top and bottom walls [see Fig. 39(a)]. The defects are due to the conflict caused by the homeotropic anchoring at the pillar and the substrate. Thus, two separate loops form around the pillar. This is comparable to the defect topology in Fig. 4(a) of Ref. [2] obtained from microfluidic experiments.

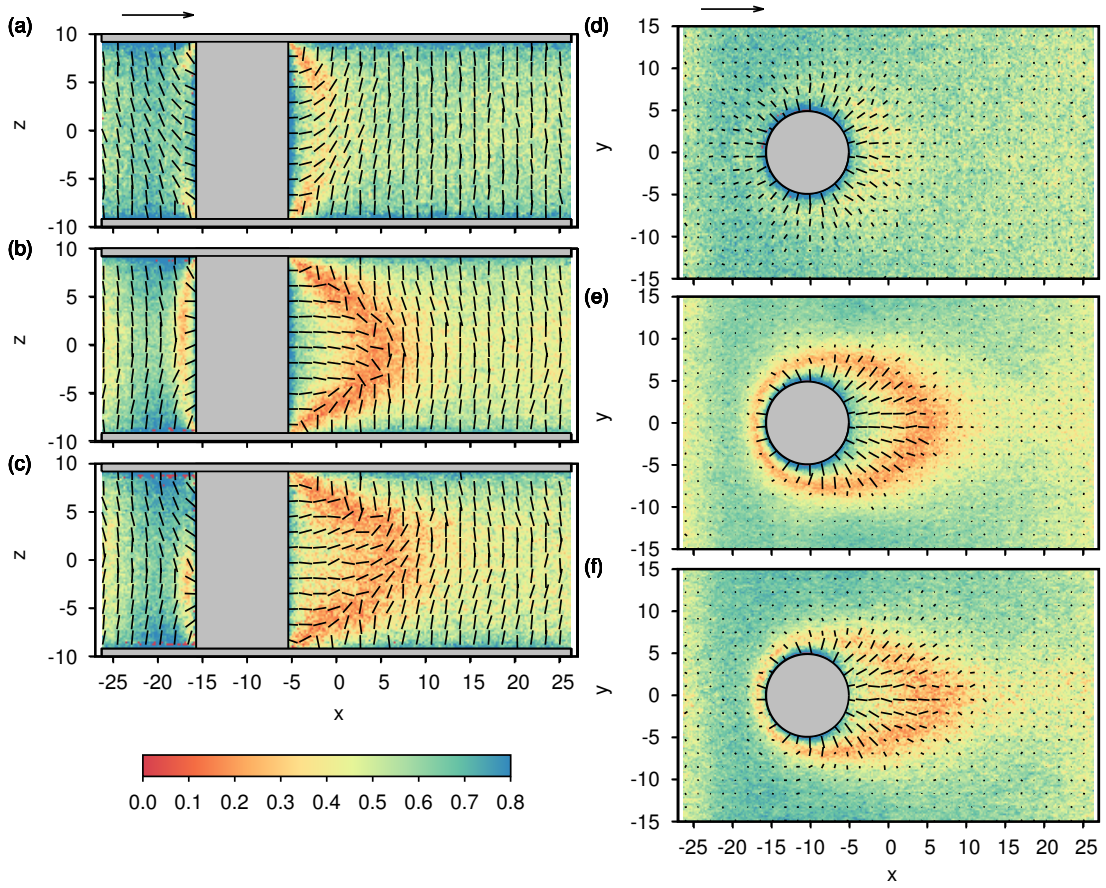


Figure 39: (a)-(c) Maps of the magnitude of local nematic order in the $x$-$z$ plane located at $y = 0$ (see attached color bar). The cylindrical gray area represents the cylindrical pillar and the arrow above each plot indicates the direction of flow. Small dashes in the maps represent the local director field. The length of a dash represents its three-dimensional orientation: shorter dashes have an orientation closer to the normal to the plane of the map. (a) $\mathcal{E} \simeq 130$, (b) $\mathcal{E} \simeq 675$ and (c) $\mathcal{E} \simeq 786$. (d)-(f) Same as (a)-(c) but in the $x$-$y$ plane located at $z = 0$.

From Fig. 39(d) it is evident that at the $x$-$y$-mid-plane, located at $z = 0$, no defect is visible. The director field remains stable for small Ericksen numbers. However, for $\mathcal{E} \geq 675$ a single loop around the pillar stabilizes in the $x$-$y$-mid-plane. The loop is deformed and extended towards the downstream direction along with the flow [see Figs. 39 (b) and (e)]. Additionally, there is a growing region of flow alignment behind the cylindrical pillar in the downstream direction. Again the director field is very similar to the experiments [see Fig. 4(c) of Ref. [2]]. Upon increasing Ericksen number one can see from see Fig. 39 (c) that the loop becomes more pronounced at the $x$-$y$-mid-plane in front of the pillar. Moreover, the loop is stretched further towards the downstream direction. However, the overall shape of the defect topology, especially behind the pillar in downstream direction, is increasingly smeared and blurred [see Fig. 39 (f)]. One can argue that the loop becomes unstable like

in the experiments [see Fig. 4(d) of Ref. [2]]. In our simulations it was not possible to make further observations on this matter because for higher Ericksen numbers cavitation occurs behind the pillar in the downstream direction.

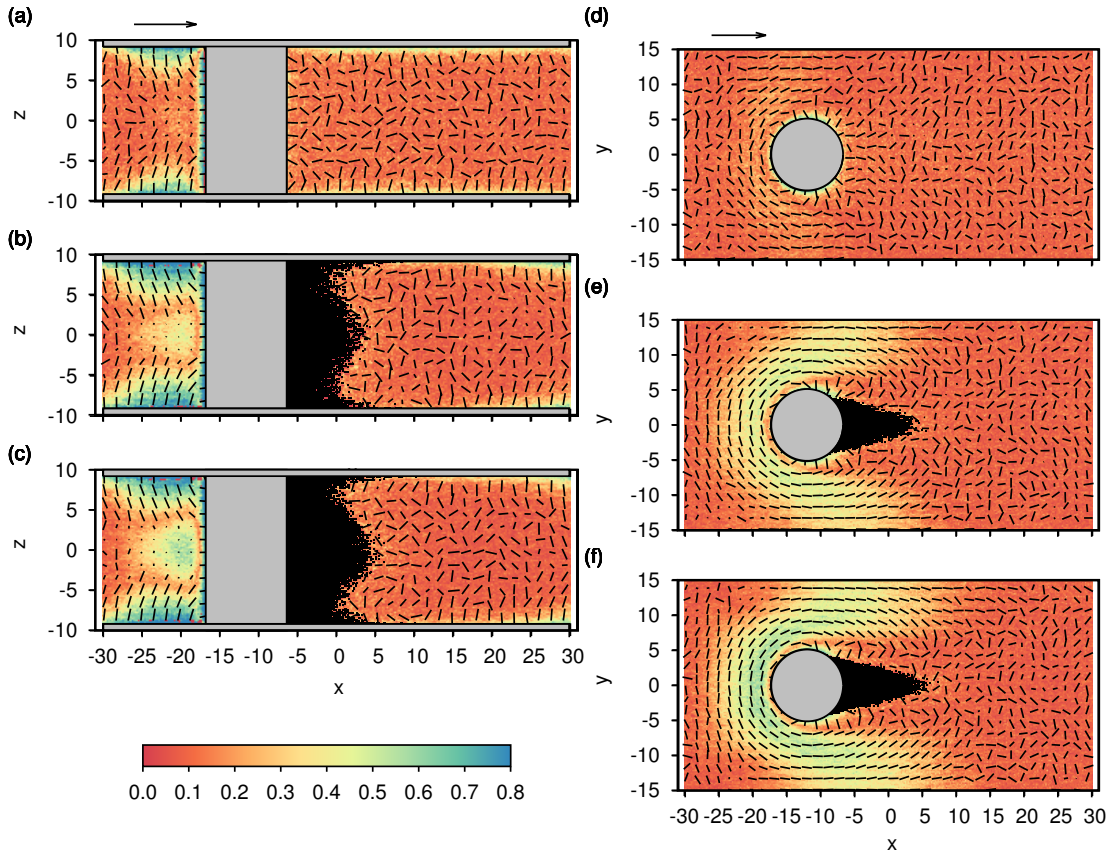


Figure 40: Same as Fig. 39 but for the isotropic phase ($T = 1.10$). (a) $F_e = 1.80$, (b) $F_e = 3.60$ and (c) $F_e = 4.80$.

Figure 40 shows maps of the magnitude of the local nematic order parameter for the liquid crystal in the isotropic phase ($T = 1.10$). For the isotropic phase it is not straightforward to obtain $\mathcal{E}$ because the elastic constant $K$ cannot be calculated in the same fashion [see Sec. 1.8]. Therefore we refer to the driving force $F_e$ in order to classify the strength of the flow [see Tab. 1]. The system at rest exhibits low nematic order and a disordered director field throughout the system, characteristic for the isotropic phase (not shown here). This remains true even under flow for a wide range of the driving force $F_e$. However, at $F_e \geq 1.80$ the nematic order in front of the pillar increases and the local directors align [see Figs. 40(a) and (d)]. As one can see in Figs. 40 (b) and (e) as well as (c) and (f) at even higher $F_e$ nematic order continues to rise and a nematic phase develops in a horseshoe-shaped area around the cylindrical pillar. Prost and de Gennes [152] proposed that flow can restore the anisotropy within a liquid crystal. Hence, a phase transition

from an isotropic to a nematic phase occurs. Our simulations support this idea although the phase transition seems mainly pressure driven. The location of the embedded nematic phase is correlated with the strong increase in local pressure in this area. Interestingly, the director field tends to be aligned more parallel to the velocity field rather than according to the homeotropic anchoring at the substrates and at the cylindrical pillar [see Figs. 36(b) and (c)]. Hence, the nematic region is somewhat flow-aligned [see Figs. 40 (e) and (f)].

# 6 Conclusions and Outlook

## 6.1 Effects of flow on topological defects

We study the defect topologies that arise around a homogeneous colloid, with planar or perpendicular anchoring, dispersed in a nematic liquid crystal. This leads to the well known Boojum defect and Saturn ring defect. We focus on the effect of hydrodynamic flow on these defect structures. The flow pertains to the laminar flow regime, meaning low Reynolds numbers. However, the regime of Ericksen numbers is rather high. Thus, the system of interest is dominated by viscous over elastic forces.

In our calculations we find that for our model system the elastic constants in the Frank free energy are equal within statistical precision. This is because the anisotropy of our liquid-crystal model stems from the interaction rather than the elongated shape of its molecules. The liquid-crystal molecules have a rather small aspect ratio. Therefore, the bend configuration is energetically roughly equal to the splay and twist configuration for liquid-crystal molecules of nearly spherical shape.

We employ nonequilibrium molecular dynamics simulations to study the evolution of topological defects under flow. In order to obtain meaningful results we employ a novel Galilean-invariant thermostat [66]. The thermostat conserves momentum locally and is completely deterministic which makes it well suited for computational studies.

The question of the direction of movement of defect topologies under flow conditions is unsettled throughout the literature and has been tackled by various theoretical approaches [59–64]. Our extensive nonequilibrium molecular dynamics simulation predict a downstream movement of all defect topologies along with the direction of flow, which is in agreement with the only available experimental study [1]. We find that the upstream lobe of a Boojum defect is swept away downstream, while the downstream lobe grows in size with increasing flow. The Saturn ring defect is convected downstream and deformed into a stomal defect. Again, this agrees very nicely with experimental observations [1].

In more detail we focus on ring-like defect structures around a homogeneous colloid. Hence, we study Saturn ring defects of different size under flow conditions quantitatively. We pay particular attention to the interaction range between liquid-crystal molecules and the colloidal particle. Generally speaking, the length of the ring-shaped disinclination line increases with increasing interaction range. The length of the disinclination line can be extracted from suitable projections of the simulation data.

The position of the ring defect depends strongly on the strength of the flow. If the flow is turned on defects move downstream while maintaining their distance from the colloid's surface. Thus, the disclination rings shrink. Our simple geometric analysis enables us to predict the transition from a Saturn ring defect to a hedgehog defect due

to flow. We estimate Reynolds and Ericksen numbers for the transition. Although the estimated Ericksen numbers might be in the scope of computer simulations our calculations show that for small colloids a hedgehog defect is very difficult to obtain. One would need to inject a lot more energy into to the system. Hence, for colloids on the nanometer scale the Saturn ring defect is energetically very stable.

Furthermore, the curvature of the ring defect also depends on the strength of the flow. In the immediate vicinity of the colloid the velocity field becomes rather inhomogeneous. This is due to the influence of the substrates. The difference in velocities leads to a difference in the amount of deflection of the defect around the colloid. Thus, the ring defect is deformed compared with its equilibrium shape. The deformation of the Saturn ring defect due to flow is in very good agreement with experimental data [1].

Our simulations suggest that the elastic deformations of the ring-shaped defects depend on the interaction range between liquid-crystal molecules and colloid as well. Smaller ring defects are less deformed due to the fact that their curvature is already large and more energy would be necessary to further bend the ring defect. Whereas bigger ring defects are more likely to experience an elastic deformation of the ring shape. The deformation can be referred to as elastic because its length scale is much bigger than the molecular scale.

Additionally, we present the first study of defect topologies arising around a Janus colloid under hydrodynamic flow. Our simulations show that a Boojum defect can be destroyed when facing the upstream direction. Furthermore, the Saturn ring defect is deformed into a stomal defect comparable to the singly Saturn ring defect for a homogeneous colloid.

The question of the direction of movement of the defect topologies under hydrodynamic flow seems settled. Additionally, the change in shape of defect topologies due to flow is well examined. However, further investigations quantifying the elastic response of defect topologies to hydrodynamic flow could complete the physical picture. Our simulations indicate elastic behavior of defect topologies and linking those findings to earlier theoretical studies [147, 149, 153] might be of great value. Furthermore, the examination of more complex defect structures under flow could be intriguing. Simulations could involve either more colloidal particles or a more complicated host phase, such as a chiral liquid crystal.

## 6.2 Hydrodynamic cavitation of anisotropic fluids

Utilizing similar nonequilibrium molecular dynamics simulations, but exploring higher Ericksen numbers, we study hydrodynamic cavitation of anisotropic fluids. However, simulations are still situated in the laminar flow regime, meaning low Reynolds numbers. We investigate the physical foundations of cavitation inception and growth of a nematic liquid crystal flowing past a cylindrical pillar. Additionally, we compare our results with the corresponding isotropic liquid crystal. Our simulations are in agreement with recent microfluidic experiments [see App. C].

Through measurements of the local density we are able to quantitatively capture the inception and evolution of the cavitation bubble. We establish a critical Reynolds number to measure the threshold for cavitation inception. Interestingly, the critical Reynolds number for a nematic liquid crystal is up to 50% lower than in isotropic fluids.

Evidently, the cavitation inception of any fluid is strongly linked to its viscosity. However, our study suggests that structural properties of ordered fluids play a role as well. We find that the critical Reynolds number decreases approximately linear with the global nematic order parameter demonstrating that long range ordering has a quantitative effect on the cavitation inception. Measurements of the growth in cavitation volume reveal that the qualitative behavior of isotropic liquid crystals is similar to the one of anisotropic fluids, for example, the rate of growth. However, the size of the cavitation domain at large Ericksen numbers is markedly different. This further adds credibility to the assumption that structural differences, such as long range order, affect the growth of cavities due to hydrodynamic flow.

Measuring the local pressure is ideal to clarify the physical basis of the cavitation inception. In the simulation cell an area restriction, such as a cylindrical pillar, causes a local drop in pressure. If the local pressure reaches negative values the fluid begins to cavitate in this particular area. Furthermore, focusing on the designated position of cavitation inception behind the cylindrical pillar reveals the molecular origin. Well-known layering effects on the surface of the cylindrical pillar cause local pressure oscillations. Hence, the formation of a cavitation bubble is favored, or even nucleated, through a minimum in local pressure caused by these oscillations. Thus, hydrodynamic cavitation is always favored in areas where the fluid is in contact with a surface.

Furthermore, we find very good agreement with earlier microfluidic experiments [2] at smaller Ericksen numbers before cavitation initiates. Our nonequilibrium molecular dynamics simulations are able to reproduce the structural changes in the nematic liquid crystal at different Ericksen numbers.

Our study is a first step towards understanding cavitation in anisotropic fluids. Further studies could follow up on these findings and explore long range order as a control parameter for driving cavitation in detail. Furthermore, exploring different geometries

could be insightful. In order to achieve this one could either vary the design of the simulation cell or the shape of the restriction. In general, hydrodynamic flow in anisotropic fluids at high Ericksen numbers is rather unexplored and opens a vast range of possibilities for new research topics.

# 7 Appendices

## A Free energy

In this appendix we derive the first order expression of the free energy in a perturbative scheme, where the range of the fluid-colloid interaction is taken as the expansion parameter. Thermodynamic stability of the system can be cast in terms of its free energy

$$\mathcal{F} = -\beta^{-1} \ln \mathcal{Q}, \tag{A.119}$$

where $\beta \equiv 1/k_{\mathrm{B}}T$ ($k_{\mathrm{B}}$ is Boltzmann's constant and $T$ the temperature), and $\mathcal{Q}$ is the partition function of the canonical ensemble [134]. For our system, $\mathcal{Q}$ may be cast as [123]

$$\mathcal{Q} = \frac{1}{2^N N!} \left( \frac{\mathcal{I}}{m} \right)^N \frac{1}{\Lambda^{5N}} \mathcal{Z}. \tag{A.120}$$

In Eq. A.120, the factor $1/\left(2^N N!\right)$ takes account of the head-tail symmetry of the molecules in the host phase [see Sec. 3.2] and their indistinguishability, $\mathcal{I}$ and $m$ are their moment of inertia and mass, respectively, $\Lambda = \sqrt{\beta h^2/2\pi m}$ is the thermal de Broglie wavelength ($h$ Planck's constant) and $\mathcal{Z}$ the configurational integral

$$\mathcal{Z} = \iint \mathrm{d}\boldsymbol{R}\, \mathrm{d}\boldsymbol{\Omega} \exp\left[-\beta \Phi\left(\boldsymbol{R}, \boldsymbol{\Omega}\right)\right], \tag{A.121}$$

where we introduce shorthand notations $\boldsymbol{R} \equiv \{\boldsymbol{r}_1, \boldsymbol{r}_2, \ldots, \boldsymbol{r}_N\}$ and $\boldsymbol{\Omega} \equiv \{\omega_1, \omega_2, \ldots, \omega_N\}$.

To estimate $\beta\mathcal{F}$ we apply perturbation theory following ideas originally proposed by Zwanzig more than half a century ago [134, 154]. We split $\Phi$ into two contributions according to

$$\Phi = \Phi^{(0)} + \Phi^{(1)}\left(\lambda\right), \tag{A.122}$$

where the separation is made such that the configurational potential energy of a reference system $\Phi^{(0)}$ is independent of the inverse Debye screening length $\lambda$ of the fluid-substrate interaction whereas a perturbational contribution $\Phi^{(1)}$ is defined which depends on $\lambda$ explicitly.

A couple of comments apply at this stage. First, we remind ourselves that we seek to investigate the dependence of the free energy on the range of the fluid-colloid *attraction*. Second, to finally arrive at computationally tractable expressions the colloid needs to be present in some form already in the reference system. Hence, we cannot take $\Phi^{(0)} = \Phi_{\mathrm{ff}} + \Phi_{\mathrm{fs}}$ such that the *entire* fluid-colloid interaction is part of $\Phi^{(1)}$.

We could split $\varphi_{\mathrm{fc}}$ in Eq. 3.69 into repulsive and attractive parts and let repulsive interactions be included in $\Phi^{(0)}$ whereas attractive ones are accounted for by $\Phi^{(1)}$. How-

ever, this naive approach has a major drawback. Because $a_1$ in Eq. 3.70 depends on $\lambda$ so would $\Phi^{(0)}$ which contradicts Eq. A.122 and therefore this choice is unsuitable.

Fortunately, one realizes from the plot of $\varphi_{\mathrm{fc}}$ [see Fig.11] that over the range of $\lambda$'s relevant to our study, a variation of $\lambda$ mainly affects the range of fluid-colloid *attractions* whereas the steepness of the *repulsive* part of $\varphi_{\mathrm{fc}}$ depends only marginally on $\lambda$. Therefore, we replace $\varphi_{\mathrm{fc}}$ in Eq. 3.69 by

$$\varphi'_{\mathrm{fc}}\left(\boldsymbol{r}_i, \omega_i; r_0, \lambda\right) = \varphi_{\mathrm{hs}}\left(r_i; r_0\right) + \varphi_{\mathrm{fc}}\left(\boldsymbol{r}_i, \omega_i; r_0, \lambda\right), \tag{A.123}$$

where

$$\varphi_{\mathrm{hs}}\left(r_i; r_0\right) = \begin{cases} \infty, & r_i < r_0 + \sigma \\ 0, & r_i \geq r_0 + \sigma \end{cases} \tag{A.124}$$

is a purely repulsive hard-sphere fluid-colloid background potential. This choice permits us to introduce

$$\Phi^{(0)} = \Phi_{\mathrm{ff}} + \Phi_{\mathrm{fs}} + \sum_{i=1}^{N} \varphi_{\mathrm{hs}}\left(r_i; r_0\right), \tag{A.125}$$

whereas $\Phi^{(1)}\left(\lambda\right) = \Phi_{\mathrm{fc}}$ [see also Eqs. 3.59, 3.64, and 3.68]. Hence, $\Phi^{(0)}$ and $\Phi^{(1)}\left(\lambda\right)$ now comport with Eq. A.122. In Eq. A.124 we have chosen the *effective* hard-sphere radius $r_0+\sigma$ rather than the hard-core radius of the colloid because $r_0+\sigma$ is the same irrespective of $\lambda$ on account of Eqs. 3.70 and 3.71.

Within the framework of Zwanzig's perturbation theory [134, 154] it is then straightforward to show that

$$\mathcal{Z} = \mathcal{Z}^{(0)} \left\langle \exp\left[-\beta\Phi^{(1)}\left(\lambda\right)\right] \right\rangle_0, \tag{A.126}$$

where $\mathcal{Z}^{(0)}$ is the configuration integral associated with the reference system and $\langle \ldots \rangle_0$ is an average taken in the canonical ensemble over microstates generated in the reference system. By inserting this expression into Eq. A.121 it follows from Eqs. A.119-A.120 that $\mathcal{F}\left(\lambda\right) = \mathcal{F}^{(0)} + \mathcal{F}^{(1)}\left(\lambda\right)$, where the two contributions on the right-hand side are the free energies of the reference system and of the perturbation.

Expressing now $\mathcal{F}^{(1)}$ as a power series in terms of $\beta$ and expressing $\exp\left[-\beta\Phi^{(1)}\left(\lambda\right)\right]$ as a similar series in terms of $\beta\Phi^{(1)}$ we obtain a successively more complex approximation to $\mathcal{F}^{(1)}$ by comparing in both expansions terms of equal power in $\beta$. Here we will consider only the lowest order term proportional to $\beta$ itself for which

$$\mathcal{F}^{(1)}\left(\lambda\right) = \mathcal{F}\left(\lambda\right) - \mathcal{F}^{(0)} = \left\langle \Phi^{(1)}\left(\lambda\right) \right\rangle_0, \tag{A.127}$$

which can easily be computed in Monte Carlo simulations.

# B Monte Carlo simulations

To compute the perturbational free energy we employ Monte Carlo simulations. Monte Carlo is the preferred simulation technique because hard-core repulsive interactions [see Eq. A.123] are problematic in time-driven molecular dynamics simulations. Monte Carlo simulations employ a conventional Metropolis algorithm and are carried out in the canonical ensemble using precisely the same system sizes and other thermodynamic conditions as the ones employed in nonequilibrium molecular dynamics simulations [see Sec. 5.1]. The generation of a Markov chain of configurations is governed by $\Phi^{(0)}$. An estimate of $\mathcal{F}^{(1)}$ is then easily accessible by averaging $\Phi^{(1)}$ over this Markov chain. Ensemble averages have been taken over $5.0 \times 10^4$ Monte Carlo cycles. During a Monte Carlo cycle it is decided with equal probability whether to randomly displace the center of mass of a sequentially chosen molecule by a small amount or to rotate it by a small angle increment about a randomly chosen axis. Both processes are realized through a Metropolis algorithm [119].

# C Microfluidic experiments on hydrodynamic cavitation

Here we present results from microfluidic experiments which are complementary to the nonequilibrium molecular dynamics simulations on hydrodynamic cavitation in a nematic liquid crystal [see Sec. 5.9]. We will compare the experimental findings to the molecular dynamics simulations. Details regarding the materials and methods applied can be found in Ref. [155].

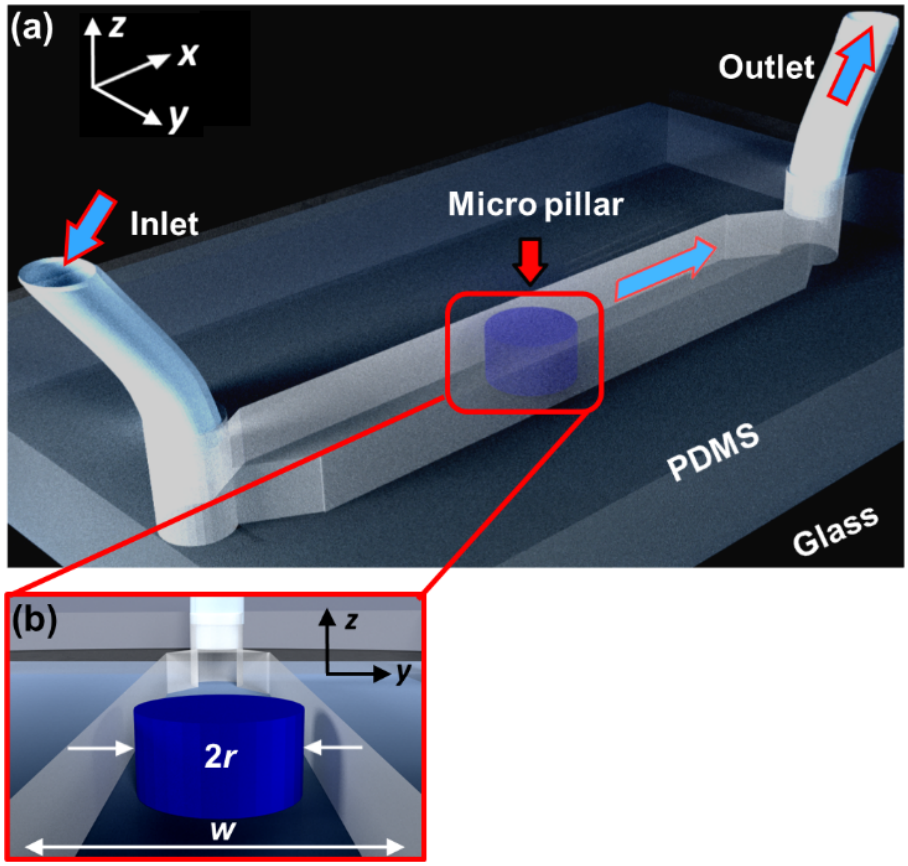


Figure C.1: Microfluidic confinement. (a) Microchannel with micron-sized cylindrical pillar fabricated using surface bonding of PDMS and glass components. The orthographic projection shows a linear channel of a rectangular cross-section with the integrated micropillar. $x$, $y$, and $z$ coordinates denote the flow direction of the nematic liquid crystal, the transverse direction of the channel (width), and the channel depth respectively. The blue arrow heads show the flow path. (b) Microchannel projection showing the cross-sectional view ($y$-$z$ plane) with $r$, $w$, and $d$ being the pillar radius, channel width and depth, respectively.

Microfluidic devices [see Fig. C.1], possessing homeotropic surface anchoring, were initially filled with 5CB in the isotropic state, and allowed to equilibrate to nematic phase at room temperature. Thereafter, the volume flow rate $Q$ ($0.01\ \mu\text{l/h} < Q < 20\ \mu\text{l/h}$) was

progressively increased to detect the first appearance of the microscopic cavitating domain. For a typical channel with dimensions, $w = 100$ $\mu$m, and $d = 15$ $\mu$m, the corresponding flow speed, $v$, within the microchannel varied between $\approx 2$ $\mu$m/s and 4 mm/s. Thus, for the nematic liquid crystal 5CB having bulk dynamic viscosity, $\eta \approx 50$ mPas [155], the characteristic Reynolds number $\mathcal{R} = \rho v l/\eta$ ranged between $10^{-6}$ and $10^{-3}$, which, from a hydrodynamic point of view, signifies the Stokes flow regime. Here, $\rho \approx 1025$ kg/m$^3$ is the material density, and $l = 4wd/2(w + d) \approx 26$ $\mu$m is the hydraulic diameter of the rectangular microchannel. The single elastic constant $K = 5.5$ pN for nematic 5CB. In the experiments, the corresponding values of the Ericksen number $\mathcal{E}$ ranged from $\approx 0.5$ to 850.

The first appearance of the microscopic cavitation domain, 5CB in vapor phase, was detected at $\mathcal{E} \approx 200$. Note that, as the streamlines of the flowing 5CB divide upon approaching the micropillar, both $\mathcal{E}$ and $\mathcal{R}$ first increase locally, reach maxima at the point of minimum separation between the pillar surface and the channel wall, and finally decrease back to their original values as the flows converge downstream of the pillar. The local velocity at the constriction in Fig. C.2(a) (minimum distance of 10 $\mu$m between the pillar surface and the channel wall) is calculated from the conservation of mass. With an average flow speed of 800 $\mu$m/s ($\mathcal{E} = 200$), the velocity reaches a maximum of 4000 $\mu$m/s at the constriction, which corresponds to $\mathcal{E} = 945$. This value is intriguingly close to $Er = 897$ found in the simulations. Notice, that the local Reynolds number still remains within the Stokes regime with a value of $Re_{loc} \approx 0.1$. These observations lead to the conclusion that despite the different length scales in experiment and simulation both are working under equivalent hydrodynamic conditions which is important because cavitation depends on the hydrodynamic conditions.

As shown in Fig. C.2(a), the vapor phase localizes at the hydrodynamic stagnation point downstream of the micron-sized pillar. Due to the high Ericksen number, the flowing nematic bulk is readily filled with singular topological defects [156]. When disclination lines are observed in white light, they scatter light and optically appear as dark lines. Here such disclination lines were observed in the bulk of the nematic liquid crystal flowing past the micron-scale obstacle using video microscopy. By means of image analysis technique one captures the minimum intensity from each frame acquired from the video, and average them over all the frames of the video. Thus, a time-averaged intensity map of the disclination lines flowing past the obstacle is obtained. This information was used as a proxy for the streamlines of the nematic flow, since disclinations - both singular and escaped structures - are stretched due to the viscous drag, and in general, appear as straight lines within the flow [157].

As an example, in Fig. C.2(c), the downstream hydrodynamic stagnation point is located from such a minimum intensity projection of the light scattered due to the flowing disclination lines, indicated by the red arrow head. Numerous, freely flowing disclinations

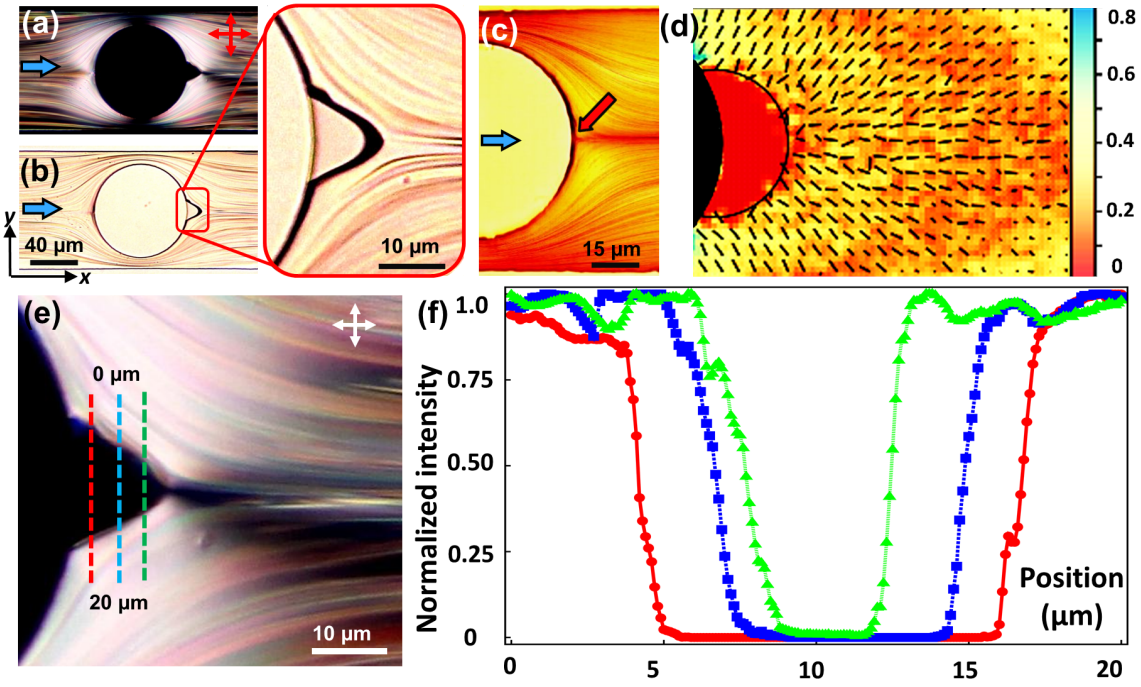


Figure C.2: Cavitation in nematic liquid crystal, 5CB, flowing past a micron-sized pillar. (a) Polarized optical microscopy and (b) white light micrograph show steady state cavitation domain. Right panel: Magnified projection of the cavitating domain. (c) Minimum intensity projection of the scattered light over time due to flowing disclination lines. The disclinations were used to trace the streamlines of the liquid crystal flow past the micropillar. The cavitating domain is locally stabilized at the hydrodynamic stagnation point (indicated by the red arrow head) downstream of the micron-sized pillar. For the micrographs shown here, the pillar diameter is $2r = 80$ $\mu$m, placed within a 100 $\mu$m wide and 15 $\mu$m deep microchannel. (d) Map of the local nematic order parameter in proximity of the cavitation domain obtained from molecular dynamics simulations (see attached color bar). The area of solid red color corresponding to vanishing nematic order represents the cavitation. Small dashes in the maps represent the local director field. The length of a dash represents its three-dimensional orientation: shorter dashes have an orientation closer to the normal to the plane of the map. (e) Magnified view of the cavitating domain observed between crossed polarizers. The intensity of the transmitted light (normalized by the maximum intensity) is measured along the dashed lines: red, blue and green, and plotted in (f). For each line, the maximum value of the normalized intensity (bright regions) is recorded outside the cavitation domain (bulk director is oriented at 45° relative to the polarizers). At the apex of the cavitation domain and further downstream, the director is oriented parallel to the flow direction which appears dark between the crossed polarizers. The gas filled cavitation domain also appears dark (minimum intensity) due to the total extinction of transmitted light.

- the director structure about each defect line corresponds to either $\pm 1/2$ or $\pm 1$ topological charge - spontaneously emerge at high Ericksen numbers [156], and follow the streamlines of the liquid crystal flow past the micropillar. The overall bulk director field is aligned due to the imposed flow field (nematic 5CB is a flow aligning liquid crystal). Between crossed polarizers [indicated by the double-headed crossed arrows in Fig. C.2], the cavitation domain has a dark visual appearance due to complete extinction of the transmitted white light as it passes first, through the polarizer, and then the analyzer. The interface between the vapor and liquid phases of 5CB are distinctly identified by visualizing the domain in white light [see Fig. C.2(b)]. No cavitation was observed due to flows with $\mathcal{E} < 200$. The flow-director interplay in this case agreed very well with those described previously by Sengupta *et al.* [2].

Figure C.2(d) shows a map of the local nematic order parameter in proximity of the cavitation domain obtained from molecular dynamics simulations. The molecular dynamics simulations predict homeotropic alignment at the fluid-vapor interface.

Figure C.2(e) presents a magnified view of the cavitating domain observed between crossed polarizers. When the intensity of the transmitted light (normalized by the maximum intensity) is plotted along three cross sections of the cavitation domain (red, blue and green dashed lines in Figure C.2(f)), one observes that the maximum value of the normalized intensity (bright regions) is located just outside the cavitation domain. These regions of maximum intensity correspond to the bulk director orientation of 45° relative to the polarizers. The director gradually bends along the flow direction, finally orients parallel to the flow direction, as observed closed to the apex of the cavitation domain and further downstream. This appears dark between crossed polarizers as the director is parallel to one of the polarizers. A minimum intensity is also observed within the cavitation domain due to the total extinction of the white light passing through the gas phase between crossed polarizers. The intermediate values of the normalized intensity at the cavitation interface suggest that the molecules are weakly homeotropically aligned at the interface, which is in agreement with the molecular dynamics simulations. Measurements on 5CB confirm that the molecules align homeotropically to the fluid-vapor interface [1, 158, 159]. Furthermore, it is known that liquid crystal molecules with strong dielectric anisotropy, such as 5CB, align homeotropically at the liquid crystal-air interface [160]. Therefore, the molecular dynamics simulations correctly capture this behavior which lends confidence to the predictions of the simulations about the underlying physics.

Flow of de-ionized water at the same Reynolds numbers did not result in cavitation, which suggests that the complex anisotropic nature of the nematic 5CB could underline the driving mechanism in the system.

Upon appearance, the volume of the cavitation domain increases over time, and typically within few hours ($4\text{ h} - 7\text{ h}$) of uninterrupted steady state flow of the nematic liquid crystal 5CB, saturates into a constant volume. Figures C.3(a) and (b) show POM

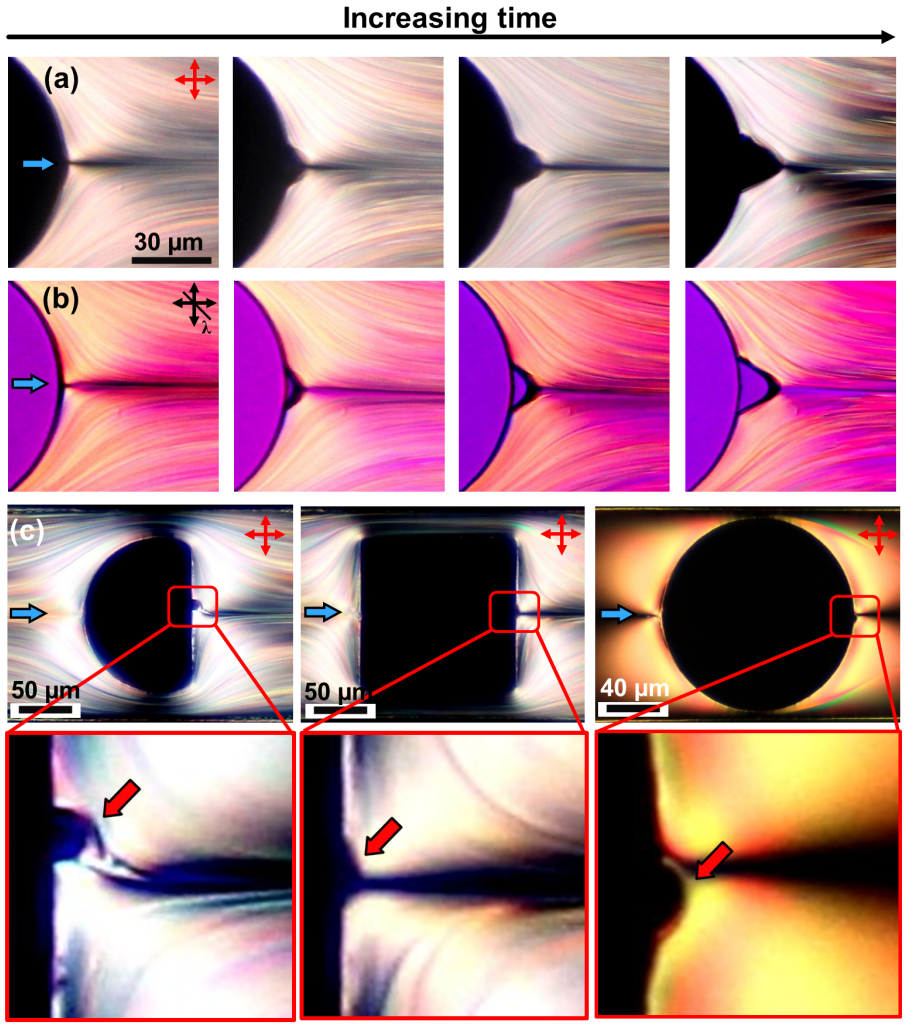


Figure C.3: Cavitation domain growth. (a) Polarized optical micrographs represent the growth of the cavitation volume over time. The total time elapsed is approximately 4 h. The minimum intensity regions (dark appearance) are observed either due to the extinction of the transmitted light as it passes through the vapor phase (in the cavitation domain), or through the bulk nematic phase aligned parallel to one of the polarizers. The two cases are distinguished using a $\lambda$-plate. (b) Introduction of the $\lambda$-plate confirms the absence of the nematic phase in the cavitation domain, and distinguishes it from the bulk nematic aligned parallel to the polarizer. (c) Cavitating domains were observed upon liquid crystal flow past different obstacle geometries: semi-circle (left) and square (middle); and at different channel depths (right, $d \approx 10$ $\mu$m). Shallow channels require high $\mathcal{E}$ numbers for cavitation to be triggered.

micrographs of a developing cavitating domain over time at $\mathcal{E} \approx 210$. The total elapsed time, from the first detection to saturation volume, is approximately 5 h. The duration to attain a steady state cavitation volume varied over multiple experiments, and, qualitatively, showed a dependence on the roughness of the pillar surface, and the vertical depth of the microchannel. For a given Ericksen number, the time taken to attain saturated domain volume was higher in shallow channels ($d < 12$ $\mu$m), compared to the deeper channels. However, once formed, the cavitation domain in a shallow channel was observed to be stable over longer times, possibly due to the pinning of the vapor-liquid interface at the top and bottom surfaces of the microchannel. The POM micrographs with $\lambda$-plate (Fig. C.3(b)) clearly show that the absence of the nematic phase within the cavitation domain, and outlines the boundary between the gas and liquid phases in the system. The emergence of the cavitating domain was reproducibly observed also at the downstream stagnation points of different obstacle geometries: semi-circle and square [see Fig. C.3(c)]. At very high Ericksen numbers, $\mathcal{E} > 500$, the domain volume shrinks, and is temporally unstable. While high flow speed (high $\mathcal{R}$) should favor the onset of cavitation, one can speculate that the resulting high shear at the vapor-liquid interface establishes a trade-off by disintegrating the saturated volume into minuscule bubbles, finally advecting them downstream.

# References


[1] S. Khullar, C. Zhou, and J. J. Feng. Dynamic evolution of topological defects around drops and bubbles rising in a nematic liquid crystal. *Phys. Rev. Lett.*, 99:237802, 2007.

[2] A. Sengupta, C. Pieper, J. Enderlein, C. Bahr, and S. Herminghaus. Flow of a nematogen past a cylindrical micro-pillar. *Soft Matter*, 9:1937, 2013.

[3] R. Virchow. Ueber das ausgebreitete vorkommen einer dem nervenmark analogen substanz in den thierischen geweben. *Virchows Arch.*, 6:562, 1854.

[4] C. Mettenheimer. Mikroskopische beobachtungen mit polarisiertem licht. *Corr. Blatt d. Vereins gem. Arb. z. Förderung d. wissenschatl. Heilkunde*, 24:331, 1857.

[5] O. Lehmann. *Über physikalische Isomerie.* Universität Straßburg, Straßburg, 1877.

[6] P. Planer. Notiz über das cholestearin. *Liebigs Ann. Chem.*, 118:25, 1861.

[7] W. Löbisch. unknown. *Ber. deutsch. chem. Ges.*, 5:513, 1872.

[8] B. Raymann. unknown. *Bull. Soc. Chim. Paris*, 47:898, 1887.

[9] F. Reinitzer. Beiträge zur kenntniss des cholesterins. *Monatsh. Chem.*, 9:421, 1888.

[10] O. Lehmann. über fliessende krystalle. *Z. Phys. Chem.*, 4:462, 1889.

[11] L. Gattermann and A. Ritschke. Ueber azoxyphenoläther. *Ber. Dtsch. Chem. Ges.*, 23:1738, 1890.

[12] D. Vorländer. Ueber krystallinisch-flüssige substanzen. *Ber. Dtsch. Chem. Ges.*, 39:803, 1906.

[13] E. Bose. Für und wider die emulsionsnatur der kristallinischen flüssigkeiten. *Phys. Zeit.*, 8:513, 1907.

[14] E. Bose. über viskositätsanomalien anisotroper flüssigkeiten im hydraulischen strömungszustande (ein experimentalbeitrag zur schwarmtheorie der kristallinen flüssigkeiten). *Phys. Zeit.*, 10:32, 1909.

[15] E. Bose. Zur theorie der anisotropen flüssigkeiten. *Phys. Zeit.*, 10:230, 1909.

[16] M. Born. über anisotrope flüssigkeiten. versuch einer theorie der flüssigen kristalle und des elektrischen kerr-effekts in flüssigkeiten. *Sitzungsber. Preuss. Akad Wiss.*, 30:614, 1916.

[17] G. Friedel. The mesomorphic states of matter. *Ann. Phys. (Paris)*, 18:273, 1922.

[18] C. W. Oseen. The theory of liquid crystals. *Trans. Faraday Soc.*, 29:883, 1933.

[19] F. C. Frank. I. liquid crystals. on the theory of liquid crystals. *Discuss. Faraday Soc.*, 25:19, 1958.

[20] V. Tsvetkov. On molecular order in the anisotropic liquid phase. *Acta Physicochim.*, 16:132, 1942.

[21] G. H.Brown and W. G. Shaw. The mesomorphic state-liquid crystals. *Chem. Rev.*, 57:1049, 1957.

[22] W. Maier and A. Saupe. Eine einfache molekulare theorie des nematischen kristallinflüssigen zustandes. *Z. Naturforsch.*, 13a:564, 1959.

[23] W. Maier and A. Saupe. Eine einfache molekular-statistische theorie der nematischen kristallinflüssigen phase. teil i. *Z. Naturforsch.*, 14a:882, 1959.

[24] W. Maier and A. Saupe. Eine einfache molekular-statistische theorie der nematischen kristallinflüssigen phase. teil ii. *Z. Naturforsch.*, 15a:287, 1960.

[25] H. Stark. Physics of colloidal dispersions in nematic liquid crystals. *Phys. Rep.*, 351:387, 2001.

[26] I. Muševič, M. Škarabot, U. Tkalec, M. Ravnik, and S. Žumer. Two-dimensional nematic colloidal crystals self-assembled by topological defects. *Science*, 313:954, 2006.

[27] P. J. Collings. *Liquid Crystals: nature's delicate phase of matter.* Princeton University Press, Princeton, 1990.

[28] P. J. Collings and M. Hird. *Introduction to Liquid Crystals.* Taylor and Francis, London, 1997.

[29] S. Chandrasekhar. *Liquid Crystals.* Cambridge University Press, Cambridge, 1992.

[30] P. G. de Gennes and J. Prost. *The Physics of Liquid Crystals.* Oxford Science Publications, Oxford, 1993.

[31] B. Jerome. Surface effects and anchoring in liquid crystals. *Rep. Prog. Phys.*, 54:391, 1991.

[32] R. Eppenga and D. Frenkel. Monte carlo study of the isotropic and nematic phases of infinitely thin hard platelets. *Mol. Phys.*, 52:1303, 1984.

[33] L. D. Landau. Zur theorie der phasenumwandlungen ii. *Phys. Z. Sowjetunion*, 11:26, 1937.

[34] J. Nehring and A. Saupe. On the schlieren texture in nematic and smectic liquid crystals. *J. Chem. Soc., Faraday Trans. 2*, 68:1, 1972.

[35] P. M. Chaikin and T. C. Lubensky. *Principles of condensed matter physics*. Cambridge University Press, 1995.

[36] H. Zöcher. The effect of a magnetic field on the nematic state. *Trans. Faraday Soc.*, 29:945, 1933.

[37] P. Oswald and P. Pieranski. *Liquid crystals: concepts and physical properties illustrated by experiments*. Taylor & Francis, Boca Raton, 2005.

[38] Orsay liquid crystal group. Dynamics of fluctuations in nematic liquid crystals. *J. Chem. Phys.*, 51:816, 1969.

[39] D. Forster. Hydrodynamics and correlation functions in ordered systems: nematic liquid crystals. *Ann. Phys.*, 85:505, 1974.

[40] M. P. Allen and D. Frenkel. Calculation of liquid-crystal frank constants by computer simulation. *Phys. Rev. A*, 37:1813, 1988.

[41] M. P. Allen and D. Frenkel. Erratum: Calculation of liquid-crystal frank constants by computer simulation [phys. rev. a 37, 1813 (1988)]. *Phys. Rev. A*, 42:3641, 1990.

[42] M. P. Allen, M. A. Warren, M. R. Wilson, A. Sauron, and W. Smith. Molecular dynamics calculation of elastic constants in gay-berne nematic liquid crystals. *J. Chem. Phys.*, 105:2850, 1996.

[43] P. Poulin and D. A. Weitz. Inverted and multiple nematic emulsions. *Phys. Rev. E*, 57:626, 1998.

[44] M. Škarabot, M. Ravnik, S. Žumer, U. Tkalec, I. Proberaj, D. Babic, N. Osterman, and I. Muševič. Interactions of quadrupolar nematic colloids. *Phys. Rev. E*, 77:031705, 2008.

[45] P. Poulin, H. Stark, T. C. Lubensky, and D. A. Weitz. Novel colloidal interactions in anisotropic fluids. *Science*, 275:1770, 1997.

[46] V. G. Nazarenko, A. B. Nych, and B. I. Lev. Crystal structure in nematic emulsion. *Phys. Rev. Lett.*, 87:075504, 2001.

[47] P. S. Drzaic. Polymer dispersed nematic liquid crystal for large area displays and light valves. *J. Appl. Phys.*, 60:2142, 1986.

[48] M. Humar, M. Ravnik, S. Pajk, and I. Muševič. Electrically tunable liquid crystal optical microresonators. *Nat. Photonics*, 3:595, 2009.

[49] I. Muševič. Nematic colloids, topology and photonics. *Philos. Trans. R. Soc., A*, 371:20120226, 2013.

[50] R. Seemann, M. Brinkmann, T. Pfohl, and S. Herminghaus. Droplet based microfluidics. *Rep. Prog. Phys.*, 75:016601, 2012.

[51] G. M. Whitesides. The origins and the future of microfluidics. *Nature*, 442:368, 2006.

[52] A. Sengupta, S. Herminghaus, and C. Bahr. Liquid crystal microfluidics: surface, elastic and viscous interactions at microscales. *Liq. Cryst. Rev.*, 2:73, 2014.

[53] Y. K. Kim, B. Senyuk, and O. D. Lavrentovich. Molecular reorientation of a nematic liquid crystal by thermal expansion. *Nat. Commun.*, 3:1133, 2012.

[54] A. Sengupta, U. Tkalec, M. Ravnik, J. M. Yeomans, C. Bahr, and S. Herminghaus. Liquid crystal microfluidics for tunable flow shaping. *Phys. Rev. Lett.*, 110:048303, 2013.

[55] S. A. Jewell, S. L. Cornford, F. Yang, P. S. Cann, and J. R. Sambles. Flow-driven transition and associated velocity profiles in a nematic liquid-crystal cell. *Phys. Rev. E*, 80:041706, 2009.

[56] Y. J. Na, T. Y. Yoon, S. Park, B. Lee, and S. D. Lee. Electrically programmable nematofluidics with a high level of selectivity in a hierarchically branched architecture. *ChemPhysChem*, 11:101, 2010.

[57] J. G. Cuennet, A. E. Vasdekis, L. D. Sio, and D. Psaltis. Optofluidic modulator based on peristaltic nematogen microflows. *Nat. Photonics*, 5:234, 2011.

[58] J. L. Billeter and R. A. Pelcovits. Defect configurations and dynamical behavior in a gay-berne nematic emulsion. *Phys. Rev. E*, 62:711, 2000.

[59] H. Stark and D. Ventzki. Non-linear stokes drag of spherical particles in a nematic solvent. *Europhys. Lett.*, 57:60, 2002.

[60] J. Fukuda, H. Stark, M. Yoneya, and H. Yokoyama. Dynamics of a nematic liquid crystal around a spherical particle. *J. Phys: Condens. Matter*, 16:S1957, 2004.

[61] M. Yoneya, J. Fukuda, H. Yokoyama, and H. Stark. Effect of a hydrodynamic flow on the orientation profiles of a nematic liquid crystal around a spherical particle. *Mol Cryst. Liq. Cryst.*, 435:75/[735], 2005.

[62] T. Araki and H. Tanaka. Surface-sensitive particle selection by driving particles in a nematic solvent. *J. Phys.: Condens. Matter*, 18:L193, 2006.

[63] C. Zhou, P. Yue, and J. J. Feng. The rise of newtonian drops in a nematic liquid crystal. *J. Fluid Mech.*, 593:385, 2007.

[64] B. T. Gettelfinger, J. A. Moreno-Razo, Jr. G. M. Koenig, J. P. Hernández-Ortiz, N. L. Abbott, and J. J. de Pablo. Flow induced deformation of defects around nanoparticles and nanodroplets suspended in liquid crystals. *Soft Matter*, 6:896, 2010.

[65] J. J. Erpenbeck. Shear viscosity of the hard-sphere fluid via nonequilibrium molecular dynamics. *Phys. Rev. Lett.*, 52:1333, 1984.

[66] S. D. Stoyanov and R. D. Groot. From molecular dynamics to hydrodynamics: A novel galilean invariant thermostat. *J. Chem. Phys.*, 122:114112, 2005.

[67] M. Conradi, M. Ravnik, M.Bele, M.Zorko, S. Žumer, and I. Muševič. Janus nematic colloids. *Soft Matter*, 5:3905, 2009.

[68] M. Melle, S. Schlotthauer, M. G. Mazza, and M. Schoen. Defect topologies in a nematic liquid crystal near a patchy colloid. *J. Chem Phys.*, 136:194703, 2012.

[69] F. Caupin and E. Herbert. Cavitation in water: a review. *C. R Physique*, 7:1000, 2006.

[70] D. H. Trevena. Cavitation and the generation of tension in liquids. *J. Phys. D*, 17:2139, 1984.

[71] P. G. Debenedetti. Physics of water: Stretched to the limit. *Nature Physics*, 9:7, 2013.

[72] G. R. Luckhurst. On the creation of director disorder in nematic liquid crystals. *Thin Solid Films*, 509:36, 2006.

[73] E. A. Brujan and P. R. Williams. Cavitation phenomena in non-newtonian liquids. *Chem. Eng. Res. Des.*, 84:293, 2006.

[74] SV S. V. Stebnovskii. Experimental investigation of pulsed stretching of cavitating media. *J. Appl. Mech. Tech. Phys.*, 39:758, 1998.

[75] W. L. Lim, Y. T. Low, and W. L. Foo. Cavitation phenomena in mechanical heart valves: the role of squeeze flow velocity and contact area on cavitation initiation between two impinging rods. *J. Biomech.*, 36:1269, 2003.

[76] M. Versluis, B. Schmitz, A. von der Heydt, and D. Lohse. How snapping shrimp snap: through cavitating bubbles. *Science*, 289:2114, 2000.

[77] C. Mishra and Y. Peles. Cavitation in flow through a micro-orifice inside a silicon microchannel. *Phys. Fluids*, 17:013601, 2005.

[78] C. Mishra and Y. Peles. Flow visualization of cavitating flows through a rectangular slot micro-orifice ingrained in a microchannel. *Phys. Fluids*, 17:113602, 2005.

[79] C. Mishra and Y. Peles. An experimental investigation of hydrodynamic cavitation in micro-venturis. *Phys. Fluids*, 18:103603, 2006.

[80] M. Medrano, P. J. Zermatten, C. Pellone, J. P. Franc, and F. Ayela. Hydrodynamic cavitation in microsystems. i. experiments with deionized water and nanofluids. *Phys. Fluids*, 23:127103, 2011.

[81] E. Zwaan, S. L. Gac, K. Tsuji, and C.-D. Ohl. Controlled cavitation in microfluidic systems. *Phys. Rev Lett.*, 98:254501, 2007.

[82] A. Makke, M. Perez, J. Rottler, O. Lame, and J.-L. Barrat. Predictors of cavitation in glassy polymers under tensile strain: A coarse-grained molecular dynamics investigation. *Macromol. Theory Sim.*, 20:826, 2011.

[83] G. N. Toepperwein and J. J. de Pablo. Cavitation and crazing in rod-containing nanocomposites. *Macromolecules*, 44:5498, 2011.

[84] V. G. Baidakov, K. S. Bobrov, and A. S. Teterin. Cavitation and crystallization in a metastable lennard-jones liquid at negative pressures and low temperatures. *J. Chem. Phys.*, 135:054512, 2011.

[85] V. G. Baidakov and K. S. Bobrov. Spontaneous cavitation in a lennard-jones liquid at negative pressures. *J. Chem .Phys.*, 140:184506, 2014.

[86] C. J. Rasmussen, A. Vishnyakov, M. Thommes, B. M. Smarsly, F. Kleitz, and A. V. Neimark. Cavitation in metastable liquid nitrogen confined to nanoscale pores. *Langmuir*, 26:10147, 2010.

[87] C. J. Rasmussen, G. Y. Gor, and A. V. Neimark. Monte carlo simulation of cavitation in pores with nonwetting defects. *Langmuir*, 28:4702, 2012.

[88] R. Vorreuther, R. Corleis, T. Klotz, P. Bernards, and U. Engelmann. Investigative urology: Impact of shock wave pattern and cavitation bubble size on tissue damage during ureteroscopic electrohydraulic lithotripsy. *J. Urology*, 153:849, 1995.

[89] P. Zhong, H.-L. Tong, F. H. Cocks, M. S. Pearle, and G. M. Preminger. Transient cavitation and acoustic emission produced by different laser lithotripters. *J. Endourol.*, 12:371, 1998.

[90] V. Manjuladevi, R. Pratibha, and N. Y. Madhusudana. Phase transitions in liquid crystals under negative pressures. *Phys. REv Lett.*, 88:055701, 2002.

[91] J. L. Ericksen. Anisotropic fluids. *Arch. Rational Mech. Anal.*, 4:231, 1960.

[92] J. L. Ericksen. Theory of anisotropic fluids. *Trans. Soc. Rheol.*, 4:29, 1960.

[93] J. L. Ericksen. Conservation laws for liquid crystals. *Trans. Soc. Rheol.*, 5:23, 1961.

[94] J. L. Ericksen. Continuum theory of liquid crystals. *Appl. Mech. Rev.*, 20:1029, 1967.

[95] J. L. Ericksen. Continuum theory of liquid crystals of nematic type. *Mol. Cryst. Liq. Cryst.*, 7:153, 1969.

[96] F. M. Leslie. Some constitutive equations for anisotropic fluids. *Quart. J. Mech. Appl. Math.*, 19:357, 1966.

[97] F. M. Leslie. Some constitutive equations for liquid crystals. *Arch. Rational Mech. Anal.*, 28:265, 1968.

[98] O. Parodi. Stress tensor for a nematic liquid crystal. *J. Phys.*, 31:581, 1970.

[99] D. Seč. *Nematodynamics of a colloidal particle.* University of Lubljana, Ljubljana, 2009.

[100] M. Mięsowicz. The three coefficients of viscosity of anisotropic liquids. *Nature*, 158:27, 1946.

[101] B. D. Todd, D. J. Evans, and P. J. Daivis. Pressure tensor for inhomogeneous fluids. *Phys. Rev. E*, 52:1627, 1995.

[102] G. C. Stokes. On the effect of the internal friction of fluids on the motion of pendulums. *Cambridge Philos. Soc.*, 9:8, 1851.

[103] O. Reynolds. An experimental investigation of the circumstances which determine whether the motion of water shall be direct or sinuous, and of the law of resistance in parallel channels. *Philos. Trans. R. Soc. London*, 174:935, 1883.

[104] S. Tavoularis. *Measurment in fluid mechanics.* Cambridge University Press, Cambridge, 2005.

[105] P. G. de Gennes. *Nematodynamics*, page 373. Gordon and Breach, London, 1976.

[106] T. Graham. Liquid diffusion applied to analysis. *T. Philos. Trans. R. Soc.*, page 183, 1861.

[107] N. J. Wagner and J. F. Brady. Shear thickening in colloidal dispersions. *Phys. Today*, 62:27, 2009.

[108] M. D. Haw. Colloidal suspensions, brownian motion, molecular reality: a short history. *J. Phys.: Cond. Matt.*, 14:7769, 2002.

[109] C. W. W. Ostwald. *Die Welt der vernachlässigten Dimensionen: eine Einführung in die moderne Kolloidchemie mit besonderer Berücksichtigung ihrer Anwendungen.* Theodor Steinkopff, Dresden, 1914.

[110] E. A. Hauser. The history of colloid science: In memory of wolfgang ostwald. *J. Chem. Educ*, 32:2, 1955.

[111] A. V. Ryzhkova and I. Muševič. Particle size effects on nanocolloidal interactions in nematic liquid crystals. *Phys. Rev. E*, 87:032501, 2013.

[112] E. Yablonovitch. Inhibited spontaneous emission in solid-state physics and electronics. *Phys. Rev. Lett.*, 58:2059, 1987.

[113] M. Yada, J. Yamamoto, and H. Yokoyama. Spontaneous formation of regular defect array in water-in-cholesteric liquid crystal emulsions. *Langmuir*, 18:7436, 2002.

[114] D. Andrienko, G. Germano, and M. P. Allen. Computer simulation of topological defects around a colloidal particle or droplet dispersed in a nematic host. *Phys. Rev. E*, 63:041701, 2001.

[115] A. B. Pawar and I. Kretzschmar. Fabrication, assembly, and application of patchy particles. *Macromol. Rapid Commun.*, 31:150, 2010.

[116] C. Casagrande and M. Veyssié. Janus beads-realization and 1st observation of interfacial properties. *C. R. Acad. Sci. Paris, Ser II*, 306:1423, 1988.

[117] J. Yan, M. Bloom, S. C. Bae, E. Luijten, and S. Granick. Linking synchronization to self-assembly using magnetic janus colloids. *Nature*, 491:578, 2012.

[118] J. Hu, S. Zhou, Y. Sun, X. Fang, and L. Wu. Fabrication, properties and applications of janus particles. *Chem. Soc. Rev.*, 41:4356, 2012.

[119] M. P. Allen and D. J. Tildesley. *Comupter Simulations of Liquids.* Oxford University Press, Oxford, 1987.

[120] S. Hess and B. Su. Pressure and isotropic-nematic transition temperature of model liquid crystals. *Z. Naturforsch.*, 54a:559, 1999.

[121] H. Steuer, S. Hess, and M. Schoen. Pressure, alignment and phase behavior of a simple model liquid crystal. a monte carlo simulation study. *Physica A*, 328:322, 2003.

[122] H. Steuer, S. Hess, and M. Schoen. Phase behavior of liquid crystals confined by smooth walls. *Phys. Rev. E*, 69:031708, 2004.

[123] M. Greschek, M. Melle, and M. Schoen. Isotropic-nematic phase transitions in confined mesogenic fluids. the role of substrate anchoring. *Soft Matter*, 6:1898, 2010.

[124] M. Greschek and M. Schoen. Frustration of nanoconfined liquid crystals due to hybrid substrate anchoring. *Soft Matter*, 6:4931, 2010.

[125] M. Greschek and M. Schoen. Finite-size scaling analysis of isotropic-nematic phase transitions in an anisometric lennard-jones fluid. *Phys. Rev. E*, 83:011704, 2011.

[126] M. Greschek and M. Schoen. Orientational prewetting of planar solid substrates by a model liquid crystal. *J. Chem. Phys.*, 135:204702, 2011.

[127] J. G. Gay and B. J. Berne. Modification of the overlap potential to mimic a linear site-site potential. *J. Chem. Phys.*, 74:3316, 1981.

[128] S. Giura and M. Schoen. Density-functional theory and monte carlo simulations of the phase behavior of a simple model liquid crystal. *Phys. Rev. E*, 90:022507, 2014.

[129] P. I. C. Teixeira and M. M. Telo Da Gama. A model nematic liquid crystal revisited: some new phase diagrams from density-functional theory. *Mol. Phys.*, 86:1537, 1995.

[130] Y. Reznikov, O. Ostroverkhova, K. D Singer, J. H. Kim, S. Kumar, O. Lavrentovich, B. Wang, and J. L. West. Photoalignment of liquid crystals by liquid crystals. *Phys. Rev. Lett.*, 84:1930, 2000.

[131] J. Shan, W. shi, L. Y. Liu, Y. R. Shen, and L. Xu. Optical control of surface anchoring and reorientation of liquid crystals via a plasmon-enhanced local field. *Phys. Rev. Lett.*, 109:147801, 2012.

[132] A. A. Sonin. *The surface physics of liquid crystals*. Gordon and Breach, Amsterdam, 1995.

[133] H. F. Gleeson, T. A. Wood, and M. Dickinson. Laser manipulation in liquid crystals: an approach to microfluidics and micromachines. *Phil. Trans. R. Soc. A*, 364:2789, 2006.

[134] D. A. McQuarrie. *Statistical Mechanics*. University Science Books, Sausalito, 2000.

[135] L. Verlet. Computer "experiments" on classical fluids. i. thermodynamical properties of lennard-jones molecules. *Phys. Rev.*, 159:98, 1967.

[136] D. Frenkel and B. Smit. *Understanding molecular simulation: from algorithms to applications*. Academic Press, San Diego, 2002.

[137] J. M. Ilnytskyi and M. R. Wilson. A domain decomposition molecular dynamics program for the simulation of flexible molecules of spherically-symmetrical and non-spherical sites. ii. extension to nvt and npt ensembles. *Comput. Phys. Commun.*, 148:43, 2002.

[138] K. Singer, A. Taylor, and J. V. L. Singer. Thermodynamic and structural properties of liquids modelled by '2-lennard-jones centres' pair potentials. *Mol. Phys.*, 33:1757, 1977.

[139] J.-P. Ryckaert, G. Ciccotti, and H. J. C. Berendsen. Numerical integration of the cartesian equations of motion of a system with constraints: molecular dynamics of n-alkanes. *J. Comput. Phys.*, 23:327, 1977.

[140] S. Nosé. A unified formulation of the constant temperature molecular dynamics methods. *J. Chem. Phys.*, 81:511, 1984.

[141] S. Nosé. A molecular dynamics method for simulations in the canonical ensemble. *Mol. Phys*, 52:255, 1984.

[142] W. G. Hoover. Canonical dynamics: equilibrium phase-space distributions. *Phys. Rev. A*, 31:1695, 1985.

[143] R. D. Groot. A local galilean invariant thermostat. *J. Chem. Theory Comput.*, 2:568, 2006.

[144] J. Li and J. D. Lee. Reformulation of the nosé--hoover thermostat for heat conduction simulation at nanoscale. *Acta Mech.*, 225:1223, 2014.

[145] C. G. Gray and K. E. Gubbins. *Theory of Molecular Fluids.* Oxford University Press, Oxford, 1984.

[146] M. Ravnik, M. Škarabot, S. Žumer, U. Tkalec, I. Poberaj, D. Babič, N. Osterman, and I. Muševič. Entangled nematic colloidal dimers and wires. *Phys. Rev. Lett.*, 99:247801, 2007.

[147] E. M. Terentjev. Disclination loops, standing alone and around solid particles, in nematic liquid crystals. *Phys. Rev. E*, 51:1330, 1995.

[148] S. Grollau, E. B. Kim, O. Guzman, N. L. Abbott, and J. J. de Pablo. Monte carlo simulations and dynamic field theory for suspended particles in liquid crystalline systems. *J. Che. Phys.*, 119:2444, 2003.

[149] T. C. Lubensky, D. Pettey, N. Currier, and H. Stark. Topological defects and interactions in nematic emulsions. *Phys. Rev. E*, 57:610, 1998.

[150] W. J. Huisman, J. F. Peters, M. J. Zwanenburg, S. A.de Vries, T. .E Derry, D. Abernathy, and J. F. van der Veen. Layering of a liquid metal in contact with a hard wall. *Nature*, 390:379, 1997.

[151] L. Cheng, P. Fenter, K. L. Nagy, M. L. Schlegel, and N. C. Sturchio. Molecular-scale density oscillations in water adjacent to a mica surface. *Phys. Rev. Lett.*, 87:156103, 2001.

[152] J. Prost and P. G. de Gennes. Note on the dynamics of prenematic fluids. *Simple Views on Condensed Matter*, 4:78, 1992.

[153] R. W. Ruhwandl and E. M. Terentjev. Monte carlo simulation of topological defects in the nematic liquid crystal matrix around a spherical colloid particle. *Phys. Rev. E*, 56:5561, 1997.

[154] R. W. Zwanzig. High-temperature equation of state by a perturbation method. i. nonpolar gases. *J.Chem. Phys.*, 22:1420, 1954.

[155] A. Sengupta. *Topological Microfluidics*. Springer, Cham, 2013.

[156] A. Sengupta, B. Schulz, E. Ouskova, and C. Bahr. Functionalization of microfluidic devices for investigation of liquid crystal flows. *Microfluid. Nanofluid.*, 13:941, 2012.

[157] A. Sengupta, U. Tkalec, and C. Bahr. Nematic textures in microfluidic environment. *Soft Matter*, 7:6542, 2011.

[158] M. G. J. Gannon and T. E. Faber. The surface tension of nematic liquid crystals. *Philos. Mag. A*, 37:117, 1978.

[159] H. Kasten and G. Strobl. Nematic wetting at the free surface of 4-cyano-4'-n-alkylbiphenyls. *J. Chem. Phys.*, 103:6768, 1995.

[160] E. Smela and L. J. Martínez-Miranda. Effect of substrate preparation on smectic liquid crystal alignment: a structural study. *J. Appl. Phys.*, 73:3299, 1993.

# Acknowledgments

I would like to thank Prof. Dr. Martin Schoen for giving me the opportunity to write this thesis. It was a pleasure working under his guidance and I'm thankful for all the support he gave me throughout the years. I enjoyed the numerous open discussions and the freedom to work on whatever seemed interesting and worth to explore at the moment.

A special thank you goes to Dr. Marco. G. Mazza for the helpful and supportive discussions and phone calls we had. I'm grateful for his advise and help throughout the years. It was a lot of fun to collaborate with him on numerous projects.

I enjoyed working in the Schoen group and would like to thank everybody for the warm and easy-going atmosphere. Especially, I want to thank Sergej Püschel-Schlotthauer for all the support, fruitful discussions and all the good times we spend in general.

Thank you to my family for encouraging me to reach my goals and always believing in me. I would also like to thank Benjamin Zirnstein, Jana Gülzow, Raphael Peifer and Marek Diekmann for their honest friendship and all the fun moments in the last years.

Last and definitely never least I dedicate this work to my wife Ricarda. Without her I wouldn't have come even close to writing this. Thank you for always being there and knowing me so well.